DE-FG05-80ET-53088-655 IFSR #655

Collective Effects of Beam-Beam Interaction in a Synchrotron Collider

J.K. KOGA and T. TAJIMA
Institute for Fusion Studies
The University of Texas at Austin
Austin, Texas 78712

April 1994

Collective Effects of Beam-Beam Interaction in a Synchrotron Collider

J.K. KOGA[a] and T. TAJIMA
Department of Physics and
Institute for Fusion Studies
The University of Texas at Austin
Austin, Texas 78712

Abstract

The effects of the beam-beam interaction on particle dynamics in a synchrotron collider are investigated. The main highlight of this work is the investigation of collective effects of the beam-beam interaction in a self-consistent approach that naturally incorporates the correct single particle dynamics. The most important target of this simulation is to understand and predict the long-time ($10^8 - 10^9$ rotations) behavior of the beam luminosity and lifetime.

For this task a series of computer codes in one spatial dimension have been developed in increasing order of sophistication. They are: the single particle dynamics tracking code, the strong-strong particle-in-cell (PIC) code, and the particle code based on the δf algorithm. The later two include the single particle dynamics of the first. The third approach is used to understand beam lifetime by improving the numerical noise problem in the second.

Scans in tune ν_0 and tune shift $\Delta\nu_0$ show regions of stability and instability which correspond to the regions predicted by a linear theory. Strong resonance beam blowup

[a] present address: Advanced Science Research Center, Japan Atomic Energy Research Institute, Tokai, Ibaraki, Japan

is observed just above $\nu_0 = 1/2$ and $\nu_0 = 1/4$, where the rate of beam blowup drops with the order of the resonance.

In both the strong-strong code and δf code using the reference parameters of the SSC (Superconducting Super Collider), oscillations in the tune shift, $\Delta\nu$, are observed. The odd moments of the beam are increasing in oscillation amplitude with rotation number, while the amplitudes of the even moments either decrease or remain constant. The "flip-flop" effect is observed in the strong-strong code simulations and is found to be sensitive to the initial conditions.

In studying slow particle diffusion in the phase space of the beams away from resonances, the tracking code shows no diffusion of particles from the beam-beam interaction after 10^5 rotations. The strong-strong code is found too noisy to study particle diffusion from the beam-beam interaction. The much quieter δf code shows all particles diffusive after 10^5 rotations in contrast to single particle tracking results. The diffusion coefficients are several orders of magnitude higher than the tracking code and increase exponentially with the action. However, this amount of diffusion ($D \sim 10^{-10} - 10^{-11}$ in the normalized unit) is still permissible for the SSC design parameters. This diffusion is caused by the collision induced variation of the second moment of the beams $\langle x^2 \rangle$.

I Introduction

The key goal of high energy particle accelerators in addition to achieving high energies is achieving a high number of collision events from high energy colliding beams. In circular accelerators or synchrotrons this is accomplished by colliding two focussed beams which are travelling in opposite directions. The beams can be either of the same or opposite charge sign. The number of collision events depends on the interaction rate, R[13]:

$$R = L\sigma_{\text{int}} \ , \tag{1}$$

where L is the beam luminosity and σ_{int} is the interaction cross section of the particles in the beam. The luminosity of the colliding beams is defined as:

$$L = f\frac{N^2}{4\pi\sigma^2} \tag{2}$$

where N is the number of particles, σ is the rms beam size, and f is the frequency of collisions. To achieve a large interaction rate, it is necessary that the luminosity to be as high as possible. High luminosity is achieved by high collision frequencies, a large number of particles per beam, and small beam sizes. However, higher N increases collective effects, higher f results in multi-bunch instabilities, and lower σ places more demands on focusing systems and beam sources. Typically the luminosity L is a number between 10^{30} and $10^{33}\,\text{cm}^{-2}\,\text{sec}^{-1}$ for contemporary high energy accelerators. At high energies the interaction cross section σ_{int} tends to be small on the order of 10^{-32} to $10^{-33}\,\text{cm}^2$, as it is inversely proportional to the square of the beam energy. A large number of collisions is necessary to achieve a statistically significant amount of data. For example, in the Superconducting Super Collider (SSC) the projected storage time in the main ring is 24 hours. In this amount of time the bunched beams will undergo approximately 10^8 rotations and collisions. Therefore, the beams need to remain coherent for a long period of time. The major concern with circular colliders is

long term beam stability. Beam instabilities can lead to beam spreading which reduces beam luminosity and beam lifetimes. Beam instability is caused by many factors:

- longitudinal and transverse momentum spread of the beam
- noise in the system
- magnetic field gradient errors
- resonances
- steering errors
- focusing errors
- beam-beam interaction

One of the principle limitations on beam intensity is due to the beam-beam interaction via their collective electromagnetic fields.[4, 7] For hadron colliders the beam-beam interaction is expected to be even more crucial, since there is no synchrotron radiation damping to stop beam blow-up as in electron storage rings.[7]

In this paper we will concentrate on the beam-beam interaction with emphasis on the beam-beam kick and beam-beam plasma collective effects. In the beam-beam interaction each beam imparts an impulse on the other beam at the interaction point where the beams cross. This impulse may be treated as a kick, as the interaction time is much shorter than the beam particle dislocation time due to collisions. The kick can include both the impulse acting on whole beams and impulses acting on individual particles within each beam. Beam-beam plasma collective effects include plasma instabilities or "soft" collisions. These instabilities modify the beam profile and can contribute to increasing beam size. Collective instabilities have the most effect in the interaction region where the beam densities are highest in the accelerator. One of the fastest growing collective instabilities which can occur in a plasma

is the filamentation instability. However, in typical high energy heavy particle colliders the beam-beam interaction times are very short relative to the filamentation instability growth rate. In the SSC the interaction time is about 2% of the maximum growth rate time. The relative importance of collective effects in plasmas is determined from the plasma parameter g:

$$g = \frac{1}{n\lambda_D^3} \tag{3}$$

where n is the density and λ_D is the Debye length. If $g \ll 1$, collective effects play an important role. For SSC type parameters $g = 2.66$. So collective effects are not dominant for a single beam-beam interaction. However, the effects of a large number of successive interactions have yet to be determined.

The objective of this study is to determine beam-beam interaction effects on particle dynamics using a collective plasma model at the interaction point. A one dimensional model is employed at the interaction point so that oscillations in only one transverse direction due to the counterstreaming beams are studied. The rest of the machine is treated by simple harmonic transport (betatron oscillations). By employing a fully self-consistent model at the interaction point, an assessment of the relative importance of collisions as a whole and individual "soft" collisions (collective effects) can be determined. Specifically, we will examine the contribution of self consistent effects on beam blow up and particle diffusion after a large number of interactions.

II Simulation Models

In the course of our investigation various simulation models have been developed to study the beam-beam interaction. These models are presented in increasing order of sophistication and inclusion of physical effects.

Numerical simulation of accelerator beam dynamics has a relatively short history. As

accelerators became increasingly more costly and complex, computers and computational techniques also became increasingly more developed. Computer simulation has recently become an accepted standard method of investigation of accelerators. It certainly is this way for the Tevatron. For the SSC one may say even that it has become one of the central design techniques. An obvious reason for developing computer models is the cost. It is much cheaper to run a simulation than to build a device. Also simulations allow the study of the problem under very controlled conditions with accuracy limited by the precision of the computer. This is not the case with experimental setups. Analytical methods provide a means to study the problem in the linear regime. However, nonlinear aspects are not easily accessible. Numerical methods allow the study of this regime with fewer approximations than analytic methods. Simulation schemes such as the Particle-in-Cell (PIC) methods[3, 36] represent a medium ground between the 2 particle picture of the beam-beam interaction and the full statistical picture representing all particles in the beams.

In the following sections the various numerical codes used to study the beam-beam interaction will be described. They are the tracking code, Particle-in-Cell (PIC) codes, and the δf algorithm.

Tracking code

The basic principle of tracking codes is to follow the dynamics of single particles around the machine.[26] In the beam-beam interaction the tracking code consists of two components: a target beam and a projectile beam. The target beam is treated as a rigid smooth Gaussian distribution of a large number of particles. It remains unchanged from interaction to interaction. The projectile beam is considered to be a collection of mutually noninteracting particles which are perturbed by the target beam. This is the so called "weak-strong" approximation. In tracking code simulations in the "weak-strong" approximation, transport about one turn is simulated as the product of two matrices, one for the one turn Courant-Synder map,[8] and

the other for the impulsive application of the beam-beam interaction discussed above[26]:

$$\begin{bmatrix} x \\ x' \end{bmatrix}_{\text{final}} = M \begin{bmatrix} x \\ x' \end{bmatrix}_{\text{initial}} , M = \begin{bmatrix} \cos(2\pi\nu_0) & \beta_0^* \sin(2\pi\nu_0) \\ -\sin(2\pi\nu_0)/\beta_0^* & \cos(2\pi\nu_0) \end{bmatrix} \begin{bmatrix} 1 & 0 \\ 4\pi\Delta\nu_0 F(x)/\beta_0^* & 1 \end{bmatrix} , \quad (4)$$

where x is the position of the particle, x' is dx/ds, s is the distance along the collider, $\nu_0 = \oint ds/\beta(s)$ is the tune, $\Delta\nu_0$ is the input tune shift, β_0^* is the betatron oscillation amplitude at the interaction point (IP), and $F(x)$ is the 1-D truncation of the force from a round Gaussian beam

$$F(x) = \frac{1 - \exp(-x^2/2\sigma_{x_0}^2)}{x^2/2\sigma_{x_0}^2} , \quad (5)$$

where σ_{x_0} is the beam standard deviation in x. This formulation is similar to that of Neuffer *et al.*;[26] however, here both beams are of the same charge. For comparison with one dimensional simulation results, $F(x)$ becomes the force of a 1-D Gaussian slab:

$$F(x) = \sqrt{\frac{\pi}{2}} \left(\frac{\sigma_{x_0}}{x}\right) \text{erf}\left(\frac{x}{\sqrt{2}\sigma_{x_0}}\right) \quad (6)$$

where erf is the error function.

The first matrix in Eq. (4) takes into account the particle motion from the lattice magnets.[8] The second matrix takes into account the kick from the beam-beam interaction.

Particle-in-cell codes

In this section collider models using Particle-in-Cell (PIC) codes are described. In these models the collider is broken into two sections. One section models the interaction region. The other section models the rest of the storage ring. In the interaction region it is necessary to take into account the beam-beam interaction. Since self-consistent effects play an important role in the beam dynamics there, PIC codes are used. The rest of the collider is modelled using the Courant-Synder map which simply involves a symplectic rotation of the particles in phase space.[8]

A Particle-in-Cell (PIC) strong-strong code is used to model the beam-beam interaction region where the strong-strong code uses the "strong-strong" model where there is a

many particle-many particle interaction in the relativistic limit. Our model differs from previous models of the beam-beam interaction.[15, 17, 26, 33] Previous models approximated the beam-beam interaction as either a two particle interaction, a single particle-many particle interaction ("weak-strong" approximation),[15, 26] or a many particle-many particle interaction ("strong-strong") where the beam is constrained to be a Gaussian.[17, 33] Using a PIC code in the beam-beam model allows a many particle-many particle interaction with internal degrees of freedom in the beam shapes.

The steps of the simulation for one turn in the collider are:

1. interaction region
2. reset of fields to 0
3. symplectic mapping.

These steps are repeated until the necessary number of turns are attained. Figure 1 shows the basic geometry used in the simulation models.

Accelerator model

The model we use for the accelerator is shown in Fig. 1. Outside of the interaction region self-consistent effects are not as important as in the interaction region, since the density of the beams is much lower. Therefore, the approximation of single particle dynamics is a very good one. With this approximation a linear map can represent the collider in matrix notation:

$$\begin{pmatrix} x \\ x' \end{pmatrix}_{n+1} = \begin{pmatrix} 1 & -\Delta s \\ 0 & 1 \end{pmatrix} \begin{pmatrix} \cos(2\pi\nu_0) & \beta_0^* \sin(2\pi\nu_0) \\ -\frac{1}{\beta_0^*} \sin(2\pi\nu_0) & \cos(2\pi\nu_0) \end{pmatrix} \begin{pmatrix} x \\ x' \end{pmatrix}_n , \tag{7}$$

where Δs is the drift length along the collider path. The first matrix accounts for the finite length of the region as a free drift space and subtracting it from the full rotation. The

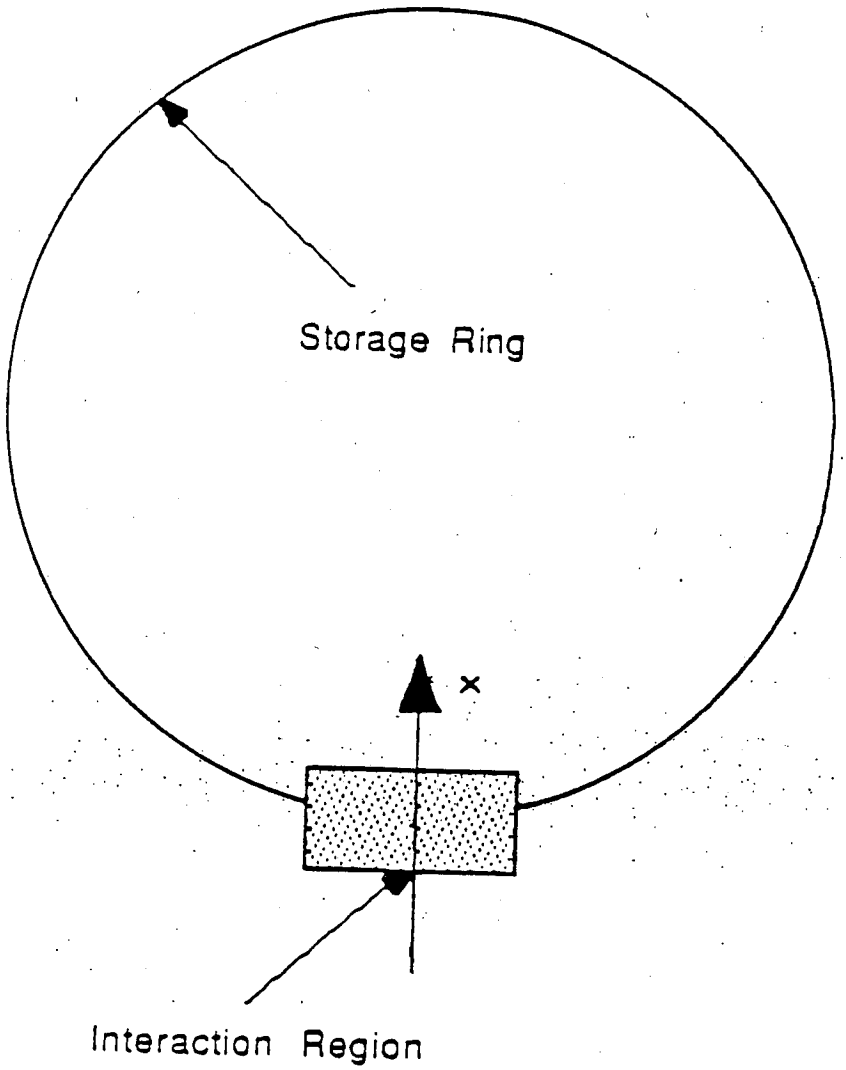

Figure 1: This shows the two components used to model the collider

second matrix is the Courant-Synder map around the collider where $\nu_0 = \oint ds/\beta(s)$ is the unperturbed tune and $\alpha = 0$ everywhere in the ring.[8]

Strong-strong code

A fully self-consistent electromagnetic treatment of the beam-beam interaction is severely constrained. Typically, fully electromagnetic codes solve the full set of Maxwell's equations. The main constraint on these types of codes is the time step size Δt which needs to be small enough to follow light waves for numerical stability[3, 36]:

$$c\Delta t < \Delta \ , \tag{8}$$

where c is the speed of light and Δ is the grid size of the simulation. Because of the small time step size the number of time steps to follow particles in the interaction region is prohibitively large for SSC parameters. For realistic SSC parameters 30000 time steps would be necessary for one interaction. To eliminate this, a strong-strong code is developed. The code has one spatial dimension x and three velocity coordinates (v_x, v_y, v_z). In this strong-strong code two approximations are made: (1) light waves are ignored and (2) self-fields (space charge effects) among particles of the same beam are ignored. Ignoring the effects of light waves can be justified for the SSC by considering the collisionless skin depth, λ_c, of the beam where:

$$\lambda_c = \frac{c}{\omega_b} \tag{9}$$

$$\omega_b = \sqrt{\frac{4\pi e^2 n_b}{\gamma m_b}} \ . \tag{10}$$

Using parameters for the SSC, $\lambda_c \gg w$ where w is the width of the beam. λ_c is the scale length over which a plasma responds to light waves. Since λ_c is much larger than the size of the beam, particles do not strongly interact with light waves. Self-fields of the beam are neglected, since the forces from the other beam are much larger. The ratio of the self fields

to the kick fields from the other beam goes as:

$$(\text{self-fields}) \approx \frac{1}{\gamma^2} (\text{kick fields}) \ , \tag{11}$$

where $\gamma = 2.13 \times 10^4$ for SSC parameters.

With the elimination of light waves the time step of the simulations can be on the order of the plasma frequency ω_p, which occurs on a much longer time scale than light waves. The time of interaction between the two beams is $\tau_{\text{int}} = \Delta s/2c$. τ_{int} is the time the simulation is run before the particles are rotated in phase space. With simulation time steps in units of fractions of ω_p the time period can now be represented by $1 - 4$ simulation time steps.

In particle simulations the beams are represented by a number of macroparticles. Each particle in the simulation has a particle shape factor $S(x)$. $S(x)$ is chosen to give the particles finite size, so that short wavelength oscillations are filtered out in the fields.[3, 36] This reduces noise and short range collision forces. The particular form chosen is:

$$S(x) = \frac{1}{\sqrt{2\pi}a} \exp\left(-\frac{x^2}{2a^2}\right) \ , \tag{12}$$

where a is the finite particle size.

Care must be taken when choosing the particle size a. When it becomes comparable to the beam width w, the tune shift $\Delta\nu$ is reduced. This can be expressed by:

$$\frac{\Delta\nu_{\text{point}}}{\Delta\nu_{\text{fsp}}} = \left(1 + 4\left(\frac{a}{w}\right)^2\right)^{1/2} \ , \tag{13}$$

where $\Delta\nu_{\text{point}}$ is the tune shift for a point particle, $\Delta\nu_{\text{fsp}}$ is the tune shift for a finite size particle, a is the particle size, and w is the beam width. This calculation is based on the assumption that the particle is Gaussian in shape as in Eq. (12). The particle size must be chosen so that $a \ll w$ and, therefore,

$$\frac{\Delta\nu_{\text{point}}}{\Delta\nu_{\text{fsp}}} \approx 1 \ . \tag{14}$$

The macroparticles are advanced by the Lorentz force equation:

$$\frac{d\mathbf{p}_i}{dt} = e\int_{-\infty}^{\infty} dx S(x - x_i)(\mathbf{E}(\mathbf{x}) + \mathbf{v}_i \times \mathbf{B}(\mathbf{x})/c) \ , \tag{15}$$

where $\mathbf{x}_i$ is the position, $\mathbf{p}_i$ is the momentum, $\mathbf{v}_i$ is the velocity of particle i, $S(x)$ is the particle shape factor, and $\mathbf{E}(\mathbf{x}_i)$ and $\mathbf{B}(\mathbf{x}_i)$ are the electric and magnetic field of the other beam, respectively. The integral over x takes into account the finite size of the particle.

The calculation of the fields can be simplified by performing the appropriate Lorentz transforms and taking into account the highly relativistic nature of the beams being studied. For a general Lorentz transformation to a frame moving at velocity $\vec{v}$ the transformation of the fields can be written[16]:

$$\mathbf{E} = \gamma(\mathbf{E}' + \boldsymbol{\beta} \times \mathbf{B}') - \frac{\gamma^2}{\gamma + 1}\boldsymbol{\beta}(\boldsymbol{\beta} \cdot \mathbf{E}') \ , \tag{16}$$

$$\mathbf{B} = \gamma(\mathbf{B}' - \boldsymbol{\beta} \times \mathbf{E}') - \frac{\gamma^2}{\gamma + 1}\boldsymbol{\beta}(\boldsymbol{\beta} \cdot \mathbf{B}') \ , \tag{17}$$

where $\boldsymbol{\beta} = \mathbf{v}/c$ and γ is the relativistic factor. Equations (16) and (17) can represent transformations of the fields from the frame moving with the beam $(\mathbf{E}', \mathbf{B}')$ to the lab frame $(\mathbf{E}, \mathbf{B})$. In the beam frame the beam particles only have thermal velocities. These velocities are small and randomly oriented. Therefore, only small remnant currents are present and the approximation $|\mathbf{B}'| \approx 0$ can be made. Equations (16) and (17) become:

$$\mathbf{E} = \gamma\mathbf{E}' - \frac{\gamma^2}{\gamma + 1}\boldsymbol{\beta}(\boldsymbol{\beta} \cdot \mathbf{E}') \ , \tag{18}$$

$$\mathbf{B} = -\gamma(\boldsymbol{\beta} \times \mathbf{E}') \ . \tag{19}$$

Assuming the motion of the beams is in the z direction the fields can be written:

$$E_x = \gamma E_x' \ , \tag{20}$$

$$B_y = \gamma\beta E_x' \ . \tag{21}$$

Since the beams are highly relativistic $\gamma \gg 1$, the approximation $|\beta| \approx 1$ can be made. Thus, $E_x \approx B_y$. Using this in Eq. (15), we obtain:

$$\frac{d\mathbf{p}_i}{dt} \approx e \int_{-\infty}^{\infty} dx S(x - x_i) E_x(x)(1 + v_i/c) \tag{22}$$

where v_i is the velocity of the beam kicked by the other beam. Again the approximation $v_i \approx c$ can be used:

$$\frac{d\mathbf{p}_i}{dt} \approx 2e \int_{-\infty}^{\infty} dx S(x - x_i) E_x(x) \tag{23}$$

Therefore, including the effects of the magnetic field kick to the beam simply involves doubling the contribution of the electrostatic field of the other beam.

The electric field E_x is calculated from:

$$\frac{\partial E_x}{\partial x} = 4\pi e \int S(x - x')\rho(x')dx' \ , \tag{24}$$

where $\rho(x)$ is the charge density and $S(x)$ is the particle shape factor. The charge density $\rho(x)$ is the accumulation of the finite size macroparticles:

$$\rho(x) = \sum_{j=1}^{N} q_j S(x - x_j) \ , \tag{25}$$

where N is the number of particles and q_j is the charge of particle j. Since the charge is accumulated on a grid, Fast Fourier Transforms (FFT) can be used to transform the grid to k space where manipulation is easier:

$$\rho(x) = \sum_{j=1}^{N} q_j \mathrm{e}^{-(x-x_j)^2/2a^2} \ , \tag{26}$$

$$\rho(k) = q\mathrm{e}^{-k^2a^2/2} \sum_{g} \mathrm{e}^{-ikx_g} \sum_{j \in g} \mathrm{e}^{-ik\delta_j} \ , \tag{27}$$

where a Gaussian shape factor is used $S(x - x_j) = \exp[-(x - x_j)^2/2a^2]$, the sum on g is over the grid points, a is the particle size, and δ_j is the distance of the particle from the nearest grid point $x_j - x_g$. The summation term with $j \in g$ is a sum over all particles j in grid cell g.

In order to increase the accuracy, the accumulation is done using cubic spline interpolation.[27, 36] This assignment technique allows a smoother grid assignment than lower order methods such as the subtracted dipole scheme (SUDS) or area weighting scheme.[3, 36] The charge density then takes the form[36]:

$$\rho(k) = q\mathrm{e}^{-k^2a^2/2}\left[\sum_g \mathrm{e}^{-ikx_g}\left(\sum_{j\in g} s_1 + \sum_{j\in g-1} s_2\right)\right.$$

$$\left. - ik\sum_g \mathrm{e}^{-ikx_g}\left(\sum_{j\in g} s_3 + \sum_{j\in g-1} s_4\right)\right] , \tag{28}$$

where the summation terms with $j \in g-1$ are sums over all particles j in grid cell $g-1$ and the s terms are the weighting factors:

$$s_1 = (1-\delta_j)^2(1+2\delta_j) \tag{29}$$

$$s_2 = \delta_j^2(3-2\delta_j) \tag{30}$$

$$s_3 = \delta_j(1-\delta_j)^2\Delta \tag{31}$$

$$s_4 = -(1-\delta_j)\delta_j^2\Delta \ . \tag{32}$$

The electric field in Eq. (24) can be transformed to k space using the FFT:

$$-ikE_x = 4\pi e\rho(k) \ , \tag{33}$$

where $\rho(k)$ is from Eq. (28). Using Eq. (28) and rearranging terms[36]:

$$E_x(k) = \frac{iq\mathrm{e}^{-k^2a^2/2}}{k}[\mathrm{FFT(G1X)} - ik\mathrm{FFT(G2X)}] \ , \tag{34}$$

where FFT is the Fast Fourier Transform and

$$\mathrm{G1X} = \sum_{j\in g} s_1 + \sum_{j\in g-1} s_2 \tag{35}$$

$$\mathrm{G2X} = \sum_{j\in g} s_3 + \sum_{j\in g-1} s_4 \ , \tag{36}$$

where G2X corresponds to derivatives of the charge density. Note that two quantities, G1X and G2X, need to be accumulated in this method. The force on the particles $F(x)$ can be calculated in a similar manner[36]:

$$F(x) = qE(x) \tag{37}$$

$$= s_1(\delta)F_s(x_g) + s_2(\delta)F_s(x_g + \Delta)$$

$$+ s_3(\delta)F_d(x_g) + s_4(\delta)F_d(x_g + \Delta) \ , \tag{38}$$

where δ is the distance from the nearest grid point $x - x_g$ and

$$F_s = \frac{q}{2\pi L} \mathrm{FFT}^{-1}[\mathrm{e}^{-k^2a^2/2}E(k)] \ , \tag{39}$$

$$F_d = \frac{q}{2\pi L} \mathrm{FFT}^{-1}[ik\mathrm{e}^{-k^2a^2/2}E(k)] \ , \tag{40}$$

where L is the system length, and FFT^{-1} is the inverse transform.

The previous field calculation solves the field for periodic boundary conditions. Note that the field equation does not take into account finite charge in the system. Finite charge is included in the $k = 0$ term. However, this term cannot be incorporated, since one gets a division by zero. To account for finite charge in the system, the $k = 0$ term in E_x can be explicitly calculated[9]:

$$E_x^{k=0}(x) = -4\pi\rho(0)\left(\frac{L_x}{2} - x\right) \ , \tag{41}$$

where L_x is the length of the system and $\rho(0)$ is the $k = 0$ component of the charge density which calculates the total charge in the system. By adding this field to the field calculated from Eq. (34) one gets the field with vacuum boundary conditions.

In the SSC design each beam has $\sim 10^{10}$ particles and a large number of beam-beam interactions (10^8). Due to computer time limitations the beams may only be represented by $\sim 10^3 - 10^4$ particles. We find that the representation of Eq. (24) and (15) by the well known PIC method[3, 36] with macroparticles shows a large amount of noise due to the small

number of computational macroparticles. This is especially apparent when single particle diffusion is studied. To study particle diffusion we, therefore, implemented a few improved algorithms for noise reduction. One is the cubic spline for smoother interpolation,[36] which was described above. Another is to load the macroparticles using a quiet start.[3] The third is to follow the portion of the particles due to the perturbed distribution only.[10, 22, 36] This is described in the next section.

Normally simulation macroparticles are distributed initially in a Gaussian profile via random number generators. A distribution produced from this method is shown in Fig. 2. The distribution integrated over p_x is shown in Fig. 3. Although the distribution resembles a Gaussian, it contains spikes and peaks which produce start-up noise.

This start-up noise can be minimized by using the technique of the quiet start to load the macroparticles.[3] Two methods of loading simulation macroparticles are described. One method distributes the particles uniformly in phase space and assigns charge nonuniformly to the particles based on the initial particle distribution. The other method involves nonuniform distribution of the particles in phase space and uniform charge for each particle.

In the first method the particles are distributed uniformly in r and θ where r and θ are defined in terms of x and p_x as:

$$r^2 = \frac{x}{\beta_0^*}^2 + \frac{p_x}{p}^2 \tag{42}$$

$$\tan(\theta) = \frac{x}{\beta_0^*}\frac{p}{p_x}, \tag{43}$$

where β_0^* is the betatron oscillation length at the interaction point and p the particle momentum along the collider. The increments in r and θ are determined from values input into the code. The r increment Δr is $r_{\max}/n_r$, where $r_{\max}$ is the maximum value of r and n_r is the number of r segments. The angle increment $\Delta\theta$ is $2\pi/n_\theta$, where n_θ is the number of angle segments. The initial distribution for 10000 particles is shown in Fig. 4. Assuming a

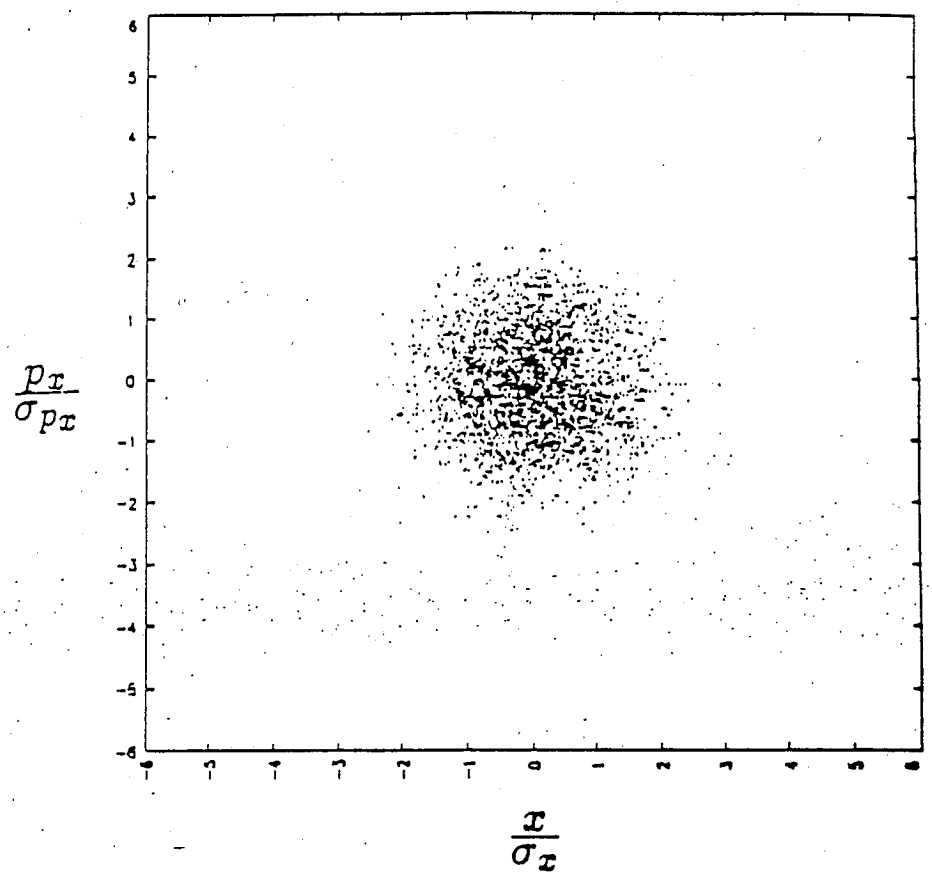

Figure 2: A Gaussian distribution of particles produced from a random number generator

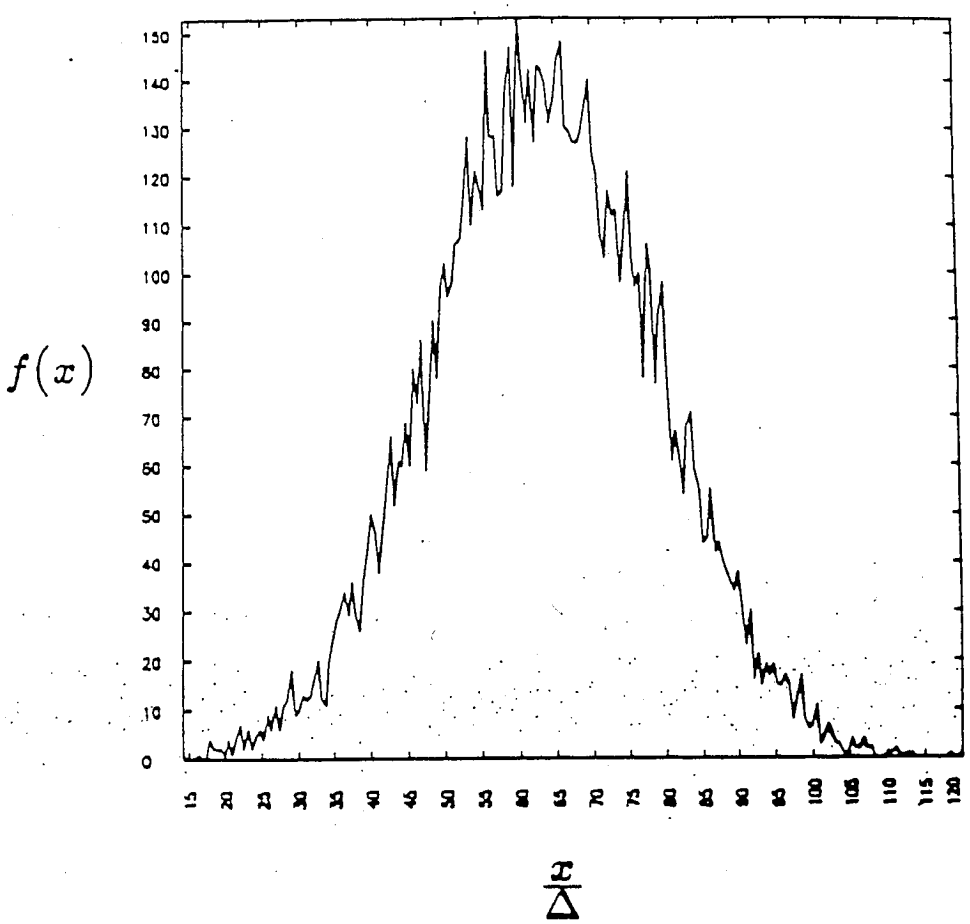

Figure 3: Distribution integrated over p_x with random number generated phase space positions

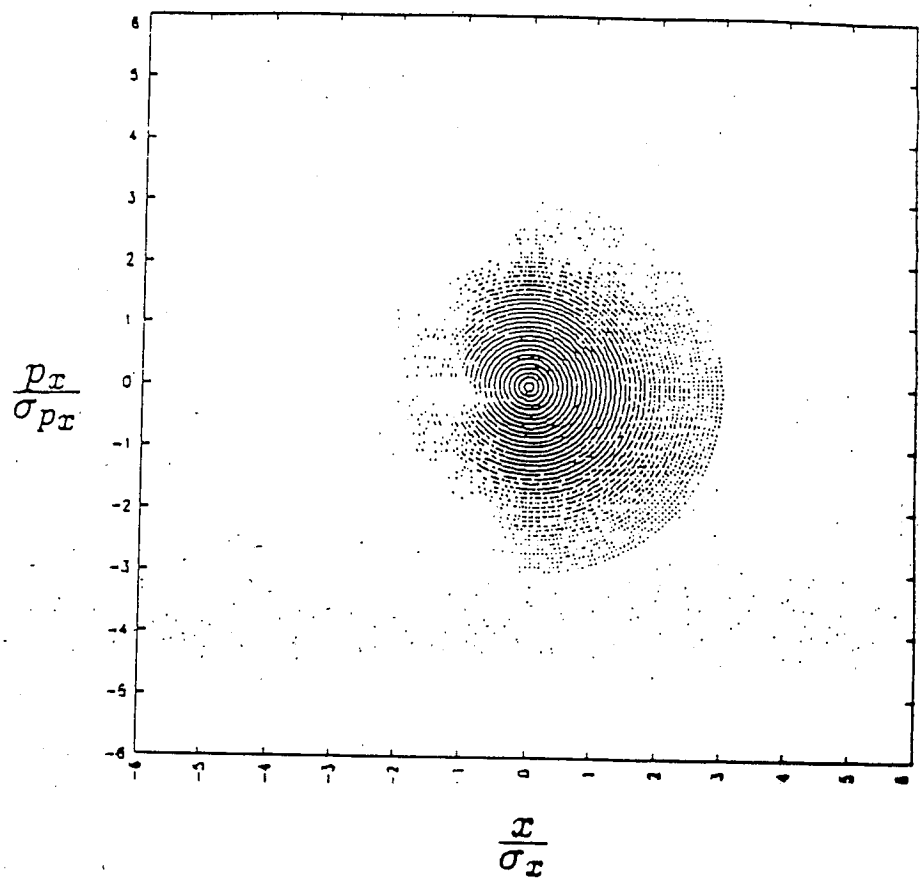

Figure 4: Uniform distribution of 10000 particles in x, p_x phase space

Gaussian profile for the beam in $x - p_x$ of the form:

$$f(x, p_x) = \frac{N}{2\pi\sigma_x\sigma_{p_x}} \exp\left(-\frac{x^2}{2\sigma_x^2} - \frac{p_x^2}{2\sigma_{p_x}^2}\right) . \tag{44}$$

Each particle can be assigned charge q_i where:

$$q_i = Ne \frac{r_i \exp\left(-\frac{r_i^2}{2\sigma^2}\right)}{\sum_{i=1}^{N} r_i \exp\left(-\frac{r_i^2}{2\sigma^2}\right)} , \tag{45}$$

N is the number of simulation particles, e is the unit charge, r_i is obtained from Eq. (42) for particle i, and σ is σ_x. Although each particle is assigned a different charge q_i, each particle is also assigned a different mass m_i so that the force on each particle is the same.

The distribution integrated over p_x is shown in Fig. 5 after the charge assignment. In comparison with the random distribution [Fig. 3] this distribution is much smoother in the tails and is more symmetric about the center. This symmetry reduces the higher order moments in the distribution and therefore produces less start-up noise.

In the second quiet start method particles are distributed nonuniformly in r and θ, where r and θ are defined in terms of x and p_x in Eqs. (42) and (43).[14] The number of particles at each r value is determined by a cumulative integration method.[3, 36] Again a Gaussian distribution $f(x, p_x)$ in x and p_x is assumed [Eq. (44)]. This function can be integrated in r and θ coordinates to yield:

$$N(r) = N\left(1 - \exp\left(-\frac{r^2}{2\sigma_r^2}\right)\right) , \tag{46}$$

where $N(r)$ is the number of particles contained within radius r and N is the total number of simulation particles. Equation (46) can be used to obtain the number of particles to add between r and $r + \Delta r$:

$$\Delta N = N\left[\exp\left(\frac{r^2}{2\sigma_r^2}\right) - \exp\left(\frac{(r + \Delta r)^2}{2\sigma_r^2}\right)\right] , \tag{47}$$

where ΔN is the number of particles to be added. The ΔN particles between r and $r + \Delta r$ are distributed uniformly in θ with a random offset θ_{ran} at $r + \Delta r/2$. The initial distribution

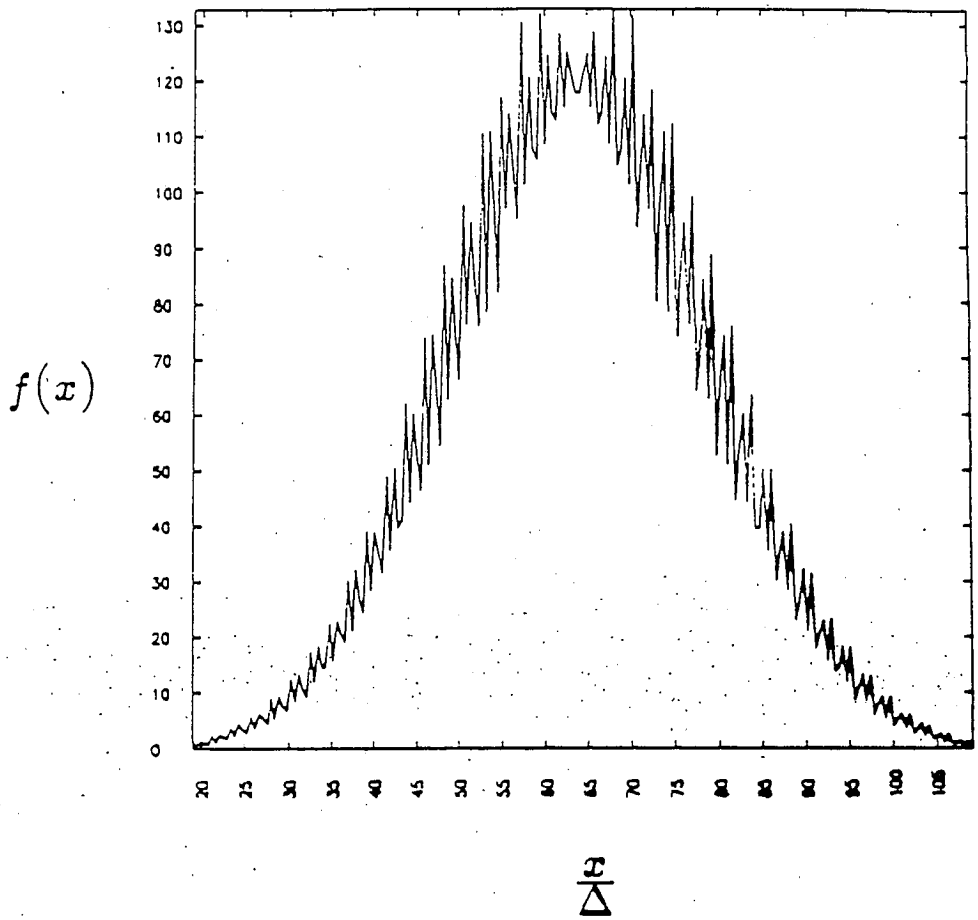

Figure 5: Distribution integrated over p_x with uniform distribution and nonuniform charge assignment

for 10000 particles is shown in Fig. 6. The distribution integrated over p_x is shown in Fig. 7. This distribution is smoother than both the random distribution of particles [Fig. 3] and the uniform distribution of differently charged particles [Fig. 5].

Noisy model

In order to study particle diffusion brought about by the beam-beam interaction, sources of numerical noise in the PIC codes need to be quantified. One source of noise is the fluctuations due to the use of a finite number of particles. To model this noise in PIC simulations, noise is added to the tracking code described in Sec. 2. This is done by adding a fluctuation term to the tune shift $\Delta\nu_0$:

$$\Delta\nu = \Delta\nu_0(1 + R\, n(x)) \;, \tag{48}$$

$$n(x) = \frac{1}{\sqrt{N(x)}} \;, \tag{49}$$

where $N(x)$ is the number of particles contained between $-x$ and $+x$ and R is a random number between -1 and 1. $n(x)$ gives an idea of the fluctuation level where

$$N(x) = N \,\mathrm{erf}\left(\frac{x}{\sqrt{2}\,\sigma_x}\right) \;, \tag{50}$$

N is the total number of particles. Equation (50) is calculated for a Gaussian distribution of particles.

δf algorithm

PIC codes typically use macroparticles to represent the the entire distribution of particles. In the beam-beam interaction for the SSC, the beams consist of 10^{10} particles each. Simulating this many particles with the PIC technique is computationally prohibitive. With the conventional PIC code 10^{10} particles are represented by only $10^3 - 10^4$ simulation particles

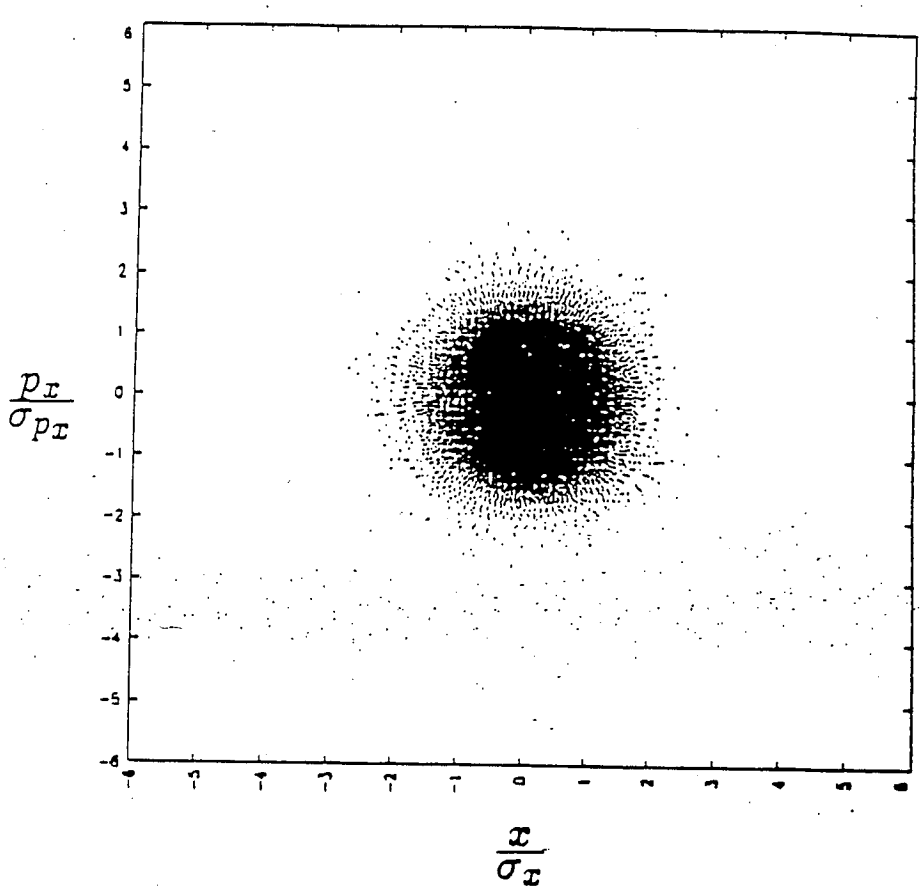

Figure 6: A nonuniform distribution of 10000 particles with equal charge

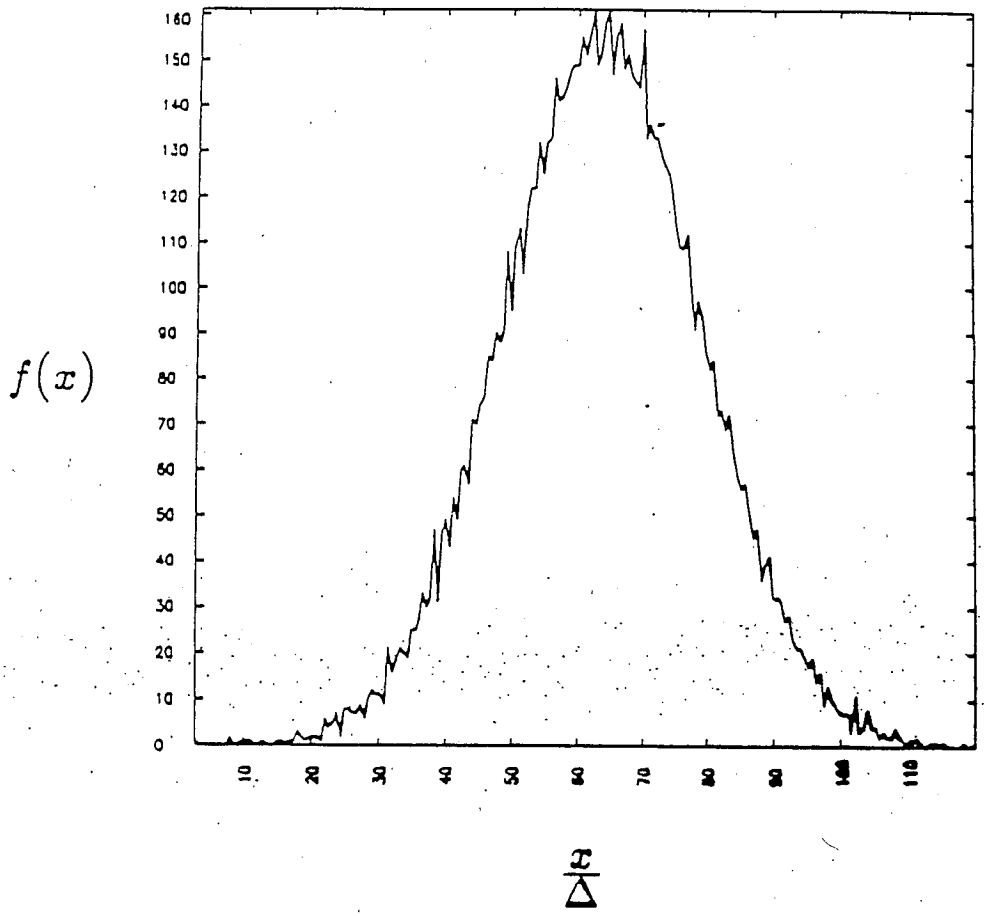

Figure 7: The profile in x of a nonuniform distribution of particles

allowing simulation of the beam-beam interaction in a reasonable computation time. However, the fluctuation level of various quantities such as the beam density ρ in the code is much higher than that of the real beam. The fluctuation level $\delta\rho$ goes as approximately:

$$\frac{\delta\rho}{\rho} \approx \frac{\sqrt{N}}{N} , \tag{51}$$

where N is the number of particles. Therefore, the fluctuation level of the PIC code is about 10^3 times higher than that of the real beam. Although this probably is not significant for beam blowup near resonances, the higher fluctuation level has a large effect on more subtle phenomenon such as particle diffusion. To facilitate the study of subtle effects, a δf code has been developed.[10, 22, 35, 36]

The δf method follows only the fluctuating part of the distribution instead of the entire distribution. This is essentially modelling the numerator on the right hand side of Eq. (51) which goes as $\sqrt{N}$. So the $10^3 - 10^4$ computational particles are used to represent $\sqrt{10^{10}}$ or 10^5 real fluctuation particles. This is only one or two orders of magnitude beyond the number of computer particles.

In the previous sections the strong-strong code used a finite number of particles to represent the Vlasov equation or Klimontovich equation.[20] In the particular case of the beam-beam interaction:

$$\frac{\partial f}{\partial s} + x' \frac{\partial f}{\partial x} - (K(s)x - F(x,s)) \frac{\partial f}{\partial x'} = 0 , \tag{52}$$

where $K(s)x$ is the usual magnetic guiding force and $F(x,s)$ is the beam-beam force

$$F(x,s) = \frac{2eE_x(x)}{\gamma m v^2} \delta_p(s) , \tag{53}$$

where $E_x(x)$ is calculated from the distribution of the particles and $\delta_p(s)$ the periodic δ-function. $\delta_p(s) = 1$ when $s = nL$ where L is the accelerator circumference and $n = 0, 1, ...$ The distribution function f is represented by a finite number of particles by:

$$f(x,x',s) = \sum_{i=1}^{N} \delta(x - x_i(s))\delta(x' - x_i'(s)) , \tag{54}$$

where N is the number of simulation particles used.

In the δf method only the perturbative part of the distribution is followed.[10, 22, 36] The total distribution function $f(x, x', s)$ is decomposed into

$$f(x, x', s) = f_0(x, x', s) + \delta f(x, x', s) \ , \tag{55}$$

where $f_0(x, x', s)$ is the steady or slowly varying part of the distribution and $\delta f(x, x', s)$ is the perturbative part. The key to this method is finding a distribution $f_0(x, x', s)$ which is close to the total distribution $f(x, x', s)$. The perturbative part $\delta f(x, x', s)$ is then small, causes only small changes to the distribution, and thus represents only the fluctuation levels. If a distribution $f_0(x, x', s)$ close to the total distribution is not found, then $\delta f(x, x', s)$ represents more than the fluctuating part of the total distribution. This defeats the purpose of the method. The ideal situation is for $f_0(x, x', s)$ to have an analytic solution. In this case any numerical truncation errors which result from the necessary derivatives of this function are eliminated. If an analytic solution cannot be found, then a numerical solution needs to be found which is close to the total distribution $f(x, x', s)$ and is slowly varying. Continual numerical update of $f_0(x, x', s)$ would also defeat the purpose of the δf method, since the PIC technique essentially does this also.

In the particular case of the beam-beam interaction an analytic solution to an equation close to the original Vlasov equation can be found. In the case of a linearized beam-beam force the Vlasov equation can be written in the form:

$$\frac{\partial f_0}{\partial s} + x' \frac{\partial f_0}{\partial x} - (K(s) - F_0(s)) x \frac{\partial f_0}{\partial x'} = 0 \ , \tag{56}$$

where

$$F_0(s) = F_0 \delta_p(s) \ . \tag{57}$$

F_0 is the linear portion of the beam-beam force $F(x)$. The solution is a Gaussian of the

form:

$$f_0(r) = \frac{N\beta^*}{2\pi\sigma^2} \exp\left(-\frac{r^2}{2\sigma^2}\right) , \tag{58}$$

where $r^2 = x^2 + \beta^{*2}x'^2$, N is the total number of particles in the beam, β^* is the betatron oscillation length, and σ is in the x direction. Note that if the beam-beam force were linear this solution $f_0(r)$ would represent the distribution for all time in the interaction region as well as in the rest of the storage ring. Only the values of β^* and σ differ between the two regions. In the interaction region the β^* and σ are calculated using the dynamic β model which assumes a linear beam-beam force[1, 30]:

$$\cos(2\pi\nu) = \cos(2\pi\nu_0) + 2\pi\Delta\nu \sin(2\pi\nu_0) , \tag{59}$$

$$\frac{\beta^*}{\beta_0^*} = \frac{\sin(2\pi\nu_0)}{\sin(2\pi\nu)} , \tag{60}$$

where ν_0 and β_0^* are the unperturbed quantities valid in the rest of the storage ring and ν and β^* are the quantities perturbed by the linearized beam-beam force. From the perturbed β^* the perturbed beam width σ can be calculated from the formula:

$$\frac{\beta_0^*}{\beta^*} = \frac{\sigma_0^2}{\sigma^2} , \tag{61}$$

where σ_0 is the unperturbed beam width which is obtained from the assumption that the beam emittance is unchanged due to this linear beam-beam force. An equation for the perturbed β^* can be written in terms of unperturbed quantities from Eqs. (59) and (60):

$$\left(\frac{\beta^*}{\beta_0^*}\right)^2 - 4\pi\Delta\nu_0 \cot(2\pi\nu_0) \left(\frac{\beta^*}{\beta_0^*}\right)^{3/2} - (2\pi\Delta\nu_0)^2 \left(\frac{\beta^*}{\beta_0^*}\right) - 1 = 0 , \tag{62}$$

where $\Delta\nu_0$ is the unperturbed one dimensional tune shift. Equation (62) can be expressed in terms of the perturbed σ using Eq. (61):

$$\left(\frac{\sigma}{\sigma_0}\right)^4 - 4\pi\Delta\nu_0 \cot(2\pi\nu_0) \left(\frac{\sigma}{\sigma_0}\right)^3 - (2\pi\Delta\nu_0)^2 \left(\frac{\sigma}{\sigma_0}\right)^2 - 1 = 0 . \tag{63}$$

Both equations can be solved for the perturbed σ or β^* using a root finder. Once this is obtained the other perturbed quantities, ν and $\Delta\nu$, are obtained from Eqs. (59) and (60).

Subtracting the linearized equation in Eq. (56) from the total Vlasov equation in Eq. (52), we obtain the perturbative part of Eq. (52) for δf :

$$\frac{\partial \delta f}{\partial s} + x' \frac{\partial \delta f}{\partial x} - (K(s)x - F_0(x,s)) \frac{\partial \delta f}{\partial x'} = -(F(x,s) - F_0(s)x) \frac{\partial f_0}{\partial x'} . \tag{64}$$

$F_0(x,s)$ is the kick from a Gaussian beam and $F(x,s)$ is the kick from a Gaussian beam $F_0(x,s)$ plus the perturbation $\delta F(x,s)$. As a result of using the dynamic beta model for the stationary solution f_0, only the nonlinear part of the beam-beam force on the right hand side of Eq. (64) is used to advance δf. The terms $\frac{\partial f_0}{\partial x'}$ and $F_0(x,s)$ are calculated using the perturbed dynamic beta quantities β^* and σ. Note that the unperturbed Gaussian field $F_0(x,s)$ is used on the lefthand side of Eq. (64) which makes the equation linear in δf. The term which has been neglected is

$$\delta F(x,s) \frac{\partial \delta f}{\partial x'} . \tag{65}$$

This term can be shown to be small in our problem. A possible incorporation of this term in the algorithm is described in Sec. 4. The reason for choosing the particular form of the steady state solution is apparent. It is chosen so that the right-hand side of Eq. (64) is small.

Finite particle representation

The perturbative part of the distribution δf [Eq. (64)] can be represented by a finite number of particles (characteristics):

$$\delta f(x,x',s) = \sum_{i=1}^{N} w_i[s, x_i(s), x_i'(s)] \delta(x - x_i(s)) \delta(x' - x_i'(s)) . \tag{66}$$

Substituting this into the equation for δf advance, we obtain:

$$\frac{dw_i}{ds} = -\frac{1}{n} \left[(F(x,s) - F_0(s)x) \frac{\partial f_0}{\partial x'} \right]_i , \tag{67}$$

where

$$n = \left(\frac{N_c}{\Delta x \Delta x'} \right) . \tag{68}$$

This density n is calculated on the assumption that the particles are distributed uniformly in phase space. The density n is assumed constant through the entire run. This approximation is no longer valid when there is either significant clumping of particles or the particles have spread out in phase space. Thus, the δf algorithm is most suited to problems that occur far away from resonances.

In the δf algorithm x_i, x_i', and w_i are advanced. The advance of the extra term w_i increases the number of operations over the PIC method and leads to other numerical constraints which will be described in the next section.

The simulation particles are distributed evenly in phase space upon initialization. The particles are distributed uniformly in x and p_x phase space in a cylindrical coordinate system r and θ. r and θ are defined in terms of x and p_x as:

$$r^2 = \frac{x}{\beta_0^*}^2 + \frac{p_x}{p}^2 , \tag{69}$$

$$\tan(\theta) = \frac{x}{\beta_0^*}\frac{p}{p_x} , \tag{70}$$

where β_0^* is the betatron oscillation length at the interaction point and p the particle momentum along the collider in s. The maximum r value is input into the code and is broken up into segments of length Δr. The number of particles at each r value is determined by a cumulative integration method.[36] The particular functional form is:

$$\Delta N = \frac{N}{N_r^2}(2r-1) , \tag{71}$$

where ΔN is the number of particles to be added, N is the number of particles, and N_r is the number of Δr segments to the edge of the distribution. Once the number of particles between r and $r+\Delta r$ is known they are distributed uniformly in θ with a random offset θ_{ran} at $r+\Delta r/2$. The initial distribution for 1000 particles is shown in Fig. 3. The purpose of this method is have each particle cover an equal area of phase space.

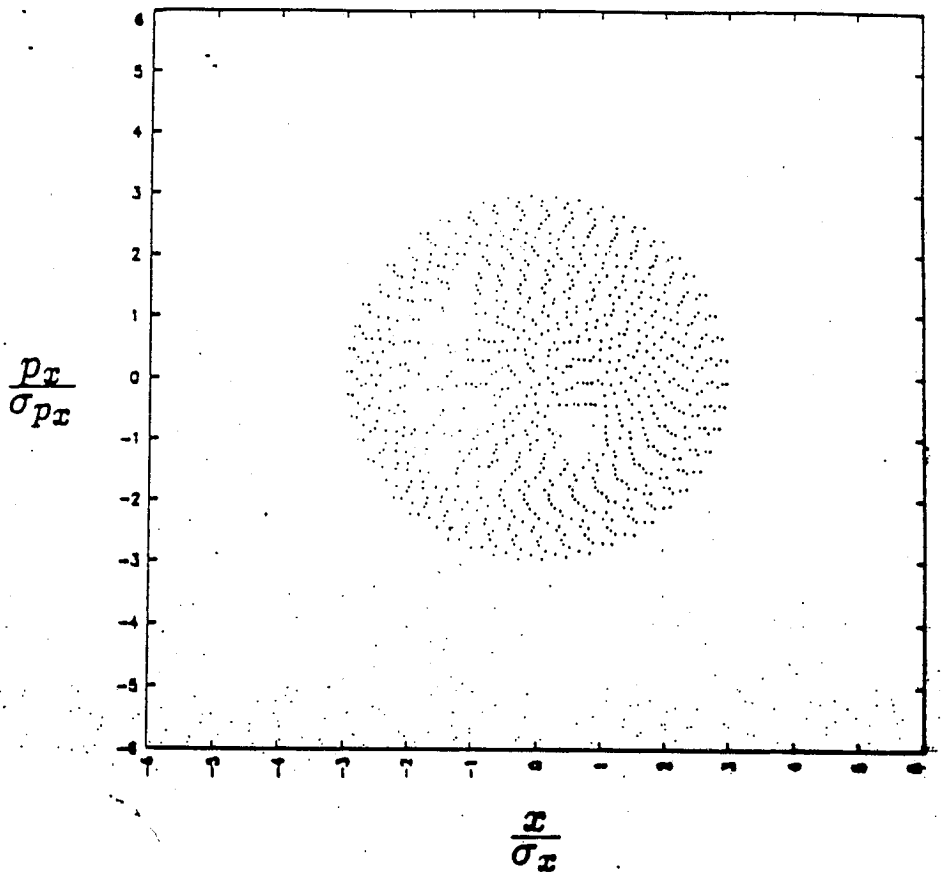

Figure 8: Uniform distribution of 1000 particles in x, p_x phase space

Symplectic mapping

Results from previous runs indicate that a higher order integration scheme for the characteristic advance is necessary for the δf algorithm. In runs where just the leapfrog scheme is used, the code is inaccurate in the particle push. This higher order integration scheme for the particles is needed in the δf algorithm because small changes to the initial distribution are being studied. In the PIC codes the numerical noise caused by the finite number of particles is larger than that produced by the numerical diffusion of the particles caused by the leapfrog integration scheme.

In this section we describe a symplectic finite difference scheme to counter the effects of numerical diffusion on the particle motion. In this scheme the normal symplectic mapping is used to advance the particles with an additional perturbation term.

Without the beam-beam force term a symplectic transformation map for the characteristics with the magnetic field can be written. Also in the case of a linearized beam-beam force a symplectic transformation map can be written with slight modifications. The map can be written in the form:

$$\begin{pmatrix} x \\ x' \end{pmatrix}_f = \begin{pmatrix} \cos(\theta) & \beta_0^* \sin(\theta) \\ -\frac{1}{\beta_0^*} \sin(\theta) & \cos(\theta) \end{pmatrix} \begin{pmatrix} x \\ x' \end{pmatrix}_i , \tag{72}$$

where $x = dx/ds$, s is the coordinate along the collider, $\theta = \int_0^s ds/\beta_0^*$, and the indices i and f refer to the initial and final positions, respectively. This map is used at all places in the storage ring including the interaction region. Upon adding the symplectic map the particle motion is accurate to many decimal places.

A simple implementation of the beam-beam force which preserves symplecticity involves approximating the force with an impulse. Using Hill's equation:

$$x'' + K(s)x = \frac{F(x)}{\gamma m v^2} \delta_p(s) , \tag{73}$$

where the term on the right-hand side of the equation is due to the beam-beam force. The

mapping is the same as a tracking code with the beam-beam force:

$$\begin{pmatrix} x \\ x' \end{pmatrix}_f = \begin{pmatrix} 1 & 0 \\ G(x) & 1 \end{pmatrix} \begin{pmatrix} x \\ x' \end{pmatrix}_i , \tag{74}$$

where

$$G(x) = \frac{F_0(x)}{\gamma m v^2} \frac{1}{x} , \tag{75}$$

and $F_0(x)$ is the unperturbed force due to a Gaussian beam.

In the particle advance scheme the particles are advanced first using the transfer matrix for a distance in $\theta = \Delta s/4\beta_0^*$ where $\Delta s = c\Delta t$. The particles are then kicked by the beam-beam field for $\Delta s/2\beta_0^*$ and then advanced again $\Delta s/4\beta_0^*$. The total matrix is:

$$\begin{pmatrix} x \\ x' \end{pmatrix}_f = M(\theta) \begin{pmatrix} 1 & 0 \\ G(x) & 1 \end{pmatrix} M(\theta) \begin{pmatrix} x \\ x' \end{pmatrix}_i , \tag{76}$$

$$M(\theta) = \begin{pmatrix} \cos(\theta) & \beta_0^* \sin(\theta) \\ -\frac{1}{\beta_0^*} \sin(\theta) & \cos(\theta) \end{pmatrix} , \tag{77}$$

where $\theta = \Delta s/(4\beta_0^*)$ and x used in $G(x)$ is the intermediate x value obtained from the first transfer matrix application.

$$G(x) = \frac{F_0(x)}{\gamma m v^2} \frac{1}{x} \frac{\Delta s}{2} . \tag{78}$$

Time advance

In this section the time advance scheme of the code is described. The entire predictor-corrector advance scheme is shown in Table 1.

The n in Table 1 refers to the time step number. In step 2 $\delta f^{n+1}_{\text{predict}}$ is calculated from the discretization of Eq. (67):

$$w^{n+1}_{i_{\text{predict}}} = w^{n-1}_i - \frac{1}{n} \left[(F^n(x^n_i, \delta f^n) - F_0 x^n_i) \frac{\partial f_0(x^n_i, x'^n_i)}{\partial x'} \right] 2\Delta s , \tag{79}$$

where $\Delta s = c\Delta t$, and $F^n(x^n_i, \delta f^n)$ is the force calculated from the unperturbed Gaussian beam $F_0(x^n_i)$ plus the perturbation force $\delta F^n(x^n_i, \delta f^n)$. $\delta f^{n+1}_{\text{predict}}$ is then calculated using

1	Start with $x^n, x'^n, \delta f^n, \delta f^{n-1}$
2	$\delta f^{n+1}_{\text{predict}}$ from $x^n, x'^n, \delta f^{n-1}, F^n(x^n, \delta f^n)$
3	$\delta f^{n+\frac{1}{2}}_{\text{predict}} = \frac{1}{2}(\delta f^{n+1}_{\text{predict}} + \delta f^n)$
4	$x^{n+\frac{1}{2}}, x'^{n+\frac{1}{2}}$
5	$\delta f^{n+1}_{\text{correct}}$ from $x^{n+\frac{1}{2}}, x'^{n+\frac{1}{2}} \delta f^n, F^{n+\frac{1}{2}}(x^{n+onehalf}, \delta f^{n+\frac{1}{2}}_{\text{predict}})$
6	x^{n+1}, x'^{n+1}
7	repeat steps 1-6 until the end of the interaction region
8	rotate x^{n+1}, x'^{n+1}
9	repeat steps 1-8 until the end of the simulation run

Table I: Steps for advance of δf algorithm

Eq. (66):

$$\delta f(x,x',s)^{n+1}_{\text{predict}} = \sum_{i=1}^{N} w^{n+1}_{i_{\text{predict}}} \delta(x - x_i(s))\delta(x' - x'_i(s)) \ . \tag{80}$$

The same procedure is used in step 5 to calculate $\delta f^{n+1}_{\text{correct}}$:

$$w^{n+1}_{i_{\text{correct}}} = w^n_i + \Delta \ , \tag{81}$$

$$\Delta w = -\frac{1}{n}\left[\left(F^{n+\frac{1}{2}}\left(x_i^{n+\frac{1}{2}}, \delta f^{n+\frac{1}{2}}\right) - F_0(s) x_i^{n+\frac{1}{2}}\right) \frac{\partial f_0\left(x_i^{n+\frac{1}{2}}\ ,\ x_i'^{n+\frac{1}{2}}\right)}{\partial x'}\right] \Delta s \ . \tag{82}$$

In steps 4 and 6 x and x' are advanced using Eq. (77). In step 8 x and x' are advanced using Eq. (72):

$$\begin{pmatrix} x \\ x' \end{pmatrix}^{n+1}_i = \begin{pmatrix} \cos(2\pi\nu) & \beta_0^* \sin(2\pi\nu) \\ -\dfrac{1}{\beta_0^*}\sin(2\pi\nu) & \cos(2\pi\nu) \end{pmatrix} \begin{pmatrix} x \\ x' \end{pmatrix}^{n+1}_i \ , \tag{83}$$

where

$$\nu = \nu_0 - \frac{\Delta s}{\beta_0^*} \ , \tag{84}$$

which takes into account the finite length of the interaction region Δs in the phase space rotation.

Diagnostic quantities

Analysis of the dynamics of the beam-beam interaction requires diagnostics of several quantities. Two typical accelerator quantities, the beam-beam tune shift parameter $\Delta\nu$ and the beam emittance ϵ, are calculated from the simulation. These quantities give an idea of the beam strength and beam size, respectively. Various moments of the beam are also measured to get an idea of macroscopic beam behavior. It is also important to determine the amount of particle diffusion occurring within the beams. This diffusion is measured using the method of Chirikov.[7] Each of these diagnostic quantities are described in more detail in the following sections.

Emittance

A quantity of importance to accelerator physics is beam emittance ϵ. It is a measure of phase space area occupied by the beam particles. In a Hamiltonian system phase space area is conserved and therefore, the phase space area should be conserved. The quantity often calculated in accelerator physics is the normalized emittance ϵ_n[26]:

$$\epsilon_n = (\beta\gamma)\pi\tfrac{1}{2}\frac{1}{\beta_0^*}\sum_{i=1}^{N}(x_i^2 + \beta_0^* x_i'^2) \tag{85}$$

where β and γ are the usual relativistic quantities, β_0^* is the betatron oscillation length at the interaction point, $x' = p_x/p$, p_x is the transverse momentum, p is the momentum along the collider path, and N is the number of simulation particles. By including γ, ϵ_n remains constant even during the boost or acceleration phase of the beam. In the PIC codes ϵ_n may be calculated by just summing over the number of particles. In the δf algorithm an initial unperturbed emittance is calculated:

$$\epsilon_{n_0} = (\beta\gamma)\pi\tfrac{1}{2}\frac{1}{\beta_0^*}\sum_{i=1}^{N}(x_i^2 + \beta_0^* x_i'^2)w_{0_i}\ , \tag{86}$$

where w_{0_i} is the initial unperturbed distribution function f_0 for particle i. The perturbation:

$$\delta\epsilon_n = (\beta\gamma)\pi\tfrac{1}{2}\frac{1}{\beta_0^*}\sum_{i=1}^{N}(x_i^2 + \beta_0^* x_i'^2)w_i \tag{87}$$

where w_i is the time evolving perturbation δf for particle i. This perturbation emittance is calculated and added to the initial ϵ_n to get the total ϵ_n.

Tune shift

As described in previous sections, the tune shift $\Delta\nu$ stands as a measure of the strength of the beam-beam kick. As the beams expand and contract, the kick weakens and strengthens, respectively. The various methods by which $\Delta\nu$ can be measured are described.

One method for measuring $\Delta\nu$ involves a least-squares-fit to the kicks of small and large amplitude particles. We use Sands'[32] expression for linear tune shift, which is valid for small amplitude particles:

$$\Delta\nu = \frac{\beta_0^*}{4\pi}\Delta K\,\Delta s\ , \tag{88}$$

$$\Delta K\,\Delta s = \frac{\Delta x'}{x}\ , \tag{89}$$

where $\Delta x' = \Delta p_x/p$ and $\Delta p_x = 2eE_x(x)\Delta t$. A least-squares-fit to $\Delta\nu$ can be performed:

$$(\Delta\nu)x_i = \left(\frac{\beta_0^*}{4\pi}\frac{1}{p}\right)\Delta p_{x_i} \tag{90}$$

where x_i and Δp_{x_i} are for individual particles and the average $\Delta\nu$ is given as

$$\Delta\nu = \frac{\beta_0^*}{4\pi}\frac{1}{p}\frac{A}{B}\ , \tag{91}$$

where

$$A = N\sum_{i=1}^{N} x_i\Delta p_{x_i} - \sum_{i=1}^{N} x_i \sum_{i=1}^{N}\Delta p_{x_i}\ , \tag{92}$$

$$B = N\sum_{i=1}^{N} x_i^2 - \sum_{i=1}^{N} x_i \sum_{i=1}^{N} x_i\ . \tag{93}$$

The sums are over the number of particles N used in the fit. The tune shift for small amplitude particles is measured from simulation particles lying within $0.1\sigma_0$ of the beam. Tune shifts measured using particles of the entire beam are smaller than for only small amplitude particles, since $\Delta\nu$ drops off at large amplitude. In the PIC codes the sums are carried out over the number of particles. In the δf method the sums are also carried out over the number of particles with the modifications:

$$A = N\sum_{i=1}^{N} x_i\Delta p_{x_i}w_i - \sum_{i=1}^{N} x_i w_i \sum_{i=1}^{N}\Delta p_{x_i}w_i\ , \tag{94}$$

$$B = N\sum_{i=1}^{N} x_i^2 w_i - \sum_{i=1}^{N} x_i w_i \sum_{i=1}^{N} x_i w_i\ , \tag{95}$$

where w_i is the total distribution function value $f(x,x') = f_0(x,x') + \delta f(x,x')$ for particle i.

Another method for calculating $\Delta\nu$ uses the electric field $E_x(x)$. This can be done at one point x in the beam or as an average over several points. For one point:

$$\Delta\nu = \frac{\beta_0^*}{4\pi}\,\Delta K\,\Delta s\ , \tag{96}$$

$$\Delta K = \frac{2eE_x(x)}{\gamma m v^2}\,\frac{1}{x}\ , \tag{97}$$

and for several points:

$$\Delta\nu = \frac{\beta_0^*}{4\pi}\,\Delta K\,\Delta s\ , \tag{98}$$

$$\Delta K = \frac{1}{N}\sum_{i=1}^{N}\frac{2eE_x(x_i)}{\gamma m_i v_i^2}\,\frac{1}{x_i}\ , \tag{99}$$

where the sum is over N particles. The tune shift $\Delta\nu$ is calculated in the δf algorithm at one point from Eq. (97) by using $E_x(x) = E_{x_0}(x) + \delta E_x(x)$, where $E_{x_0}(x)$ is the unperturbed field and $\delta E_x(x)$ is the perturbation field. For several points in the δf method Eq. (99) becomes:

$$\Delta\nu = \frac{\beta_0^*}{4\pi}\,\Delta K\ \Delta s\ , \tag{100}$$

$$\Delta K = \sum_{i=1}^{N}\frac{2eE_x(x_i)}{\gamma m_i v_i^2}\,\frac{1}{x_i}\,w_i\sum_{i=1}^{N}w_i\ , \tag{101}$$

where w_i is the total distribution function value $f(x,x') = f_0(x,x') + \delta f(x,x')$ for particle i.

The power spectra of the x position of sample particles are another diagnostic method. The x positions are sampled after each complete turn around the collider. The power spectral density $P(\nu)$ is calculated from[29]:

$$P(\nu) = \int_{-\infty}^{\infty} dn'\,\exp(-in'\nu)C(n')\ , \tag{102}$$

where n refers to the turn number and $C(n)$, the autocovariance function, is given by:

$$C(n') = \lim_{N\to\infty}\left\{\frac{1}{2N}\int_{-N}^{+N} x(n)\ x^*(n+n')dn\right\}\ , \tag{103}$$

where n' is the lag in the number of rotations. The previous expression assumes that $x(n)$ is a continuous function of n. In the simulations, $C(n')$ is calculated from a discrete set of values[18]:

$$C(r) = \frac{1}{N-r} \sum_{n=1}^{N-r} x(n)x^*(n+r) \ , \tag{104}$$

where $r = 0, ..., m$, r is the rotation lag, m is the maximum rotation lag, and N is the total number of rotations. The autocovariance function may be calculated using an FFT with $N = 2^k$. The maximum rotation lag was constrained to be less than $0.25\,N$ for accuracy. The power spectral density is calculated by:

$$P(\nu) = \mathrm{FFT}[C(r)W(r)] \tag{105}$$

where $W(r)$ is the window function, the Parzen lag weighting functions.[28] The tune shift can be determined from the frequency shift in the power spectral peak. The frequency spectrum peaks at the unperturbed tune ν_0 when the beam-beam interaction is not present. The error in measuring the tune shift $\Delta\nu$ is given by:

$$\delta(\Delta\nu) = \frac{2}{m} \ , \tag{106}$$

where m is the maximum lag in rotations.

Determination of beam moments

Other quantities of importance in diagnosing beam dynamics are the beam moments. The beam moments may be studied in two different approaches. One way involves calculating the cumulants of the particle positions x for each beam[24]:

$$\langle x \rangle = \frac{1}{N} \sum_{i=1}^{N} x_i \tag{107}$$

$$\left\langle x^2 \right\rangle = \frac{1}{N} \sum_{i=1}^{N} (x_i - \langle x \rangle)^2 \tag{108}$$

$$\left\langle x^3 \right\rangle = \frac{1}{N}\sum_{i=1}^{N}(x_i - \langle x \rangle)^3 \tag{109}$$

$$\left\langle x^4 \right\rangle = \frac{1}{N}\sum_{i=1}^{N}(x_i - \langle x \rangle)^4 - 3(x_i - \langle x \rangle)^2 \ , \tag{110}$$

where N is the number of particles. In the δf technique the cumulants are calculated:

$$\langle x \rangle = \frac{1}{N}\sum_{i=1}^{N} x_i w_i \tag{111}$$

$$\left\langle x^2 \right\rangle = \frac{1}{N}\sum_{i=1}^{N}(x_i - \langle x \rangle)^2 w_i \tag{112}$$

$$\left\langle x^3 \right\rangle = \frac{1}{N}\sum_{i=1}^{N}(x_i - \langle x \rangle)^3 w_i \tag{113}$$

$$\left\langle x^4 \right\rangle = \frac{1}{N}\sum_{i=1}^{N}(x_i - \langle x \rangle)^4 w_i - 3(x_i - \langle x \rangle)^2 w_i \ . \tag{114}$$

Power spectra of the cumulants give the frequency components which contribute to each mode.

Determination of diffusion

In this section a method to calculate the diffusion of particles is presented. Diffusion coefficients may be calculated in the following manner[7, 4]:

$$D_k = \frac{2}{N_k(N_k - 1)} \sum_{m>l} \frac{[\overline{X}(m) - \overline{X}(l)]^2}{(\Delta N_k)(m - l)} \ , \ k = 1, 2 \tag{115}$$

where N_k is the number of subintervals, ΔN_k is the size of the subinterval in terms of rotations, k refers to the subinterval type, and $\overline{X}(m)$ is the average of x_n over the subinterval m:

$$\overline{X}(m) = \frac{1}{\Delta N_k}\sum_{n=1}^{\Delta N_k} \left| \frac{x_{l+n}}{\sigma_x} \right| \ . \tag{116}$$

where $l = m\,\Delta N_k$. The total number of rotations is broken up into two different subinterval sizes. Diffusion coefficients are calculated for each different subinterval. If we find the

coefficients computed with different sampling intervals,

$$D_1 \approx D_2 \ , \tag{117}$$

then the motion x is diffusive. This occurs since a diffusive process should be independent of the number of subintervals. On the other hand, if the initial conditions are chosen within "islands" of stable oscillatory motion : $[\overline{X}(m) - \overline{X}(l)] \propto (\Delta N_k)^{-1}$, then

$$\frac{D_2}{D_1} \propto \frac{(\Delta N_1)^3}{(\Delta N_2)^3} < 1 \ . \tag{118}$$

The average in Eq. (116) is intended to lower the influence of bounded energy oscillations and pick out accumulating changes.[7] The averaging made over all pair combinations of intervals is intended to increase the time scale for which diffusion is described by the raten and facilitates the separation of diffusion processes from side effects. The mean value of Δt is about half the total time and is independent of the length of the interval Δt_n.[7]

Simulation Results

In this chapter we describe results of the study of the beam-beam interaction with the various codes which have been developed. Beam-beam collective effects are examined using the strong-strong code, and δf code. Particle diffusion is also examined with the use of all the codes. A comparison of the different codes is made.

Collective beam-beam effects

In this section the object is to describe the effects of the beam-beam interaction on macroscopic beam behavior, that is, phenomena which deal with the entire beam such as beam blowup.

$l \times w \times h$	=	7.5cm $\times 10^{-3}$ cm $\times 10^{-3}$ cm
N_B	=	7.3×10^9
T	=	20 Tev protons
β^*	=	50 cm
$\Delta\nu_{HO}$	=	$.84 \times 10^{-3}$
ν_{HO}	=	0.285
Luminosity	=	10^{33} cm^{-2} s^{-1}
Lifetime	=	24 hours or 10^8 turns

Table II: SSC Parameters

Reference parameters

Our research is generic enough to cover the beam-beam interaction of various colliders or storage rings. We make specific reference to the parameters of the SSC. Table 2 shows parameters for the SSC. Using the numbers from the table we have: $\gamma = 2.13 \times 10^4$ and $\omega_b \tau_{\text{int}} = 0.035$ where $\omega_b = \sqrt{4\pi e^2 n_b/\gamma m_b}$, $n_b = N_B/(lwh)$ is the beam density, m_b is the mass of the beam particles (protons), γ is the relativistic factor, and $\tau_{\text{int}} = L/2c$ is the interaction time of the colliding beams. The horizontal tune shift $\Delta\nu_{HO}$ is calculated for a two dimensional Gaussian beam. Since the present simulations deal with only one dimension, this quantity is recalculated. Using the equation for the one dimensional tune shift:

$$\Delta\nu_0 = \sqrt{\frac{2}{\pi}} \frac{\beta^* r_p N_B}{\gamma h w} , \tag{119}$$

and using values from Table 2, the one dimensional tune shift is $\Delta\nu_0 = 2.1 \times 10^{-3}$.

A series of simulation runs is performed using the parameters described in Table 2.

Strong-strong simulation results

A series of strong-strong simulations have been performed to determine long time characteristics. The initial distribution of particles is shown in Fig. 4. In this run 10^4 particles are used in each beam with variable charge per particle initially to maintain a Gaussian

distribution. The tune $\nu_0 = 0.285$ and the tune shift $\Delta\nu_0 = 2.1 \times 10^{-3}$. The simulation box size is 128Δ where Δ is the cell size. The beam width w is 30Δ and the particle size a is Δ. The particle size a is small enough in relation to the beam width w so that from Eq. (13):

$$\frac{\Delta\nu_{\text{point}}}{\Delta\nu_{\text{fsp}}} = 1.0022 \,, \tag{120}$$

where $\Delta\nu_{\text{point}}$ is the tune shift for a point particle and $\Delta\nu_{\text{fsp}}$ is the tune shift for a finite size particle. Thus, finite size particle effects on the kicks that the simulation particles receive are minimal. By normalizing the code to a plasma with density lower than the beam where ω_0 is the normalization plasma frequency and ω_b is the beam plasma frequency, only 4 simulation time steps are needed to cover the interaction region. So $\omega_0\Delta t = 0.25$ where Δt is the simulation time step size.

Figure 9 shows the distribution of 10^4 particles in $(x/\sigma_x, p_x/\sigma_p)$ phase space for one beam after 10240 rotations. The particles were initialized using the nonuniform charge distribution [Fig. 4]. After 10240 rotations the particles are no longer uniformly distributed in $(x/\sigma_x, p_x/\sigma_p)$ space. Clumping of particles has occurred and small regions contain no particles. However, no dominant mode such as a $m = 2$ mode (football shape) or $m = 4$ mode (square shape) has appeared, which would distort the shape of the whole beam. A profile in x of the distribution of particles in Fig. 10 shows the deviation of the distribution from the initial Gaussian profile. The center of the beam is at $x = 64\Delta$. Large spikes in the distribution are visible at $x \approx 50\Delta$ and $x \approx 80\Delta$.

We measure the tune shift $\Delta\nu$ by two methods described in Sec. 2. One method involves a least-squares-fit to the kicks of small and large amplitude particles.

Results from the least-squares-fit method for one beam are shown in Fig. 11. The fit is done for small amplitude particles $x < 0.1\sigma_x$ at the top of the figure and for the entire beam for the bottom of the figure. The tune shift $\Delta\nu$ oscillates around the unperturbed values of $\Delta\nu_0 = 2.1 \times 10^{-3}$ for small amplitude particles and $\Delta\nu_0 \approx 1.55 \times 10^{-3}$ for all the particles.

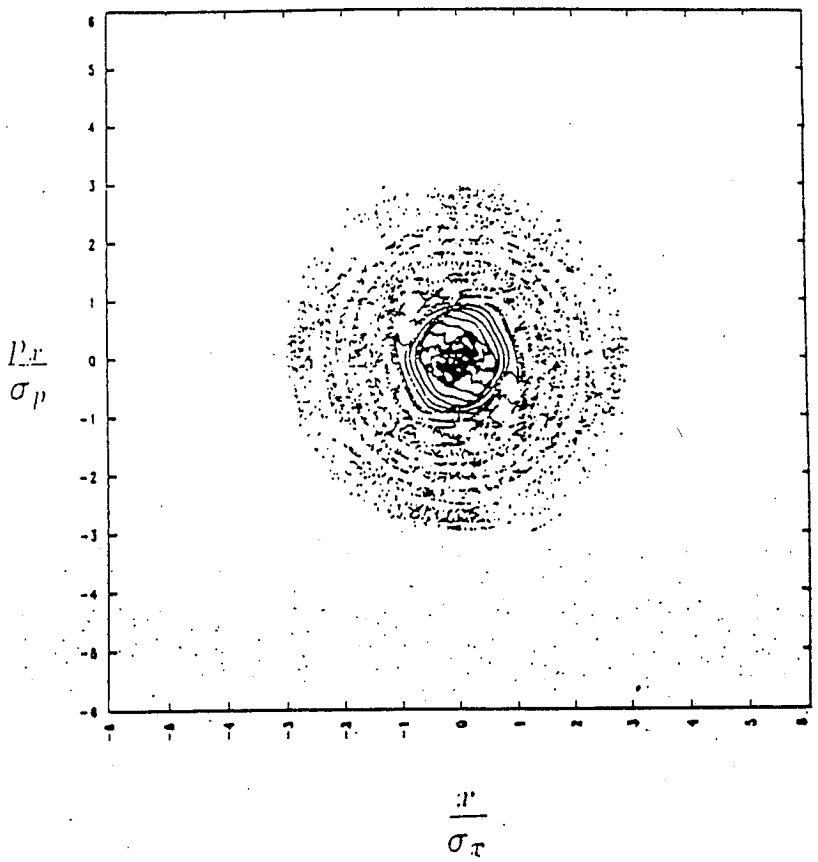

Figure 9: Distribution of 10^4 simulation particles in $(x/\sigma_x, p_x/\sigma_p)$ space after 10240 rotations with $\nu_0 = 0.285$ and $\Delta\nu_0 = 2.1 \times 10^{-3}$.

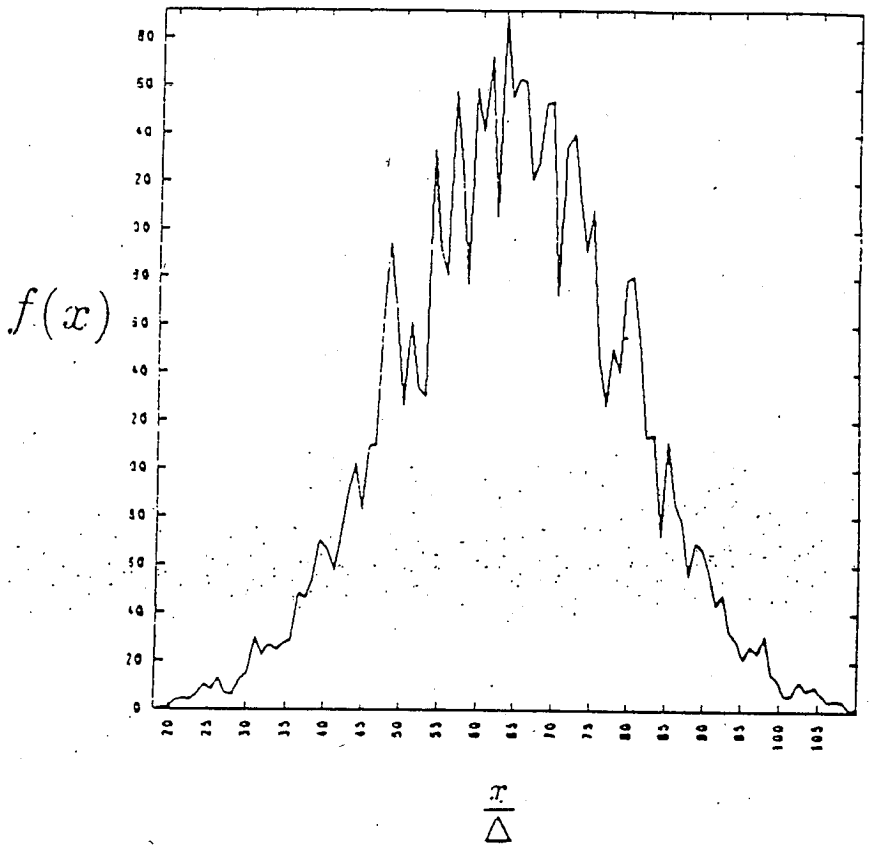

Figure 10: Distribution of 10^4 simulation particles in x after 10240 rotations with $\nu_0 = 0.285$ and $\Delta\nu_0 = 2.1 \times 10^{-3}$.

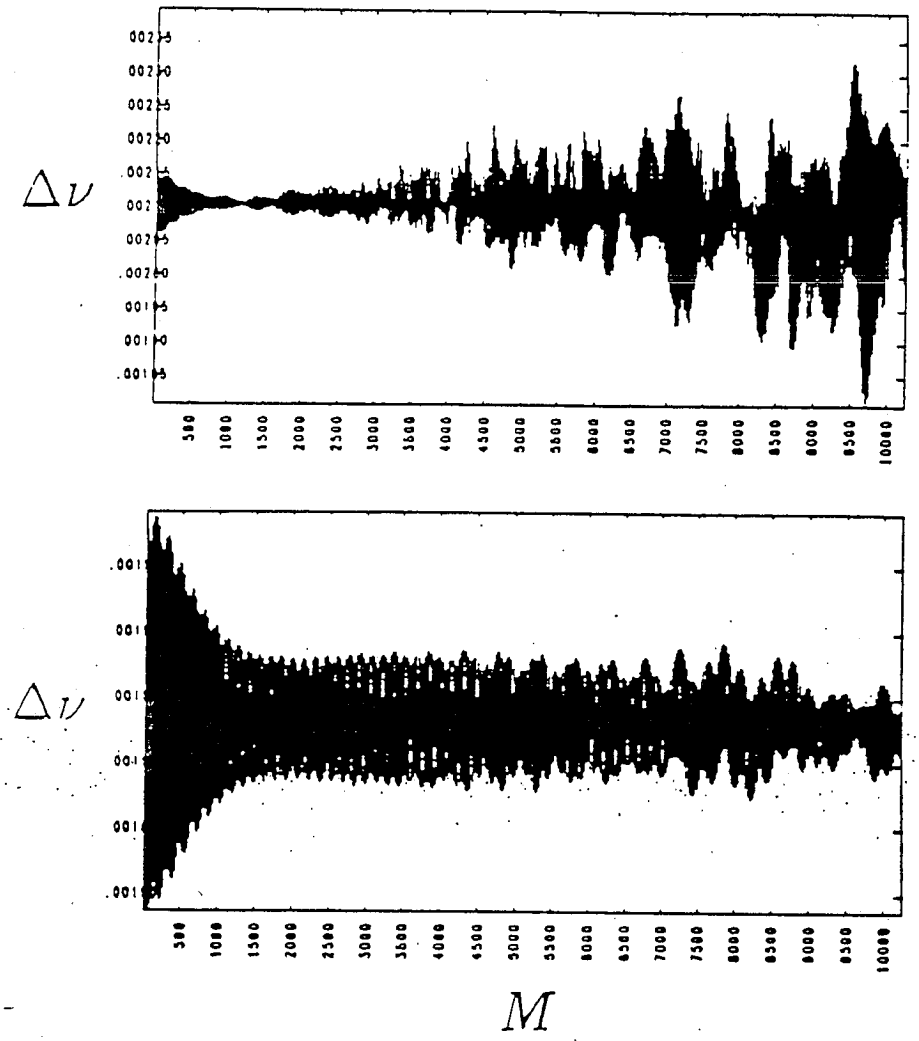

Figure 11: Tune shift $\Delta\nu$ from a least squares fit to small amplitude particles $x < 0.1\sigma_x$ (top) and all particles (bottom) for $M = 10240$ rotations

The discrepancy is due to the drop-off of the kick at large values of x. When all particles are included in the least-squares-fit, the measured $\Delta\nu$ is lowered by the particles with large x. The amplitude of the variation in $\Delta\nu$ for small amplitude particles is approximately $\pm 20\%$ of $\Delta\nu_0$ near the end of the run. The tune shift obtained from all particles decreases in amplitude with the number of rotations. The maximum variation of $\Delta\nu$ is approximately $\pm 3\%$ of its average value and occurs within the first 500 rotations. The oscillations in $\Delta\nu$ indicate expansion and contraction of the beam. The expansion and contraction of the beam decreases and increases $\Delta\nu$, respectively. Notice that the beam is expanding and contracting differently at different particle positions. The small amplitude portion of the beam is increasing in oscillation amplitude, while the entire beam is decreasing in oscillation amplitude.

The other method by which the tune shift $\Delta\nu$ is measured is by getting power spectra of the x positions of sample particles which are sampled once every complete rotation. Figures 12 and 13 show the particle positions and power spectra for a small and large amplitude particle, respectively. The tune shift $\Delta\nu$ is measured from the shift in the power spectral peak from the unperturbed tune ν_0. The small amplitude particle in Fig. 12 shows smearing in the particle position in phase space, which is indicative of particle diffusion which will be discussed in Sec. 3. The peaks in $S(\nu)$ are at $\nu = \pm 0.2827148$. The difference from ν_0 is 2.2852×10^{-3}. The error in this measurement is $\delta\nu = 7.8125 \times 10^{-4}$, where the maximum lag time is 2560 rotations for the power spectrum calculation. Although the value is higher than the unperturbed tune shift $\Delta\nu_0$, it is within the errors of the calculation. The large amplitude particle in Fig. 13 also shows smearing in the particle position in phase space, but it is less than that observed for the small amplitude particle. The peaks in $S(\nu)$ are at $\nu = \pm 0.2832031$. The difference from ν_0 is 1.7969×10^{-3}. The error in this measurement is also $\delta\nu = 7.8125 \times 10^{-4}$. The tune shift, $\Delta\nu$, for the large amplitude particle is smaller than the one measured for the small amplitude particle, since $\Delta\nu$ drops off with large x for the

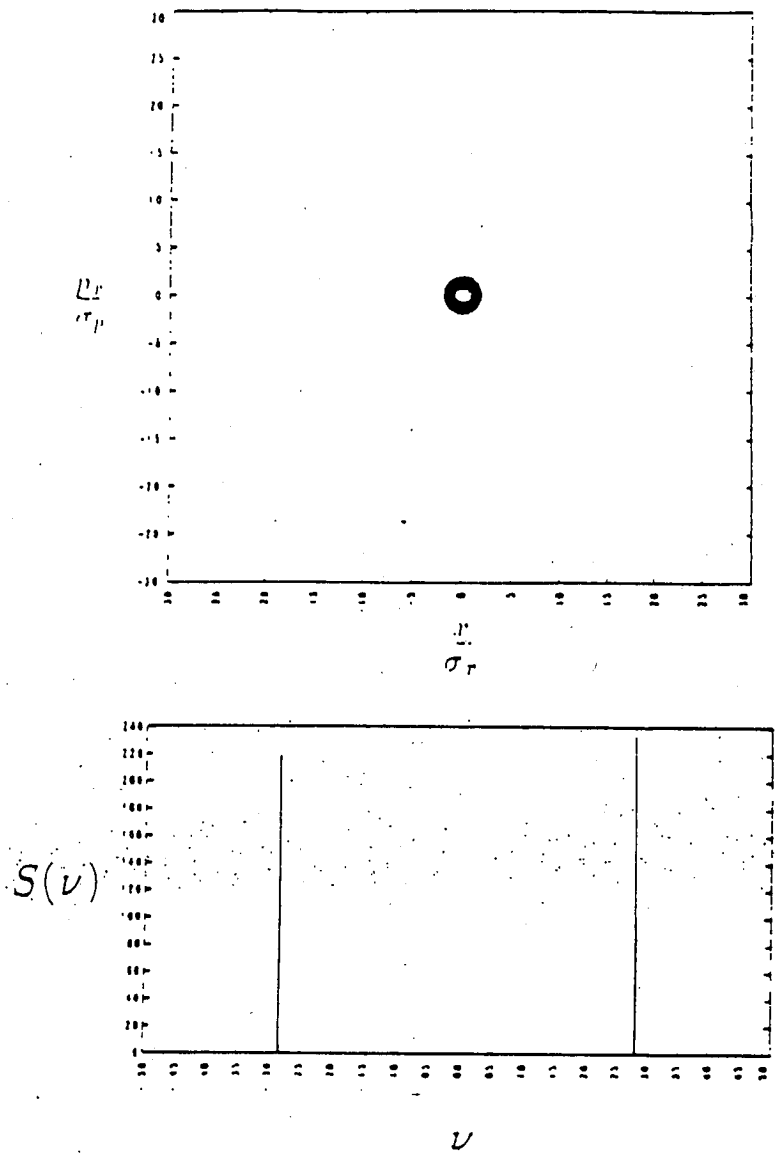

Figure 12: Position of an initially small amplitude particle $x_0 = 0.1\sigma_x$ in $(x/\sigma_x, p_x/\sigma_p)$ space for $M = 10240$ rotations (top) and power spectrum of x position of the particle versus ν (bottom).

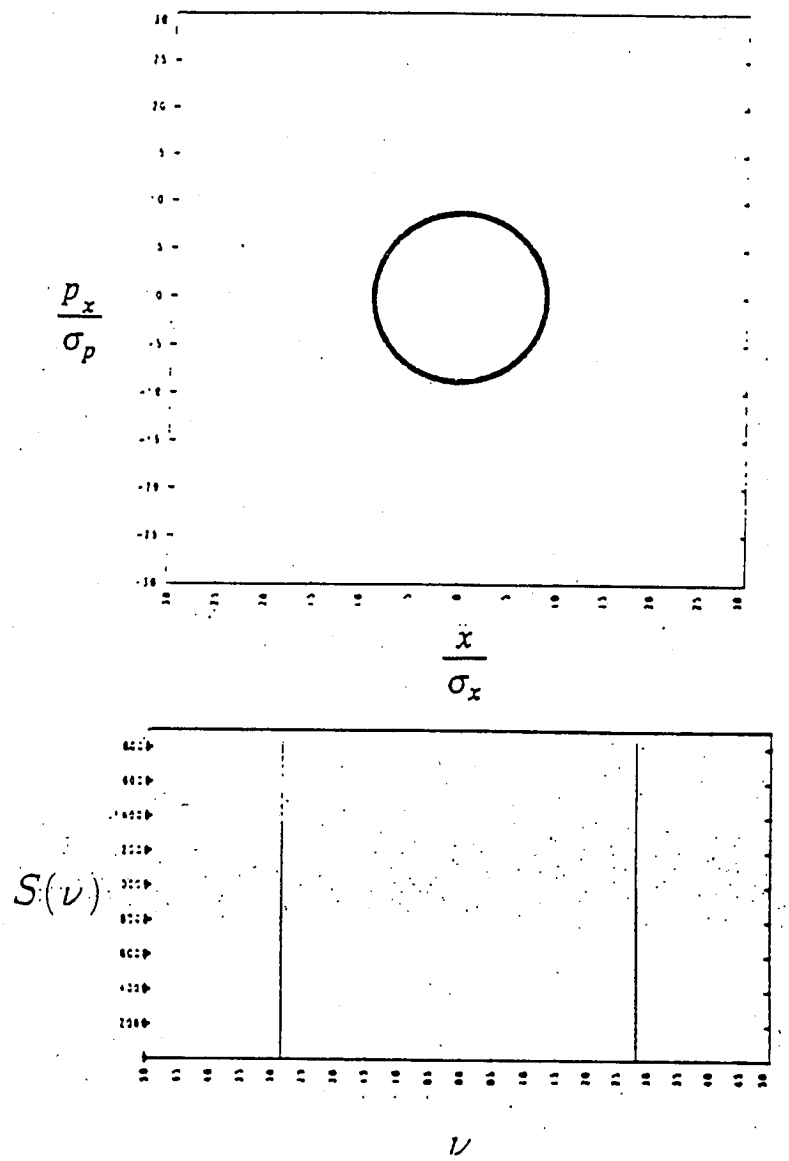

Figure 13: Position of an initially large amplitude particle $x_0 = 0.9\sigma_x$ in $(x/\sigma_x, p_x/\sigma_p)$ space for $M = 10240$ rotations (top) and power spectrum of x position of the particle versus ν (bottom).

beam-beam interaction.

Moments of one beam are shown in Figs. 14 and 15. At the top of Fig. 15 the oscillation of the average beam center $\langle x \rangle$ is apparent. The beam oscillates with a maximum beam amplitude of $\delta x/\sigma_x \approx \pm 8 \times 10^{-4}$. The average $\langle x \rangle$ and $\langle (x - \langle x \rangle)^3 \rangle$, the odd moments, are both increasing in oscillation amplitude with rotation number. The increase is more obvious for $\langle (x - \langle x \rangle)^3 \rangle$ at the bottom of Fig. 16. At the top of Fig. 15 the oscillation of the beam width can be seen. The beam is oscillating about the initial beam width σ_x^2 with a maximum amplitude of approximately $\pm 0.04\sigma_x^2$. Oscillations are also apparent for $\langle (x - \langle x \rangle)^4 \rangle$ at the bottom of the figure. The amplitudes of the even moments $\langle (x - \langle x \rangle)^2 \rangle$ and $\langle (x - \langle x \rangle)^4 \rangle$ are both decreasing with the number of rotations. Note that the variation in the second moment $\langle (x - \langle x \rangle)^2 \rangle$ closely corresponds with the variation of the tune shift measured from all beam particles in Fig. 11. Both $\Delta\nu$ and $\langle (x - \langle x \rangle)^2 \rangle$ give a measure of the width of the kicking beam and the kicked beam, respectively. Since both beams are oscillating in width in the same manner, the agreement is expected.

Figures 16 and 17 show the moments and their associated power spectra. The power spectra of the average of x, $\langle x \rangle$, is shown at the bottom of Fig. 16. There is a peak in $S(\nu)$ at $\nu \approx 0$. This peak corresponds to oscillations seen in $\langle x \rangle$ with periods between 500 and 1000 rotations. The smaller peaks at $\nu \approx \pm(\nu_0 - \Delta\nu_0)$ correspond to the betatron motion. In Fig. 17 the peaks in the power spectra $S(\nu)$ at $\nu \approx \pm(1 - 2(\nu_0 - \Delta\nu_0))$ also correspond to the betatron motion of the beam.

The emittance ϵ of each beam for 10240 rotations is shown in Fig. 18. The emittance for one beam is at the top of the figure and the other is at the bottom. Until about 6000 rotations the beams show similar behavior. They oscillate about the initial emittance $\epsilon_0 = 9.586\Delta$. After this the beams begin to deviate from one another. One beam is decreasing in phase space area and the other beam is increasing. This phenomena is similar to the "flip-flop" effect observed experimentally with equal strength beams.[19] One beam blows up and the

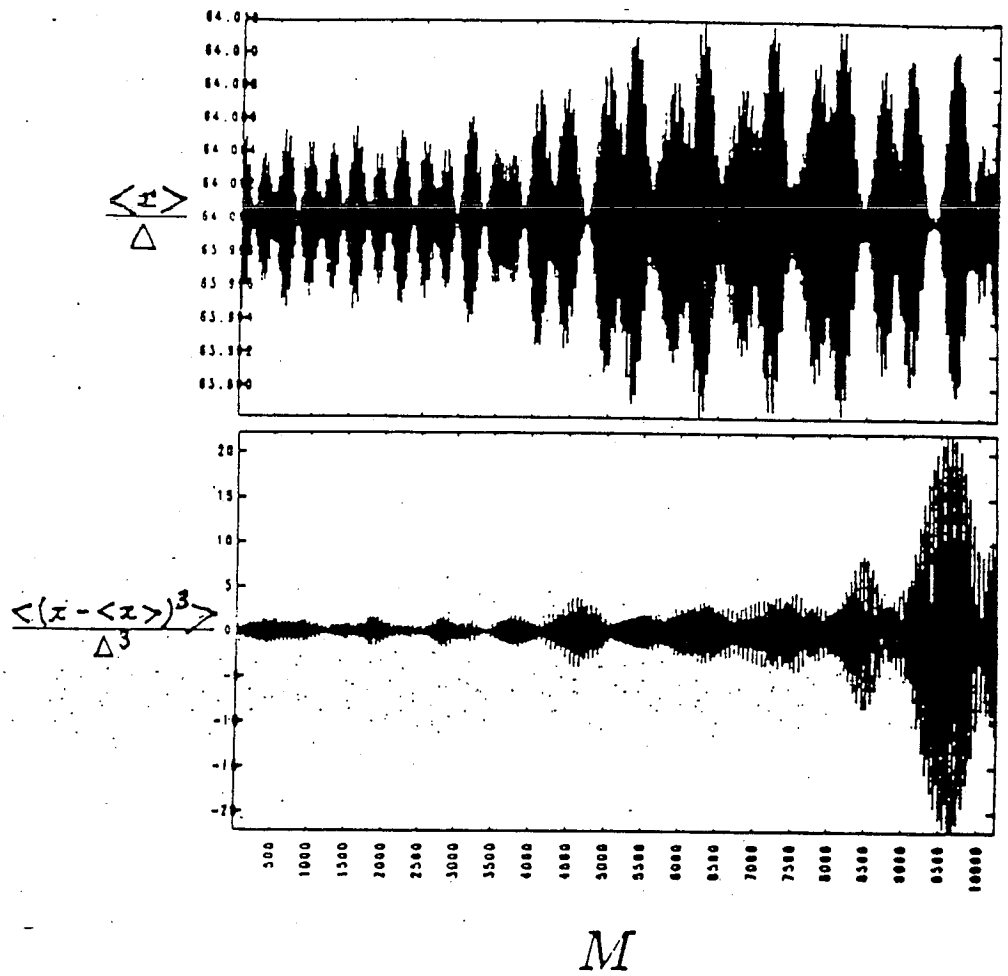

Figure 14: Beam moments $\langle x \rangle$ and $\langle (x - \langle x \rangle)^3 \rangle$ for $M = 10240$ rotations at the top and bottom of the figure respectively.

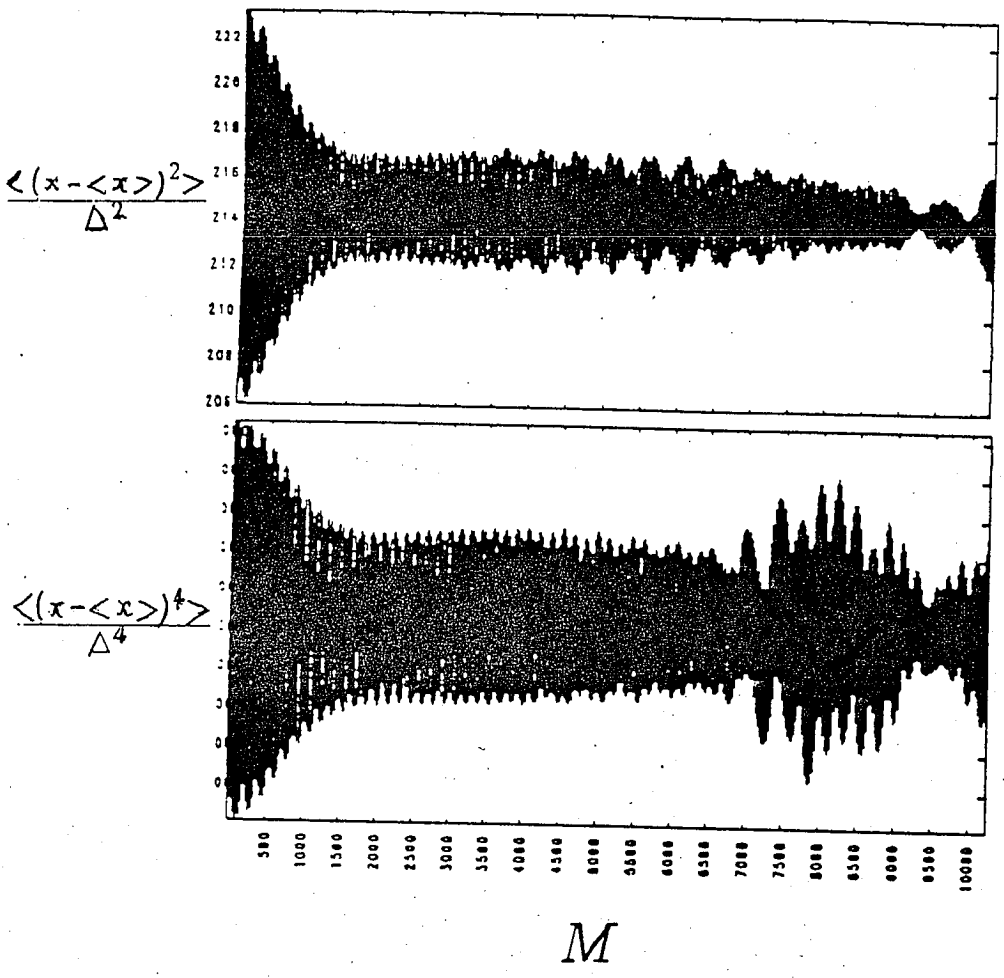

Figure 15: Beam moments $\langle (x - \langle x \rangle)^2 \rangle$ and $\langle (x - \langle x \rangle)^4 \rangle$ for $M = 10240$ at the top and bottom of the figure respectively.

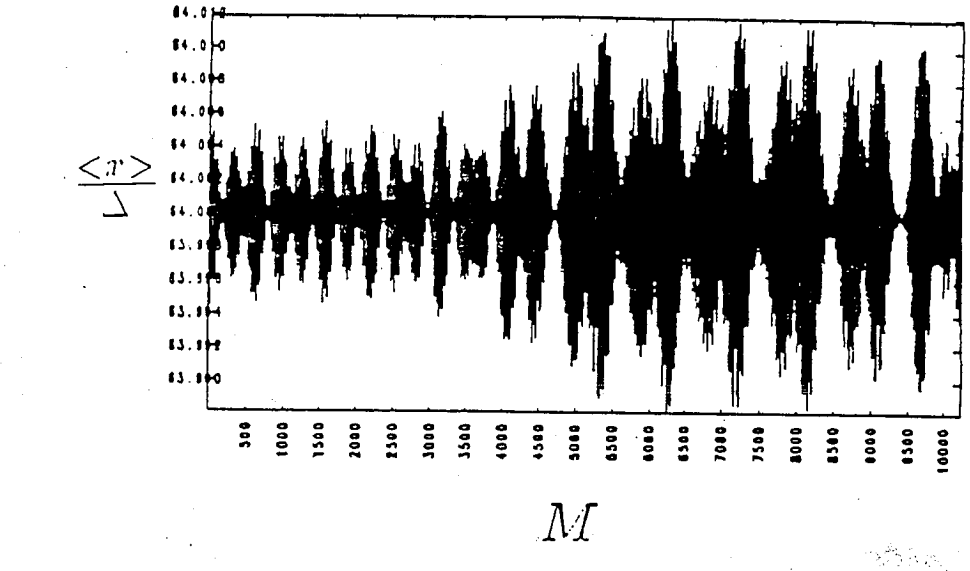

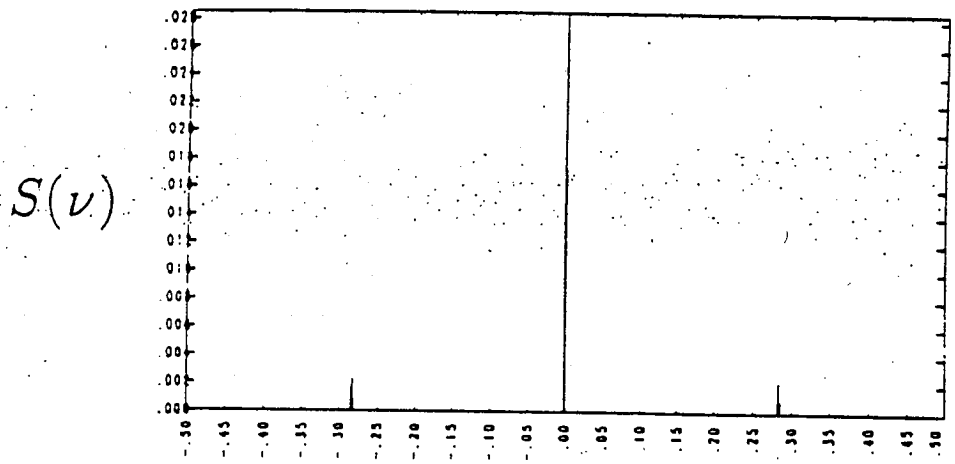

Figure 16: Beam moment $\langle x \rangle$ and power spectrum $S(\nu)$ for $M = 10240$ rotations at the top and bottom of the figure respectively.

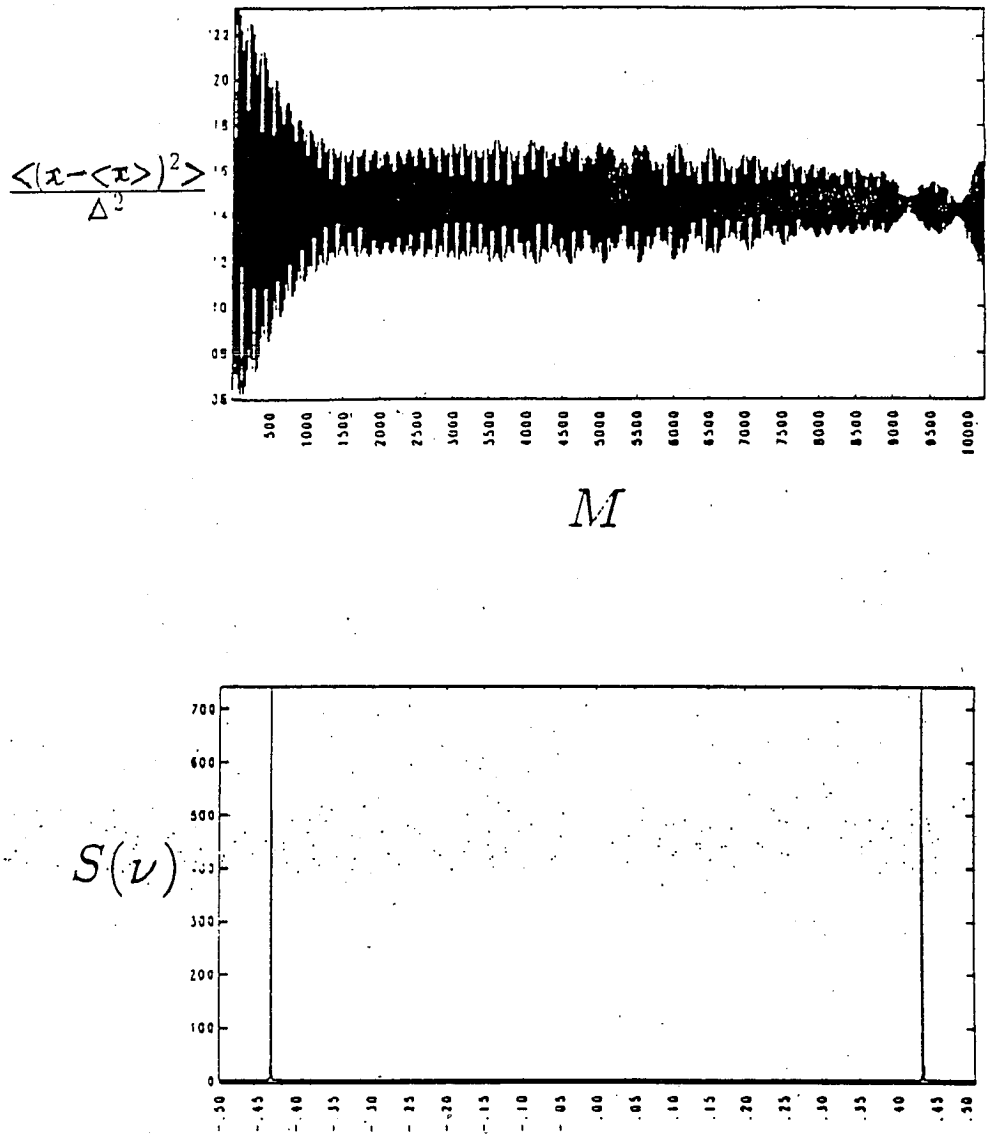

Figure 17: Beam moment $\langle (x - \langle x \rangle)^2 \rangle$ and power spectrum $S(\nu)$ for $M = 10240$ rotations at the top and bottom of the figure respectively.

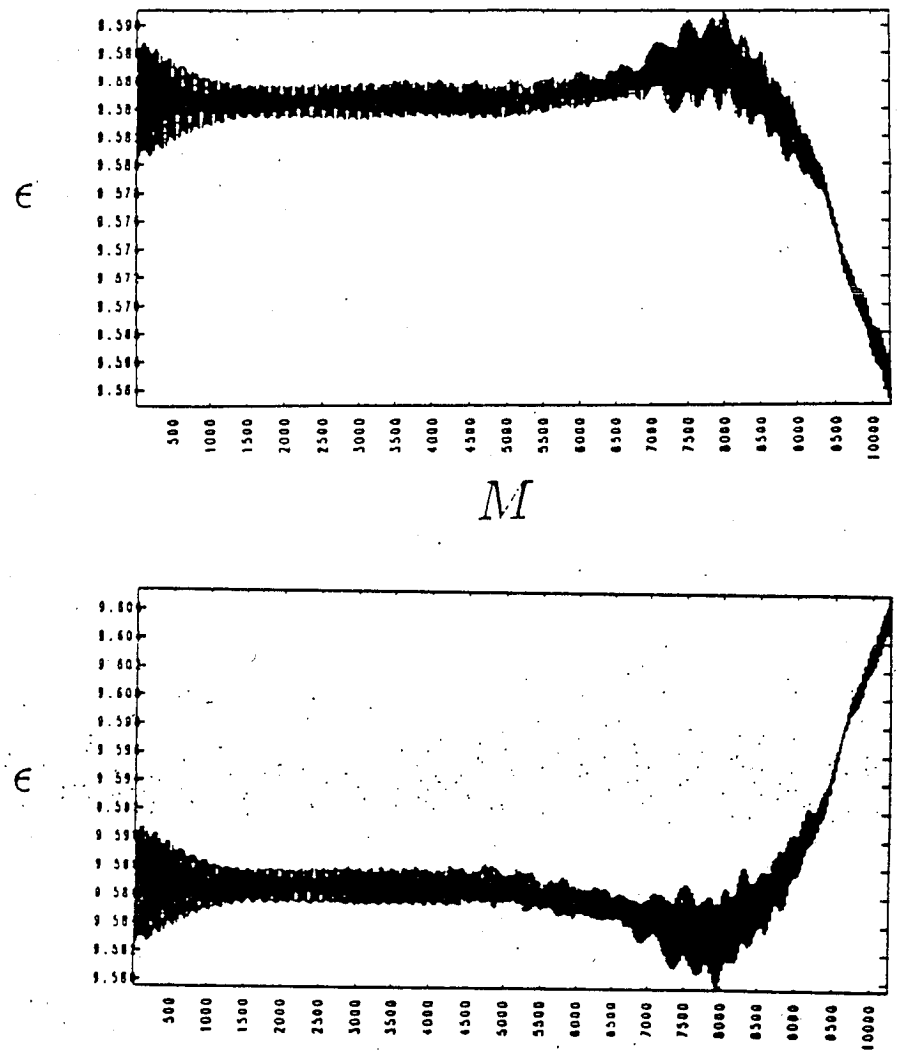

Figure 18: The emittance ϵ of both beams for 10240 rotations. One beam is at the top and the other beam is at the bottom of the figure

other decreases in size. The difference in ϵ is small between the two beams. By the end of the run it is $\delta\epsilon/\epsilon_0 = 4.4 \times 10^{-3}$. This variation in ϵ is very sensitive to the initial conditions. Figure 19 shows the emittance for both beams when the distribution is initialized with different random offsets in θ for the nonuniform charge distribution. The increments in r/σ are the same. The beams begin to deviate from one another at about 9000 rotations. The deviation is much smaller than the previous case. By the end of the run it is $\delta\epsilon/\epsilon_0 = 5 \times 10^{-4}$.

Runs with the uniform charge and nonuniform position initialization show different behavior than the runs with nonuniform charge and uniform position. Figure 20 shows the distribution of 10^4 particles in $(x/\sigma_x, p_x/\sigma_p)$ phase space for one beam after 10240 rotations. The particles were initialized using the uniform charge distribution [Fig. 6]. After 10240 rotations the particle distribution shows spiral arms in $(x/\sigma_x, p_x/\sigma_p)$ space. However, no dominant mode such as a $m = 2$ mode (football shape) or $m = 4$ mode (square shape) has appeared which is distorting the shape of the whole beam. A profile in x of the distribution of particles in Fig. 21 shows the deviation of the distribution from the initial Gaussian profile. The center of the beam is at $x = 64\Delta$. The profile is much smoother than the profile from the nonuniform charge distribution run [Fig. 10].

Results from the least-squares-fit method for one beam are shown in Fig. 22 The fit is done for small amplitude particles $x < 0.1\sigma_x$. $\Delta\nu$ oscillates around the unperturbed tune shift values of $\Delta\nu_0 = 2.1 \times 10^{-3}$ for small amplitude particles. It is found that $\Delta\nu \approx 1.55 \times 10^{-3}$ for all the particles. The discrepancy is due to the drop-off of $\Delta\nu$ at large values of x. When all particles are included in the least squares fit, the measured $\Delta\nu$ is lowered by the particles with large x. The amplitude of the variation in $\Delta\nu$ for small amplitude particles is approximately $\pm 3\%$ of $\Delta\nu_0$ near the end of the run, which is about a factor of 6 smaller than the deviations observed in the nonuniform charge run. The tune shift $\Delta\nu$ obtained from all particles decreases in amplitude with the number of rotations. The maximum variation of $\Delta\nu$ is approximately $\pm 3\%$ of its average value and occurs within the first 500 rotations. The

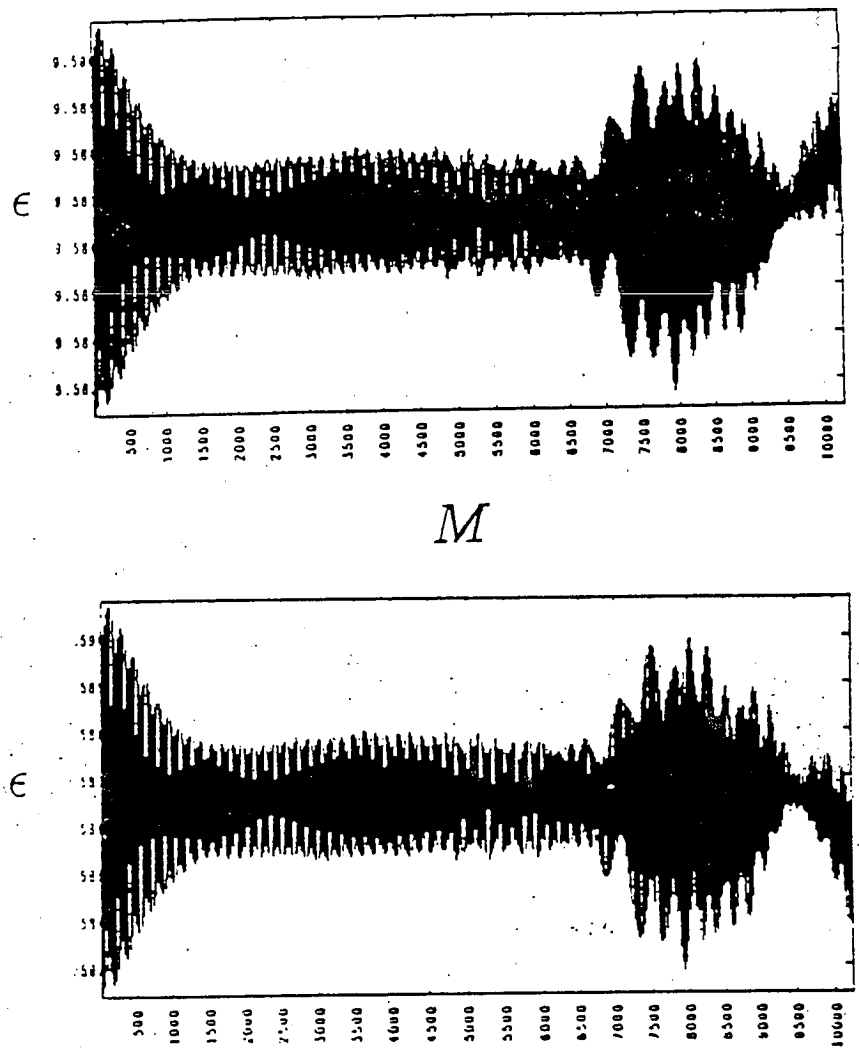

Figure 19: The emittance ϵ of both beams for 10240 rotations with a slightly different initialization. One beam is at the top and the other beam is at the bottom of the figure

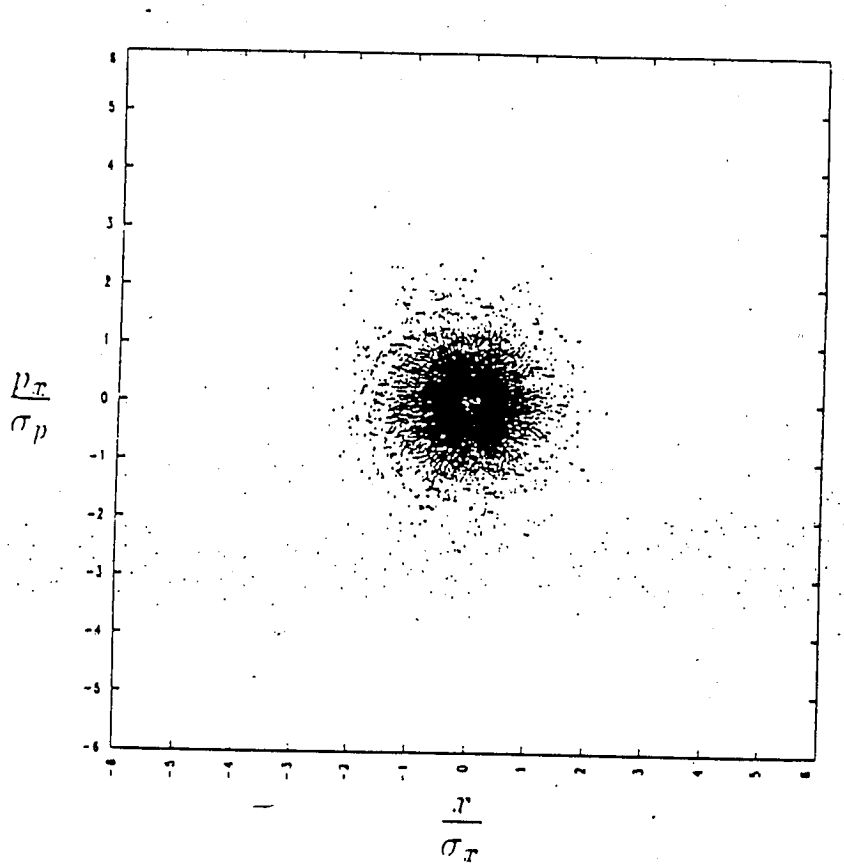

Figure 20: Distribution of 10^4 simulation particles in $(x/\sigma_x, p_x/\sigma_p)$ space after 10240 rotations with $\nu_0 = 0.285$ and $\Delta\nu_0 = 2.1 \times 10^{-3}$.

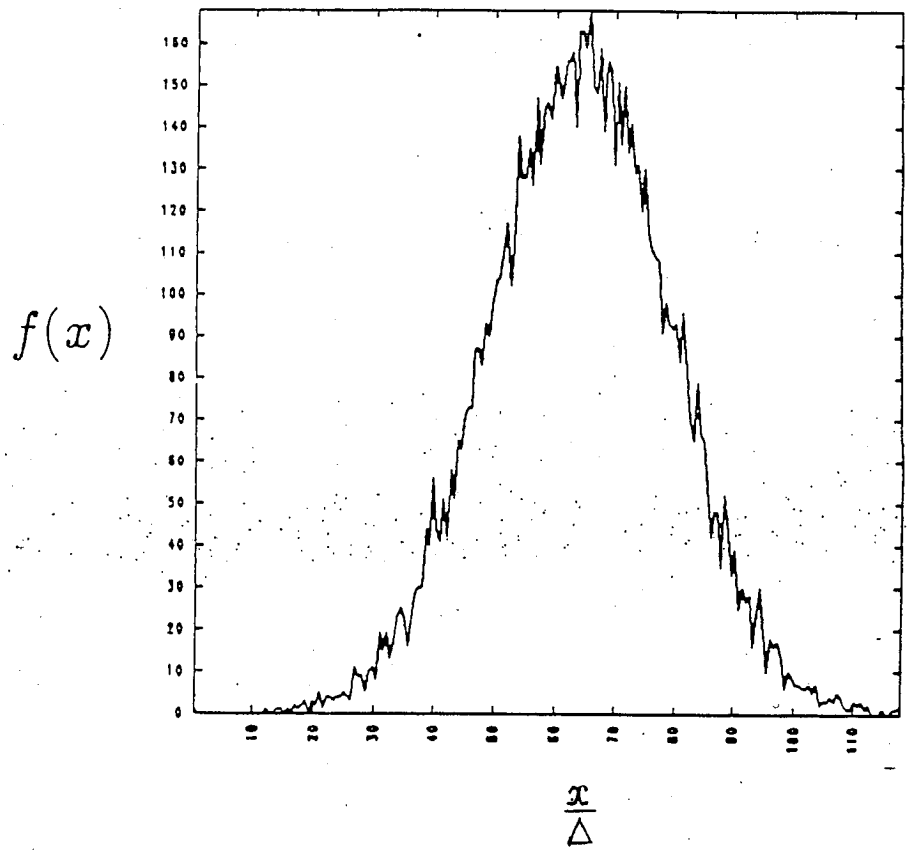

Figure 21: Distribution of 10^4 simulation particles in x after 10240 rotations with $\nu_0 = 0.285$ and $\Delta\nu_0 = 2.1 \times 10^{-3}$.

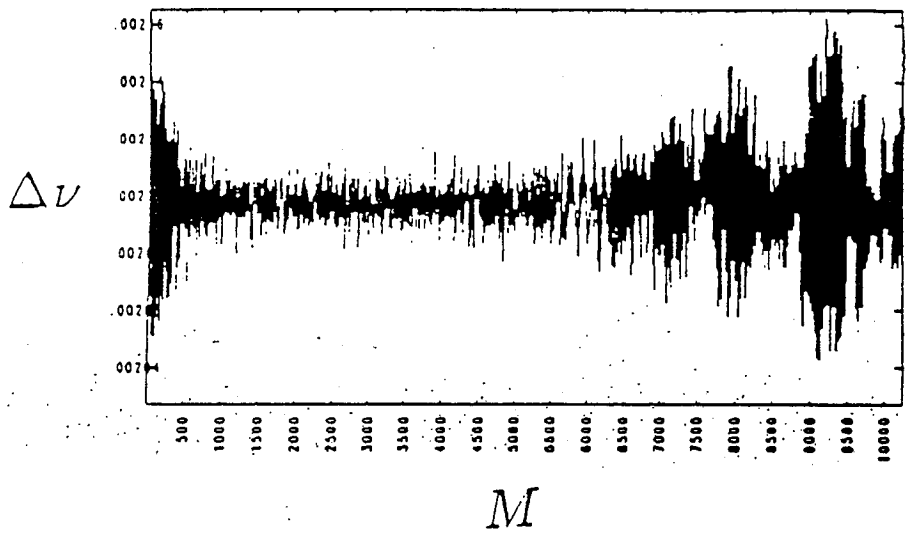

Figure 22: Tune shift $\Delta\nu$ measured from a least squares fit to small amplitude particles $x < 0.1\sigma_x$ for $M = 10240$ rotations

oscillations in $\Delta\nu$ indicate that the expansion and contraction of the beam which is kicking the particles is smaller than the nonuniform charge runs.

The emittance ϵ of each beam for 10240 rotations is shown in Fig. 23. The emittance for one beam is at the top of the figure and the other at the bottom. In this case the beams are oscillating in ϵ. The amplitude of the oscillations is largest for the first 1000 rotations. The magnitude of these oscillations is $\delta\epsilon/\epsilon_0 \approx 10^{-3}$, where ϵ_0 is the initial emittance. By the end of the run the oscillations are $\delta\epsilon/\epsilon_0 \approx 10^{-4}$.

A. δf simulation results

A series of δf simulations have been performed to determine long time characteristics. We use 10^3 particles in the runs. The fluctuation level δ expected for the actual SSC beam is $\delta \approx 10^{-5}$ for 10^{10} particles. Figure 24 shows the variation with particle number of the minimum and maximum perturbations $\delta f/f_0$ for runs with 10240 rotations. We see that the maximum perturbation is nearly independent of particle number. The minimum fluctuation value decreases exponentially with increasing particle number. It can be seen that the minimum perturbation drops below 10^{-5} for simulations with 10^3 particles and larger. Because 10^3 particles could be used, larger rotations of 10^5 could be run. The initial distribution of particles is shown in Fig. 3. In this run 10^3 particles are used in each beam with variable charge per particle initially to maintain a Gaussian distribution. The tune $\nu_0 = 0.285$ and the tune shift $\Delta\nu_0 = 2.1 \times 10^{-3}$. The simulation box size is 128Δ where Δ is the cell size. The beam width w is 30Δ and the particle size a is Δ. The particle size a is small enough in relation to the beam width w so that from Eq. (13):

$$\frac{\Delta\nu_{\text{point}}}{\Delta\nu_{\text{fsp}}} = 1.0022\,, \tag{121}$$

where $\Delta\nu_{\text{point}}$ is the tune shift for a point particle and $\Delta\nu_{\text{fsp}}$ is the tune shift for a finite size particle. Thus, finite size particle effects on the kicks that the simulation particles receive are

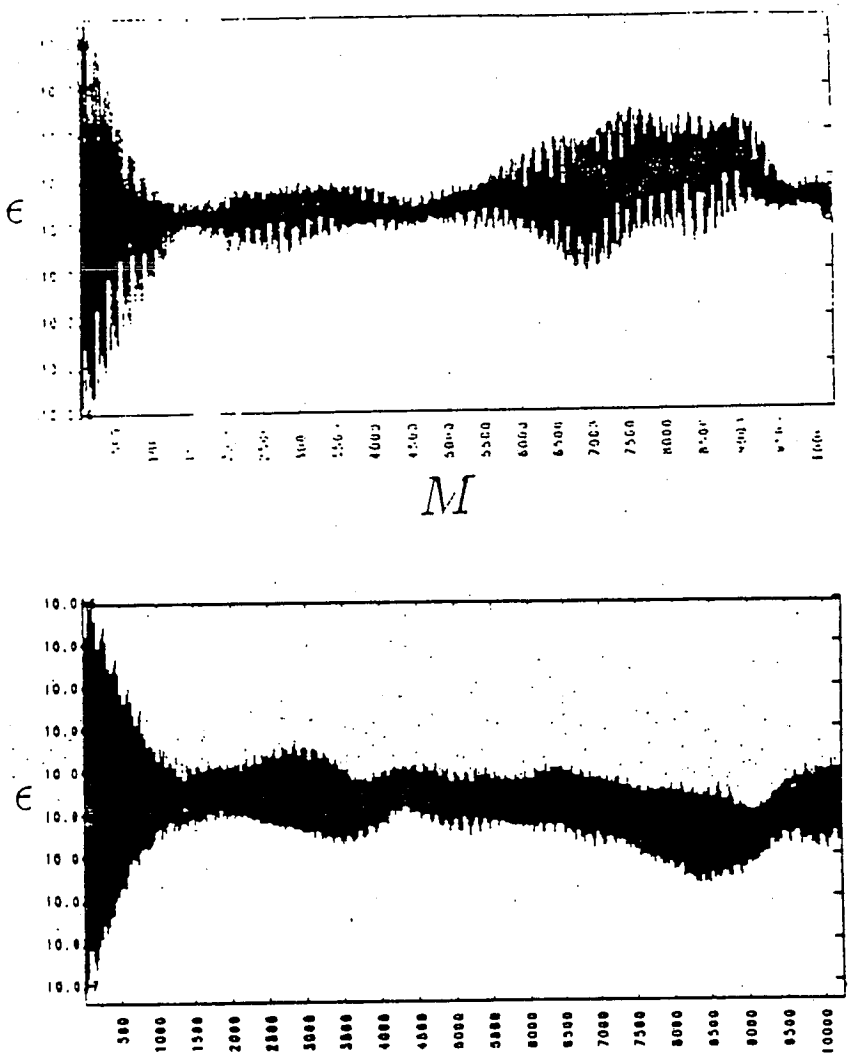

Figure 23: The emittance ϵ of both beams for 10240 rotations. One beam is at the top and the other beam is at the bottom of the figure

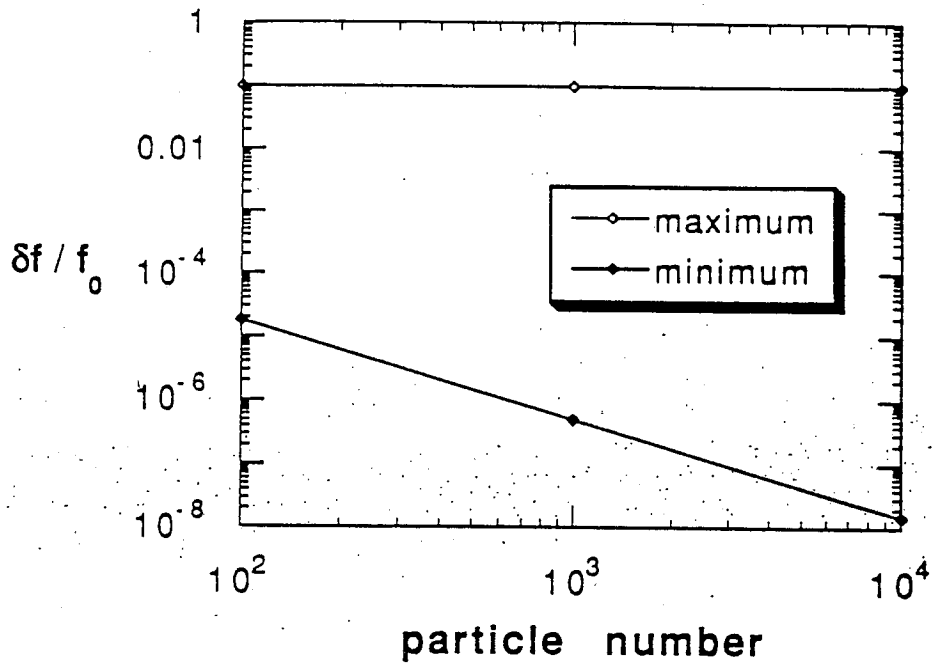

Figure 24: The minimum and maximum perturbation values $\delta f/f_0$ for $M =$ 10240 rotations, $\nu_0 = 0.285$, and $\Delta\nu_0 = 2.1 \times 10^{-3}$

minimal. By normalizing the code to a plasma with density lower than the beam, where ω_0 is the normalization plasma frequency and ω_b is the beam plasma frequency, only 4 simulation time steps are needed to cover the interaction region. Thus, $\omega_0 \Delta t = 0.25$ where Δt is the simulation time step size.

Figure 25 shows the distribution of 10^3 particles in $(x/\sigma_x, p_x/\sigma_p)$ phase space for one beam after 10^5 rotations. After 10^5 rotations the particles are no longer uniformly distributed in $(x/\sigma_x, p_x/\sigma_p)$ space. Some clumping of particles has occurred and small regions contain no particles. The clumping is not significant enough that the constant phase space density assumption is still a good approximation. A profile in x of a Gaussian distribution of particles in Fig. 26 is shown. Figure 27 shows the perturbations from the δf code to the Gaussian profile after 10^5 rotations. The center of the beam is at $x = 64\Delta$. The maximum perturbations are only 0.1% of the maximum in the Gaussian profile. Thus, the δf code is still a valid approximation. Notice that the perturbed distribution makes sense physically. There is a depletion of particles from the center of the beam and an increase in particles at about $\pm 2\sigma_x$. The beam is expanding slightly.

Results from the least-squares-fit method for one beam are shown in Fig. 28. The fit is done for small amplitude particles $x < 0.1\sigma_x$ at the top of the figure and for the entire beam for the bottom of the figure. The tune shift $\Delta\nu$ oscillates around the unperturbed values of $\Delta\nu_0 = 2.1 \times 10^{-3}$ for small amplitude particles and $\Delta\nu_0 \approx 1.52 \times 10^{-3}$ for all the particles. The discrepancy is due to the drop-off of $\Delta\nu$ at large values of x. The amplitude of the variation in $\Delta\nu$ for small amplitude particles is approximately $\pm 3\%$ of $\Delta\nu_0$ throughout the run. The tune shift obtained from all particles increases in amplitude with the number of rotations until approximately 15000 rotations and then remains somewhat constant until the end of the run. The maximum variation of $\Delta\nu$ is approximately $\pm 4\%$. The oscillations in $\Delta\nu$ indicate expansion and contraction of the beam which is kicking the particles. Notice that the beam which is kicking the particles is expanding and contracting differently at different

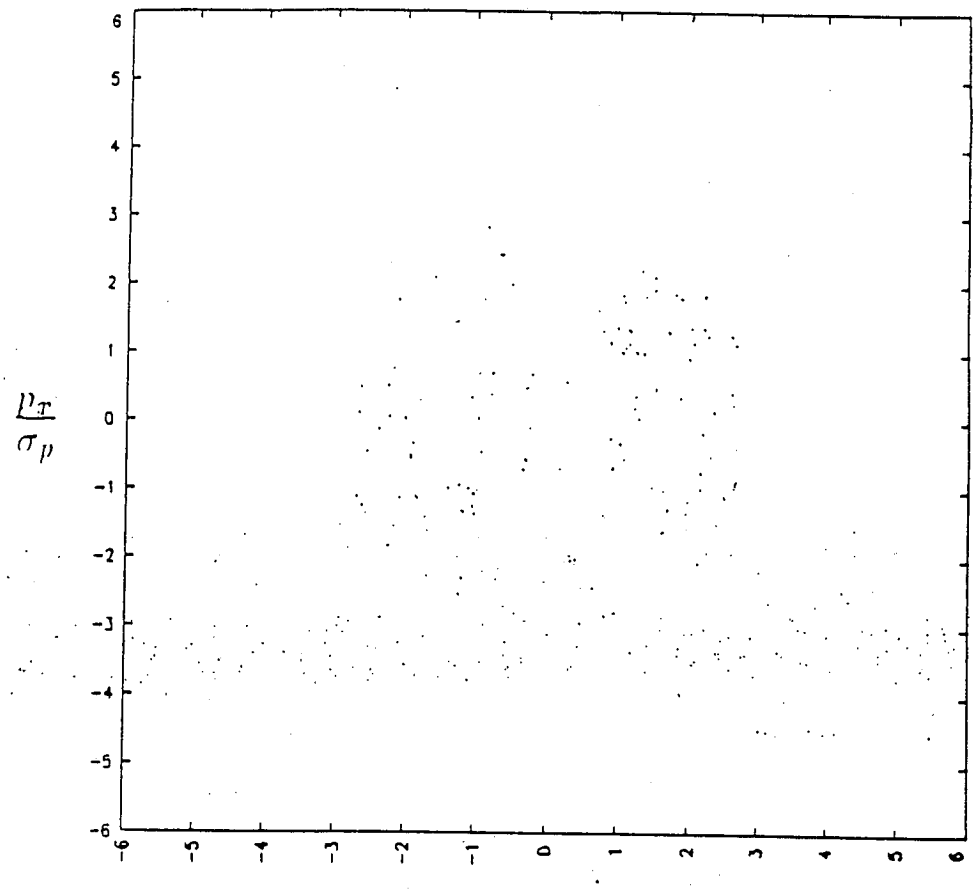

Figure 25: Distribution of 10^3 simulation particles in $(x/\sigma_x, p_x/\sigma_p)$ space after 10^5 rotations with $\nu_0 = 0.285$ and $\Delta\nu_0 = 2.1 \times 10^{-3}$.

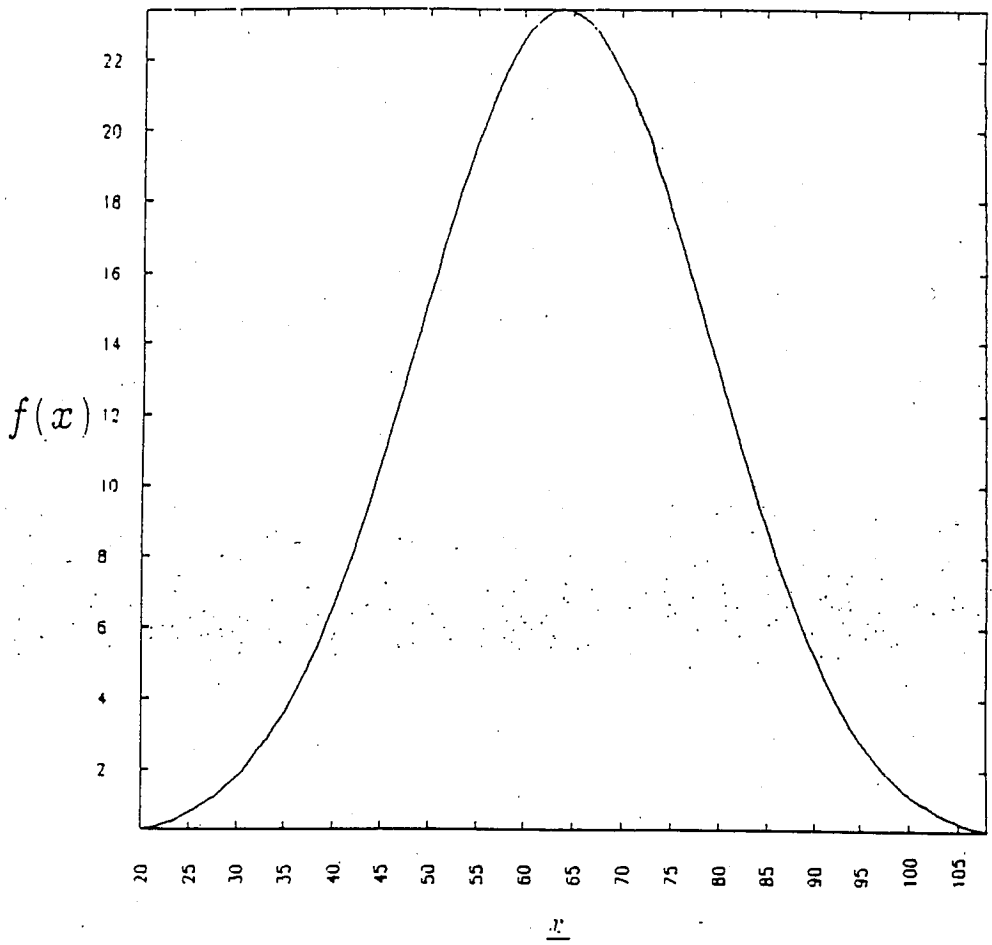

Figure 26: Gaussian steady state distribution

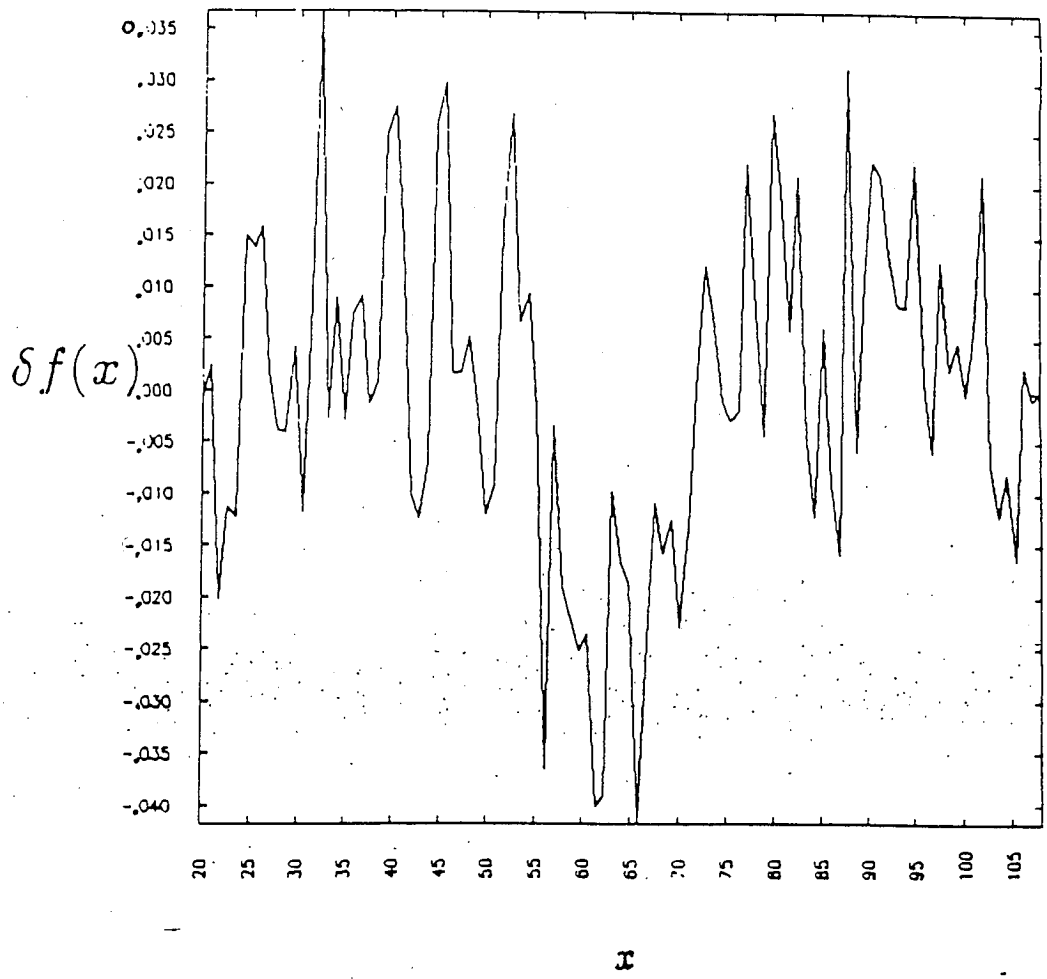

Figure 27: Distribution of 10^3 δf simulation particles including the particle weights in x after 10^5 rotations with $\nu_0 = 0.285$ and $\Delta\nu_0 = 2.1 \times 10^{-3}$.

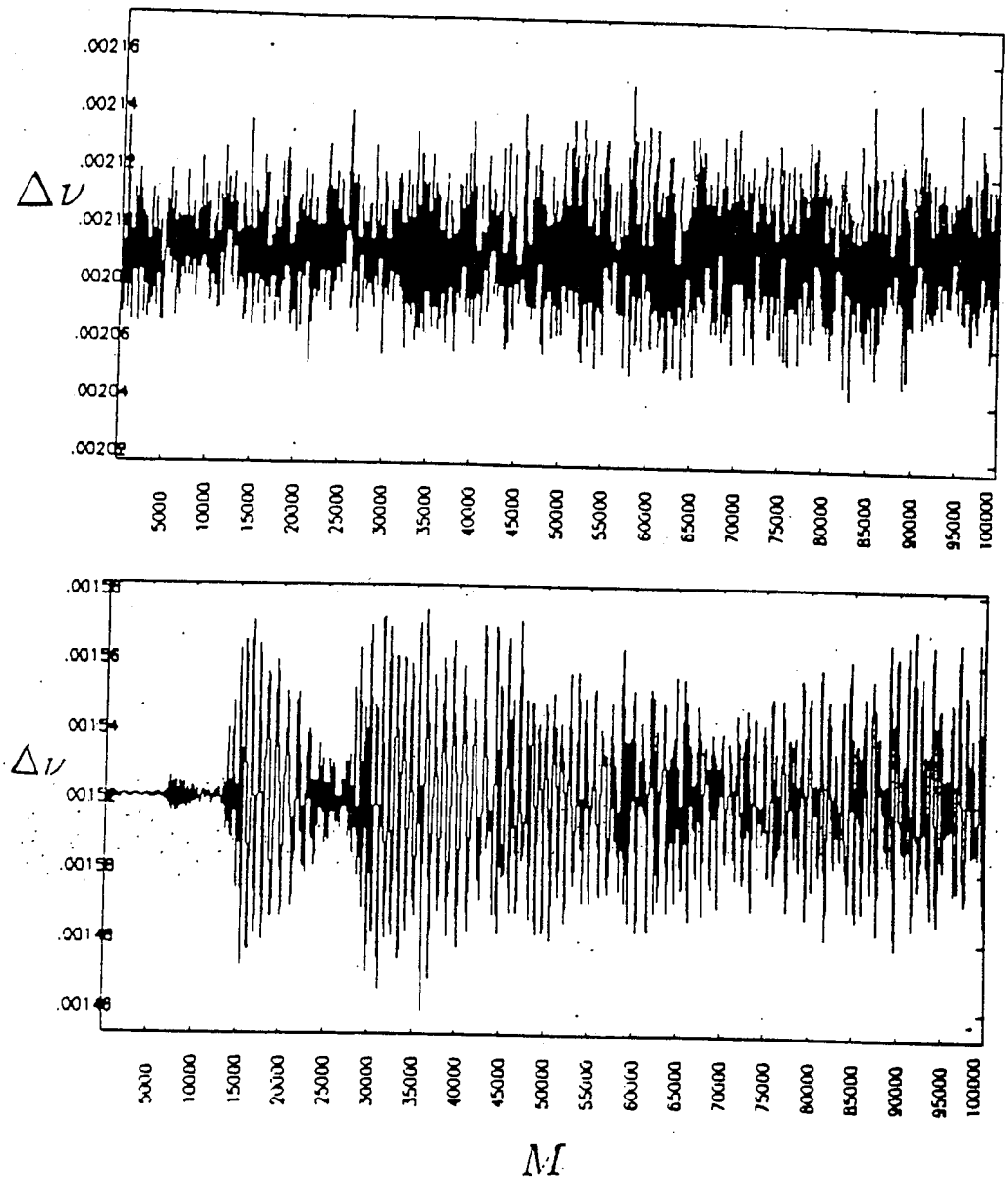

Figure 28: Tune shift $\Delta\nu$ measured from a least squares fit to small amplitude particles $x < 0.1\sigma_x$ (top) and all particles (bottom) for $M = 10240$ rotations

particle positions. The small amplitude portion of the beam is constant oscillation amplitude while the entire beam is increasing oscillation amplitude for the first 15000 rotations.

The other method by which the tune shift $\Delta\nu$ is measured is by getting power spectra of the x positions of sample particles which are sampled once every complete rotation. Figure 29 shows the shift in the power spectral peak from 100 particle positions in phase space. The tune shift $\Delta\nu$ is measured from the shift in the power spectral peak from the unperturbed tune ν_0. Notice that $\Delta\nu$ decreases with increasing r/σ of the sample particle, where $r/\sigma = \sqrt{x^2/\sigma_x^2 + p_x^2/\sigma_p^2}$.

Moments of one beam and their associated power spectra $S(\nu)$ are shown in Figs. 30, 31, 32, and 33. At the top of Fig. 30 the oscillation of the average beam center $\langle x\rangle$ is apparent. The beam oscillates with a maximum beam amplitude of $\delta x/\sigma_x \approx \pm 1.6 \times 10^{-4}$. The average $\langle x\rangle$ and $\langle (x - \langle x\rangle)^3\rangle$ [Fig. 32], the odd moments, are both increasing in oscillation amplitude with rotation number. At the top of Fig. 31 the oscillation of the beam width can be seen. The beam is oscillating about the initial beam width σ_x^2 with a maximum amplitude of approximately $\pm 0.003\sigma_x^2$. Oscillations are also apparent for $\langle (x - \langle x\rangle)^4\rangle$ at the top of Fig. 33. These oscillations are induced spontaneously. This is in spite of the initial lack of offset and initial lack of noise due to finite number of particles. The latter is due to our adoption of the δf algorithm. The particle weights w_i were taken to be zero at $t = 0$.

The bottoms of Figs. 30, 31, 32, and 33 show the moments and their associated power spectra. The power spectra of the average of x, $\langle x\rangle$, is shown at the bottom of Fig. 30. There are peaks in $S(\nu)$ in descending power at $\nu \approx \pm\nu'$ and $\pm(5\nu' - 1)$ where $\nu' = \nu_0 - \Delta\nu_0$. These peaks correspond to harmonics of the betatron motion. In Fig. 31 the peaks in the power spectra $S(\nu)$ at $\nu \approx \pm(1 - 2(\nu_0 - \Delta\nu_0))$ also correspond to the betatron motion of the beam. The peak near $\nu \approx 0$ corresponds to low frequency oscillations with periods longer than 10^4 rotations. Figure 32 shows $S(\nu)$ for $\langle (x - \langle x\rangle)^3\rangle$. The peaks in $S(\nu)$ in descending power are at $\pm(5\nu' - 1)$, $\nu \approx \pm\nu'$, $\pm(1 - 3\nu')$, and $\pm(2 - 7\nu')$ where $\nu' = \nu_0 - \Delta\nu_0$. Similarly

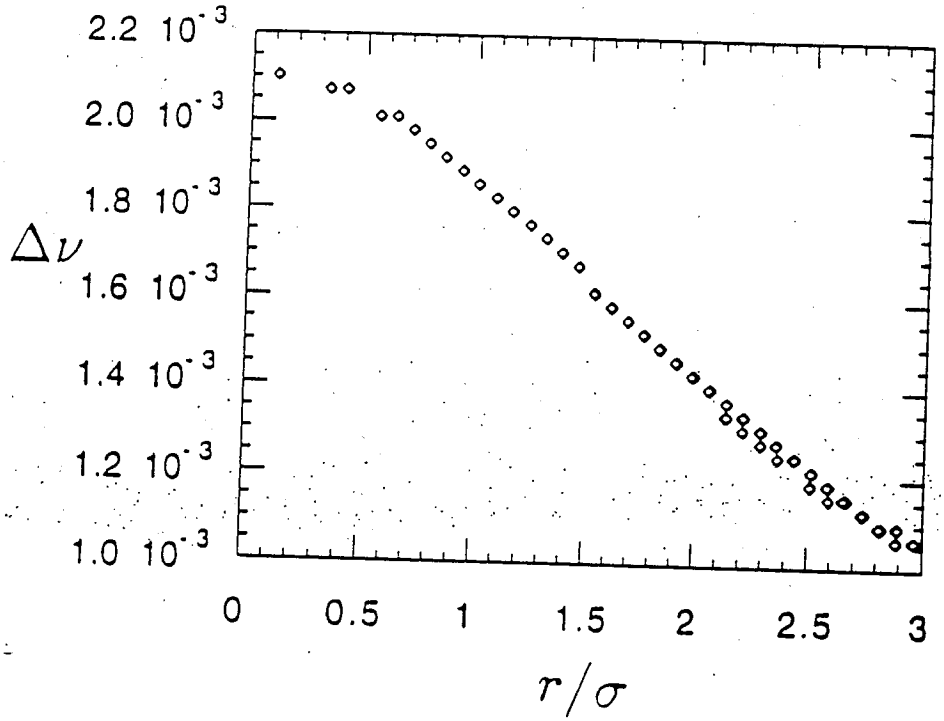

Figure 29: The tune shift $\Delta\nu$ measured from the shift in the power spectral peaks of the x positions of 100 sample particles after $M = 10^5$ rotations.

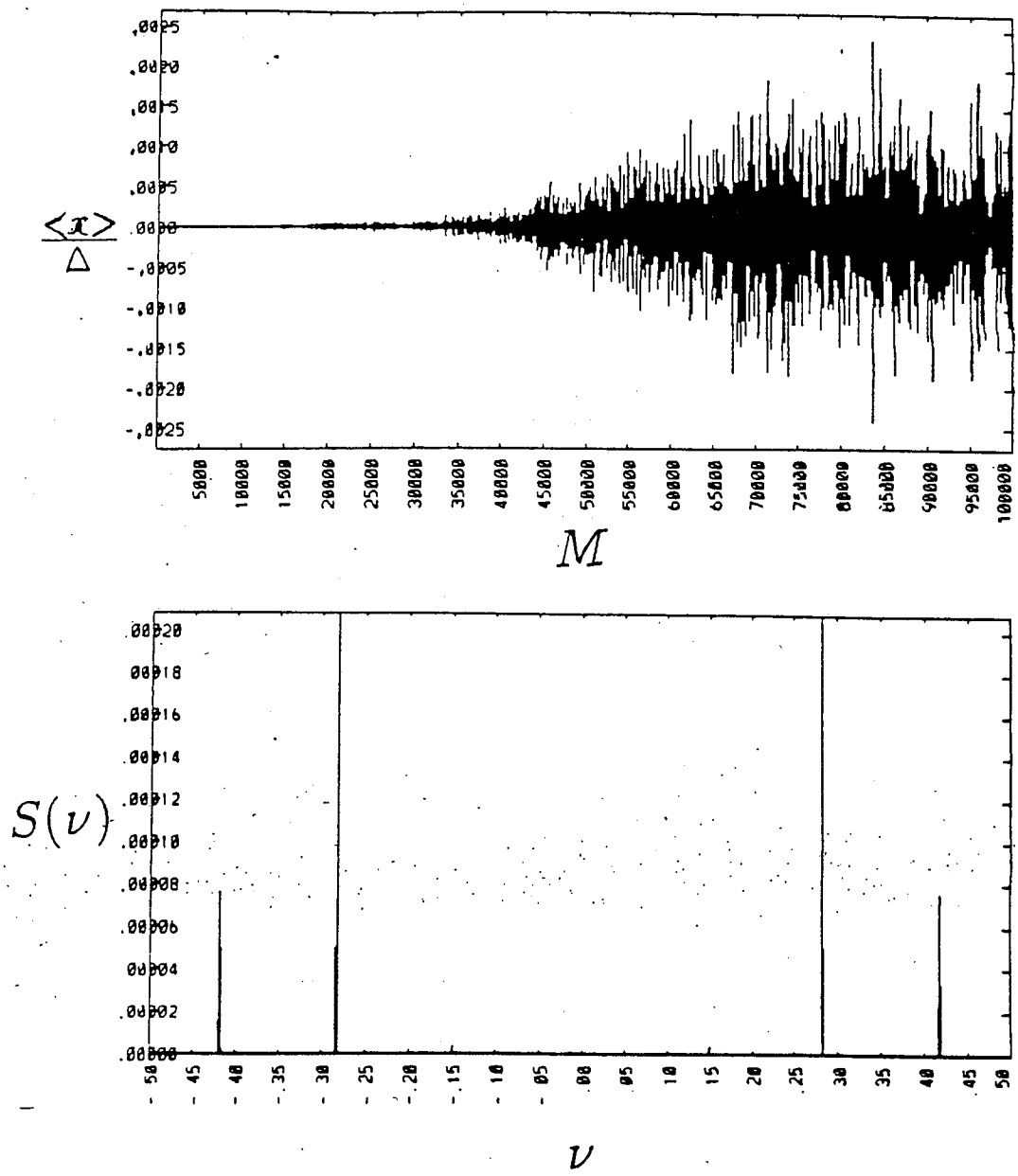

Figure 30: Beam moment $\langle x \rangle$ and $S(\nu)$ for $M = 10^5$ rotations at the top and bottom of the figure respectively.

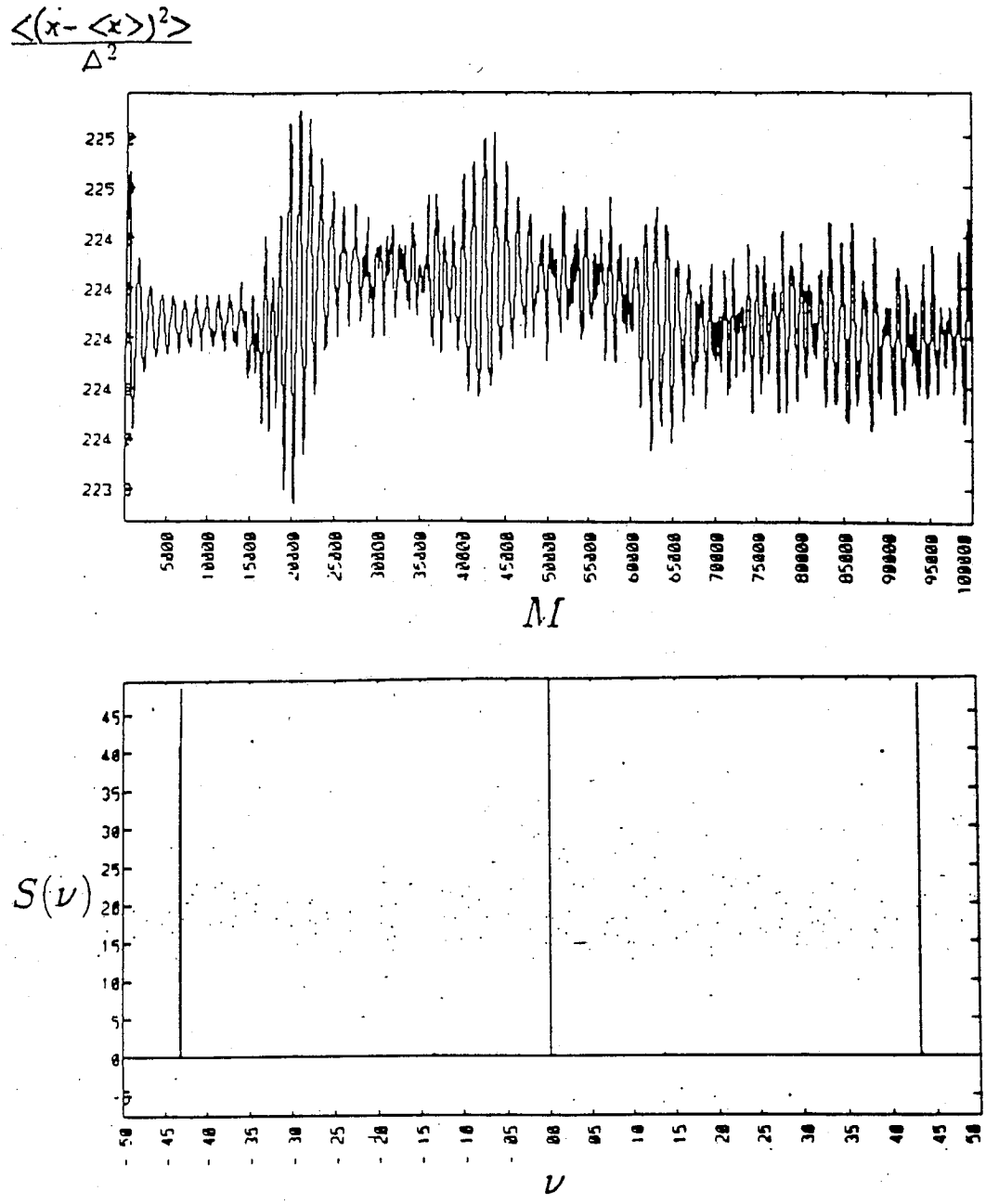

Figure 31: Beam moment $\langle (x - \langle x \rangle)^2 \rangle$ and $S(\nu)$ for $M = 10^5$ rotations at the top and bottom of the figure respectively.

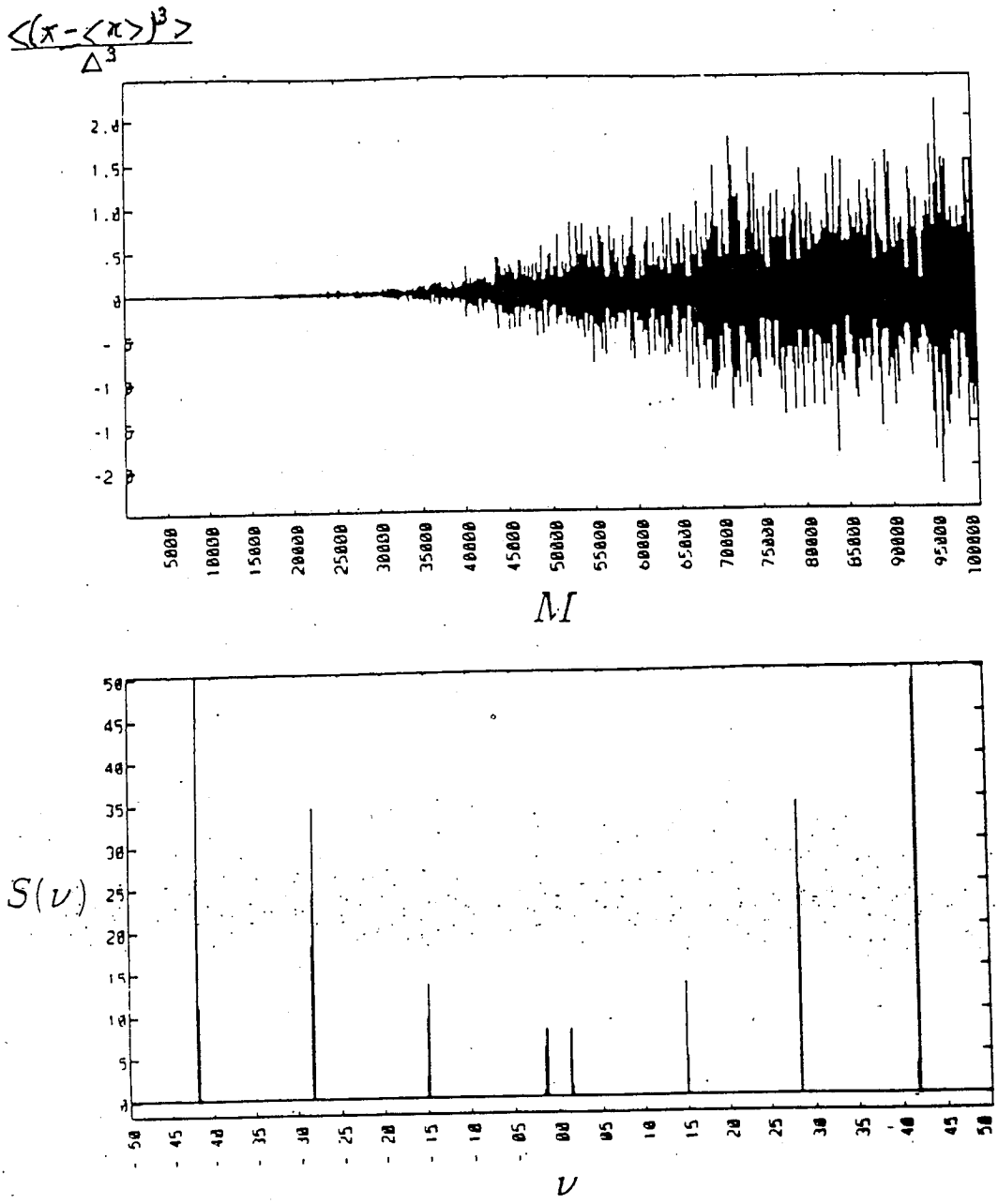

Figure 32: Beam moment $\langle (x - \langle x \rangle)^3 \rangle$ and $S(\nu)$ for $M = 10^5$ rotations at the top and bottom of the figure respectively.

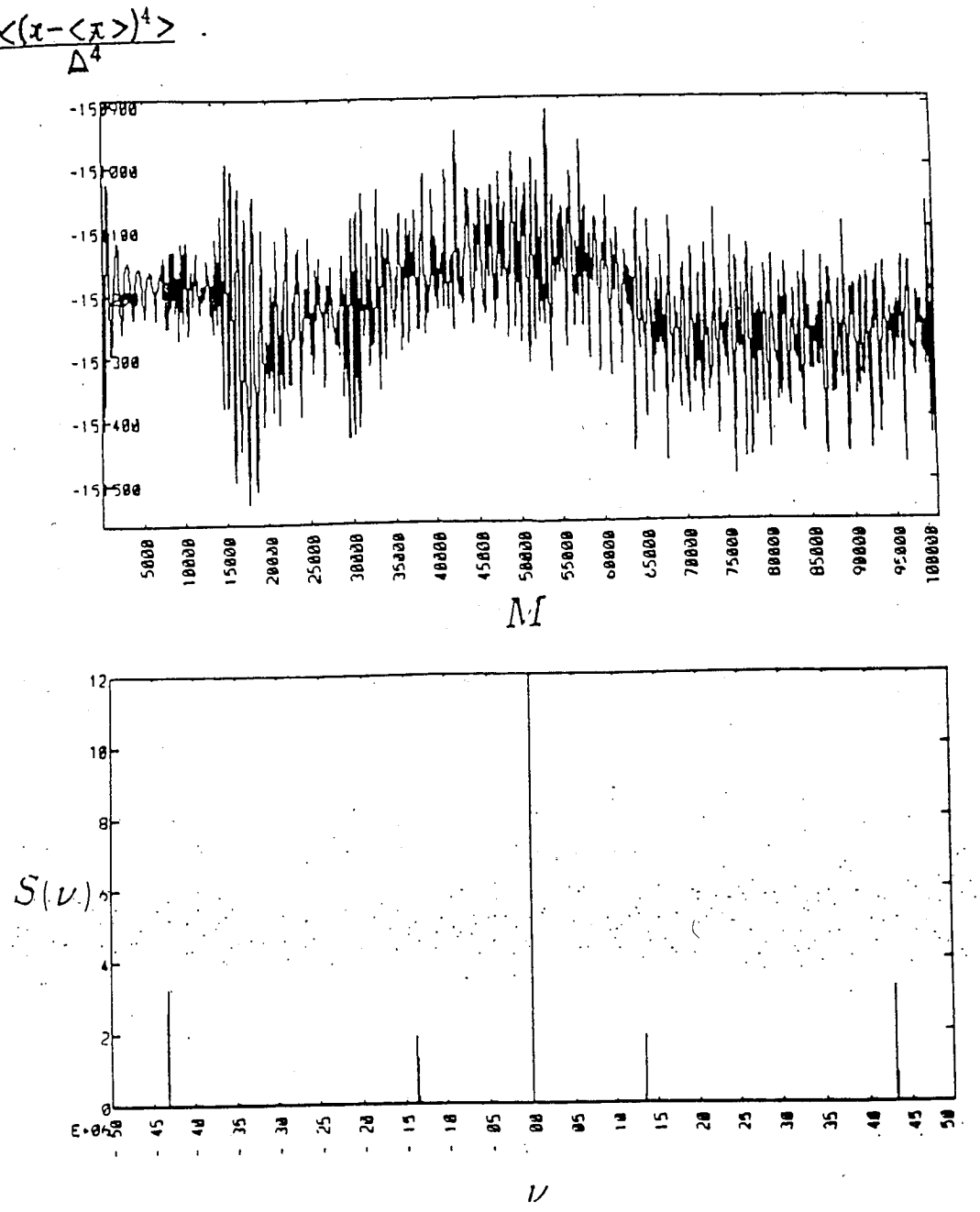

Figure 33: Beam moment $\langle (x - \langle x \rangle)^4 \rangle$ and $S(\nu)$ for $M = 10^5$ rotations at the top and bottom of the figure respectively.

in Fig. 33 $S(\nu)$ for $\langle (x - \langle x \rangle)^4 \rangle$ has peaks in descending power at $\pm(1 - 2\nu')$ and $\pm(1 - 4\nu')$ where $\nu' = \nu_0 - \Delta\nu_0$. As in the case with $\langle (x - \langle x \rangle)^2 \rangle$, there is a low frequency peak with oscillations having time scales longer than 10^4 rotations. It appears from these results that the even beam moments contain more power in the low frequency components of $S(\nu)$ than the odd beam moments.

The emittance ϵ of each beam for 10^5 rotations is shown in Fig. 34. The emittance for one beam is at the top of the figure and the other is at the bottom. The beams show similar behavior through the 10^5 rotations. They expand and contract in phase space simultaneously. The maximum expansion is about $\delta\epsilon/\epsilon_0 \approx 2 \times 10^{-3}$.

$\nu_0 - \Delta\nu_0$ stability

In this section we examine the variation of beam stability with tune ν_0 and tune shift $\Delta\nu_0$. The strong-strong PIC simulation code is employed exclusively here. Although the δf code is quieter, it is not well suited for studying beam blowup phenomena which distort the original distribution by a significant amount.

Figure 35 shows a stability diagram of $\Delta\nu_0$ versus ν_0. The dotted lines are obtained from a linear theory developed by Chao and Ruth.[5] The lines demarcate regions of linear stability and instability for equal charge beams. The stable regions are those regions contained by the dotted lines. The lines plotted are for up to 8 beam modes. As is the general case with any linear theory the theory can predict the initial growth rates of the instability, but not the saturation levels. The points in Fig. 35 represent strong-strong simulation code results, in which the unperturbed $\Delta\nu_0$ and ν_0 are varied. The unperturbed tune shift $\Delta\nu_0$ is scanned between the SSC reference value of 2.1×10^{-3} and a maximum value of 0.04. In each of the simulations 10^4 simulation particles are used. The codes are run for 10^4 rotations with the exception of one run which is run for 3×10^4 rotations. All the runs are initialized with variable charge and uniform distribution. All other parameters are the same as previous

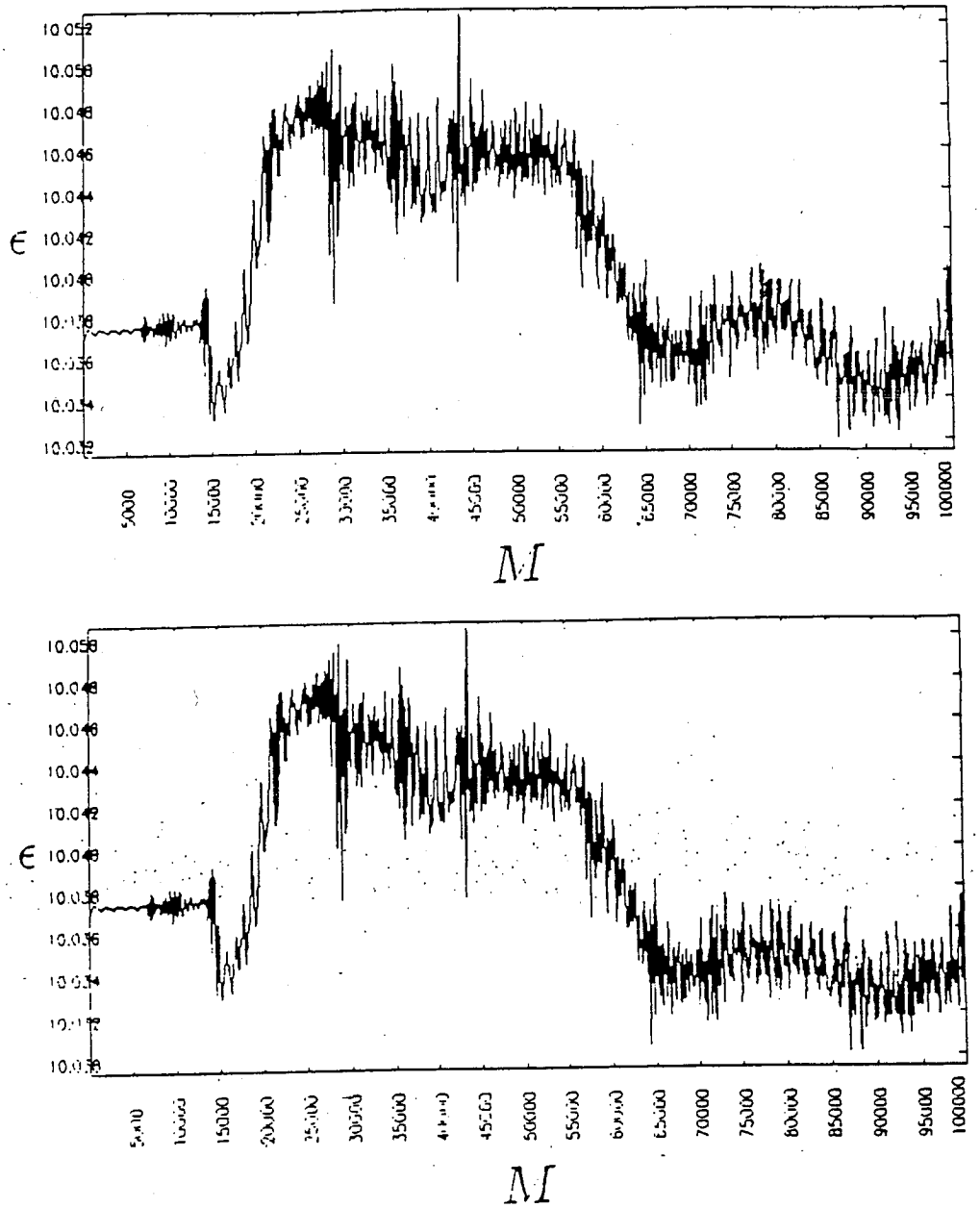

Figure 34: The emittance ϵ of both beams for 10^5 rotations. One beam is at the top and the other beam is at the bottom of the figure

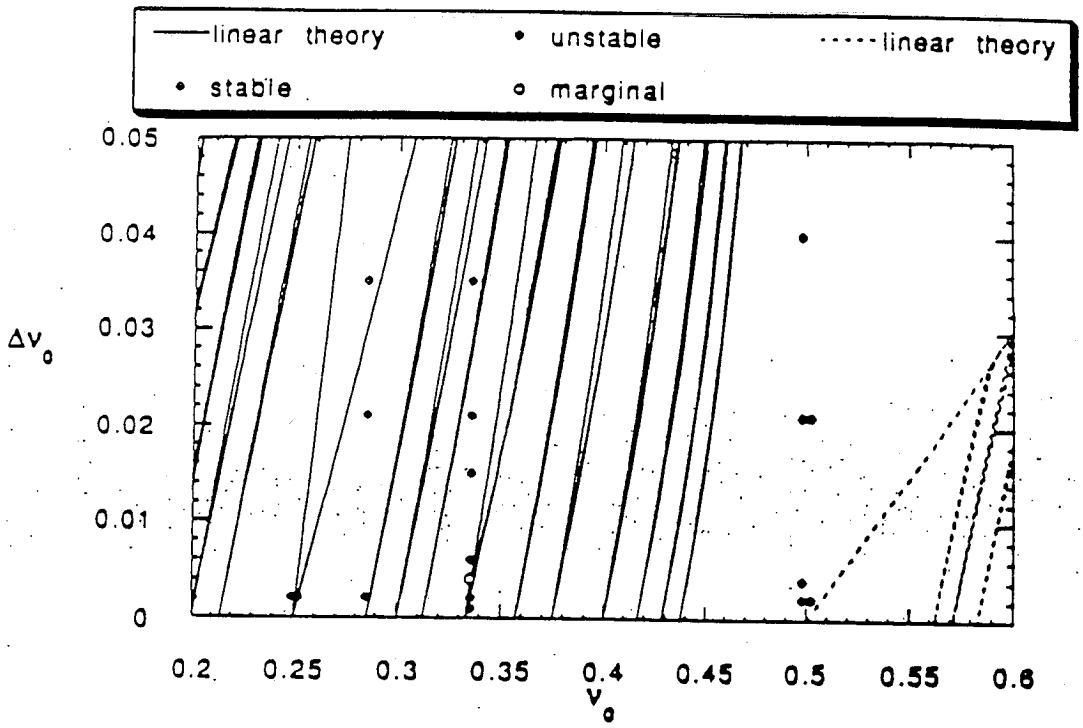

Figure 35: $\nu_0 - \Delta\nu_0$ Stability Diagram

strong-strong simulation runs. Beam stability for various values of $\Delta\nu_0$ and ν_0 is determined from emittance growth. If the emittance of the beams ϵ increases by 50%, then the run is designated unstable. The marginally stable case noted in Fig. 35 is determined from the emittance growth after 30000 rotations.

The results from the simulations show good agreement with the linear theory of Chao and Ruth.[5] The beams are unstable in regions of instability and are stable in regions of stability.

We examine in more detail the cases where $\Delta\nu_0$ is small. In this case similarly charged beams with values of the unperturbed tune ν_0 just above a resonance are kicked towards the resonance by the beam-beam interaction. In this case the beams are expected to be unstable. For beams with values of ν_0 just below a resonance the beam-beam kick is away from the resonance and the beams are expected to be stable. Beam blowup due to strong resonance is observed just above $\nu_0 = 1/2$ and $\nu_0 = 1/4$ for values of $\Delta\nu_0 = 2.1 \times 10^{-3}$. Figures 36 and 37 show the phase space distribution of the simulation particles. In Fig. 36 phase space plots show simulation results around the $\nu_0 = 1/2$ resonance. At the top of Fig. 36, where $\nu_0 = 1/2 + \Delta\nu_0$ the beam blows up. At the bottom of Fig. 36, where $\nu_0 = 1/2 - \Delta\nu_0$, it is seen that mode 2 dominates the shape of the beam in phase space (football shape). In Fig. 36 phase space plots show simulation results around the $\nu_0 = 1/4$ resonance. At the top of Fig. 36, where $\nu_0 = 1/4 + \Delta\nu_0$, the beam particles are clumping and the emittance is observed to increase by more than 50%. At the bottom of Fig. 36, where $\nu_0 = 1/4 - \Delta\nu_0$, it is mode 4 which dominates (square shape). The beams in the case of $\nu_0 = 1/2 + \Delta\nu_0$ blow up very quickly. It only takes a few hundred rotations. The beams blow up more slowly for $\nu_0 = 1/4 + \Delta\nu_0$. This behavior is expected. Higher order resonances have lower growth rates of instability. The beams are stable just below $\nu_0 = 1/2$ and $\nu_0 = 1/4$ for small values of $\Delta\nu_0$.

A point is scanned just above $\nu_0 = 1/3$ with $\nu = \nu_0 + \Delta\nu_0$ where $\Delta\nu_0 = 4 \times 10^{-3}$. In

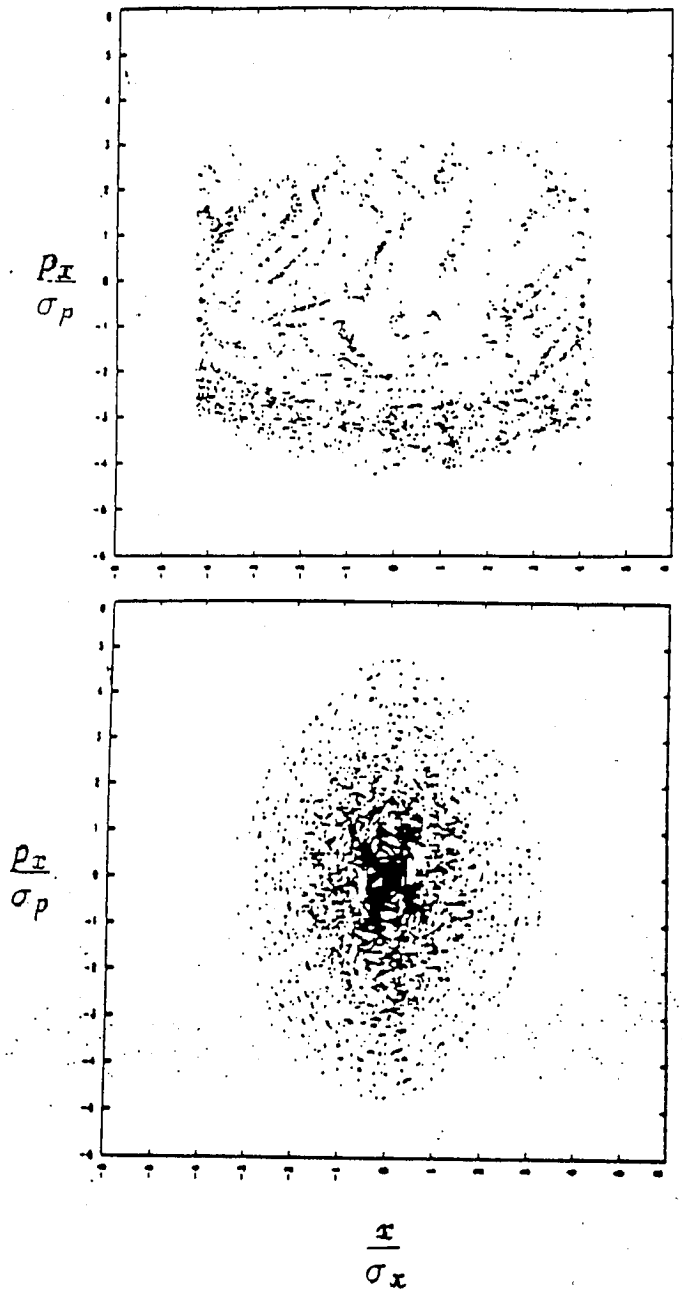

Figure 36: $(x/\beta^*, x')$ distribution of particles for $\nu_0 = 1/2 + \Delta\nu_0$ (top) and $\nu_0 = 1/2 - \Delta\nu_0$ (bottom) where $\Delta\nu_0 = 2.1 \times 10^{-3}$

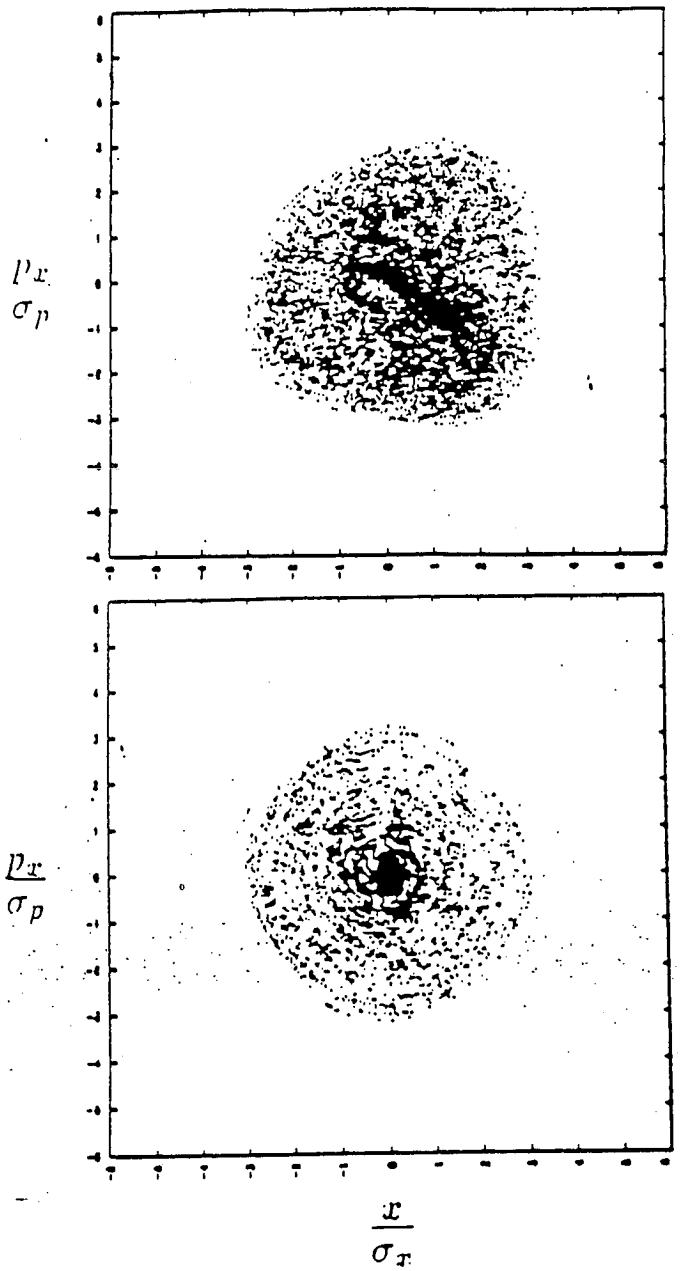

Figure 37: $(x/\beta^*, x')$ distribution of particles for $\nu_0 = 1/4 + \Delta\nu_0$ (top) and $\nu_0 = 1/4 - \Delta\nu_0$ (bottom) where $\Delta\nu_0 = 2.1 \times 10^{-3}$

this case the emittance ϵ is slowly growing [Fig. 38]. The beam emittance ϵ keeps growing until approximately 24000 rotations, after which it appears to saturate until the end of the run at 30000 rotations. The phase space distribution of one beam is shown in Fig. 39. It can be seen that mode 6 is beginning to slowly dominate the distribution. Since two (i.e. an even number of) beams are colliding, mode 2/6 is expected to dominate for $\nu_0 = 1/3 + \Delta\nu_0$. Since this is a high order mode, the slow growth rate is expected.

Particle diffusion

In this section we examine particle diffusion brought about by the beam-beam interaction. The diffusion is measured from the tracking code, strong-strong code, and the δf code. We compare the diffusion coefficients measured for each of these runs. Of the three codes the δf code gives the best representation. It is quieter than the PIC code and allows degrees of freedom of evolution from the initial distribution that are not permitted in the tracking code. We use the two methods described in Sec. 2 to measure particle diffusion.

Tracking code results

We first examine particle diffusion for particles tracked using the $1 - D$ tracking code described in Sec. 2.

Reference parameters described in Sec. 3 for the SSC are used: The tune $\nu_0 = 0.285$ and the tune shift $\Delta\nu_0 = 2.1 \times 10^{-3}$. The initial particle positions are shown in Fig. 41.

Diffusive motion of the sample particles can be obtained from diffusion coefficients, df1 and df2, calculated after 10240 rotations are shown in Fig. 41 where:

$$\frac{r}{\sigma} = \sqrt{\frac{x^2}{\sigma_x} + \frac{p_x^2}{\sigma_p}} \tag{122}$$

is the distance in phase space from the center of the beam. The D_x means that df1 and df2 are calculated for diffusion in position $|x|$ from Eq. (115). The diffusion is normalized to

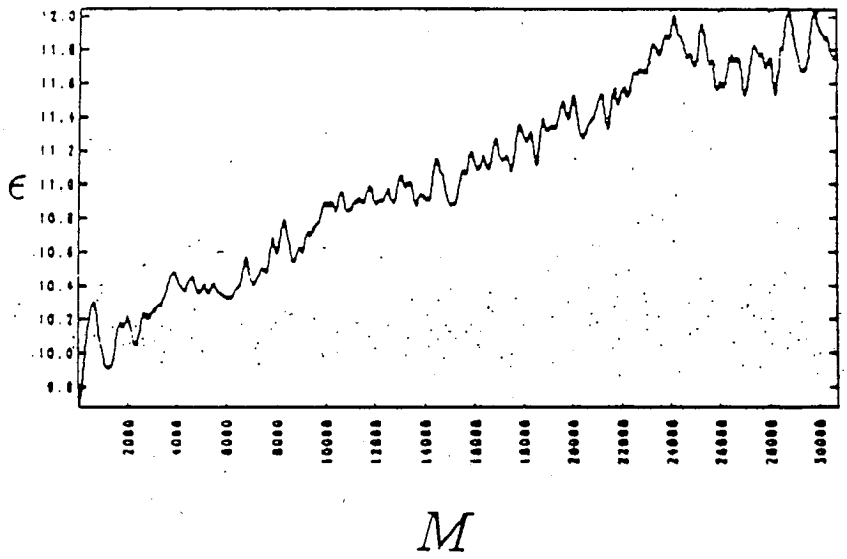

Figure 38: Emittance as a function of rotations for ν_0 just above 1/3

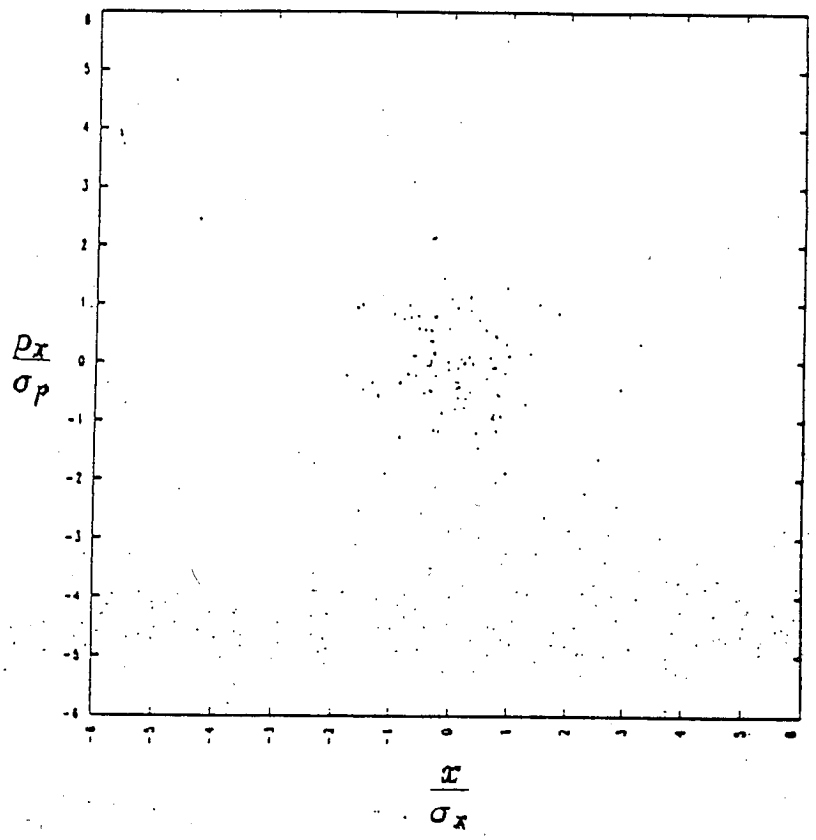

Figure 39: $(x/\beta^*, x')$ distribution of particles for $\nu_0 = 1/3 + \Delta\nu_0$ where $\Delta\nu_0 = 2.1 \times 10^{-3}$

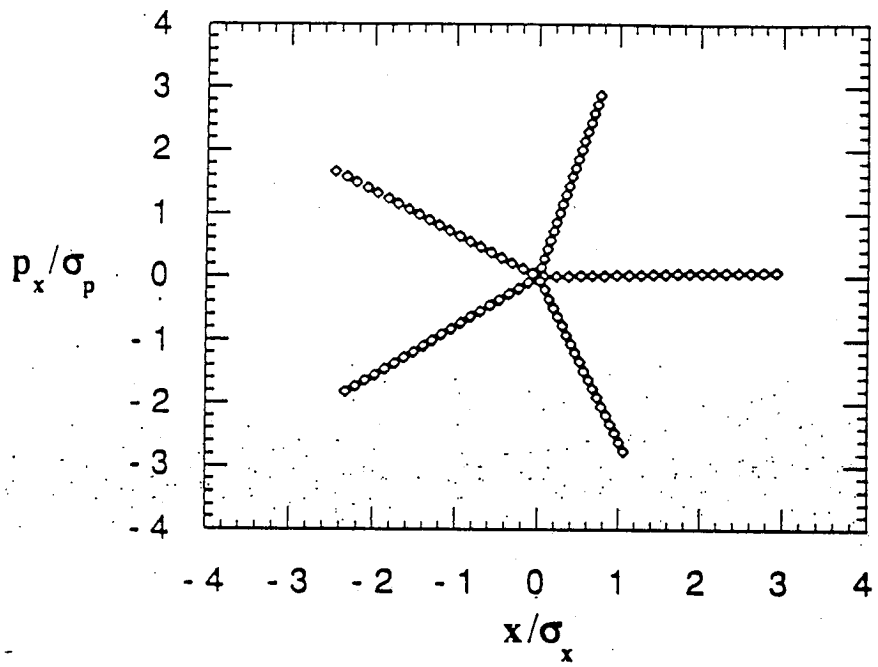

Figure 40: Initial particle positions for 100 tracking code particles in $(x/\sigma_x, p_x/p)$ phase space.

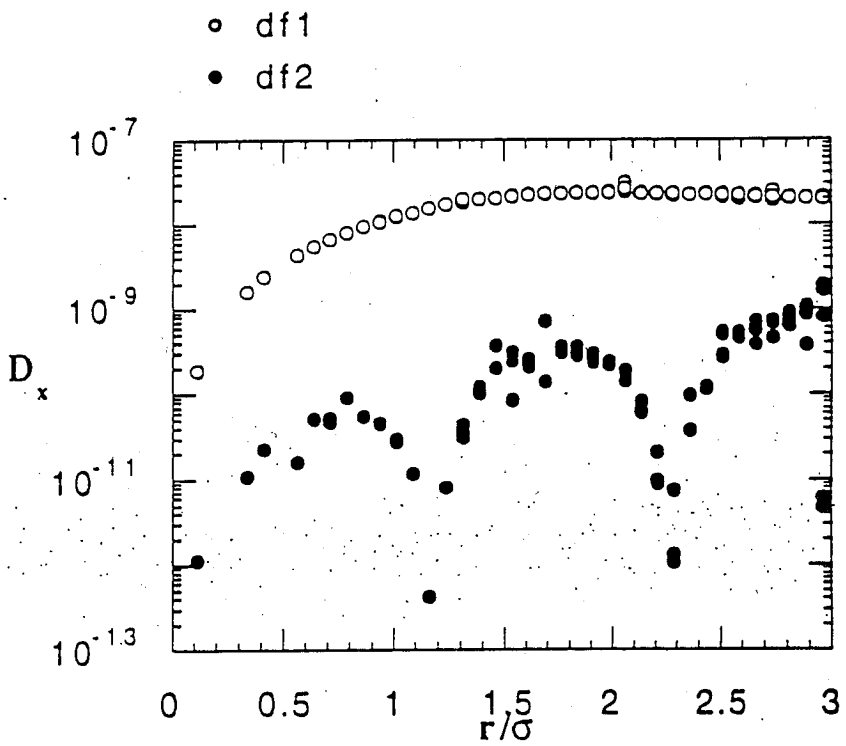

Figure 41: D_x from the tracking code with $\Delta\nu_0 = 2.1 \times 10^{-3}$ and $\nu = 0.285$ for $M = 10240$ rotations. df1 and df2 have time scales of $\Delta N_1 = 102$ and $\Delta N_2 = 1024$ rotations respectively.

σ_x^2/N_r where N_r is the number of rotations. In Fig. 41 it is apparent from the fact df1 $\gg$ df2 that the motion is largely oscillatory in phase space. The coefficients calculated over two time scales differ on average by about a factor of 100. This is expected for oscillatory motion where:

$$\frac{\text{df2}}{\text{df1}} \propto \left(\frac{\Delta N_1}{\Delta N_2}\right)^3$$
$$\propto \frac{1}{1000} \tag{123}$$

Figures 42 and 43 show the diffusion coefficients calculated for $M = 40960$ and $M = 10^5$ rotations, respectively. The average diffusion rate is decreasing with increasing rotations. The range of coefficients for 40960 rotations is between 10^{-9} and 10^{-14} and for 10^5 rotations between 10^{-10} and 10^{-15}. This drop with increasing rotation number is another indication that the particle motion is still oscillatory and not diffusive. If the particles are diffusive the diffusion coefficients would settle down to values independent of the time scale. There are some points between $r/\sigma = 1.5$ and $r/\sigma = 2$ which meet the criteria for diffusivity. That is, df1 $\approx$ df2. However, most of the coefficients differ by about a factor of 100.

So in tracking code simulations a majority of the particles exhibit oscillatory motion at different values of position x up to 10^5 rotations.

Strong-strong simulation results

In this section results from the strong-strong code on particle diffusion are presented. The effects of the particle initialization method are examined and the results are compared with the tracking code. Again reference parameters described in Sec. 3 for the SSC are used. So the tune $\nu_0 = 0.285$ and the tune shift $\Delta\nu_0 = 2.1 \times 10^{-3}$.

Results from the strong-strong code with variable charge per particle are shown in Fig. 44. Each beam in the simulation has 10^4 simulation particles with the initial distribution in (x, p_x) phase space shown in Fig. 4 and the resulting profile shown in Fig. 2.

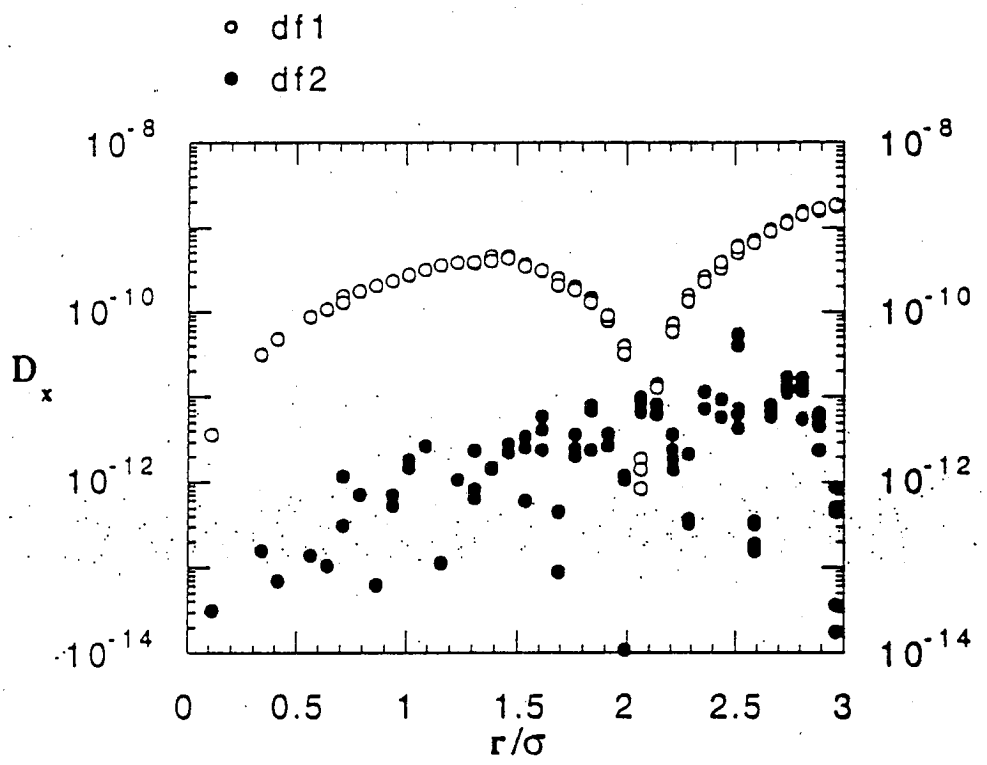

Figure 42: D_x from the tracking code with $\Delta\nu_0 = 2.1 \times 10^{-3}$ and $\nu = 0.285$ for $M = 40960$ rotations. df1 and df2 have time scales of $\Delta N_1 = 409$ and $\Delta N_2 = 4096$ rotations respectively.

The diffusion coefficients are calculated for 100 sample particles after 10240 rotations. The initial particle positions are the same as the tracking code shown in Fig. 40. As in the tracking code results in the previous section the diffusion coefficients, df1 and df2, are calculated at various $|x|$ in Eq. (115). The diffusion D_x is normalized to σ_x^2/N_r where N_r is the number of rotations. The diffusion coefficients differ substantially from those obtained from the tracking code [Fig. 41]. All the particles in this case show the diffusive nature. D_x is uniform across the beam radial position and is nearly an order of magnitude higher than the tracking code values. Some of this diffusiveness is from fluctuations due to the finite number of particles of the strong-strong code. This dependence is shown in Figs. 45 and 46. These figures show the diffusion coefficients, df1 and df2, for two different particles after 1000 rotations. One is for a sample particle at $r/\sigma = 0.1$ [Fig. 45] and the other is for sample particle at $r/\sigma = 0.9$ [Fig. 46]. In both figures the solid line and the dashed lines refer to the diffusion coefficients df1 and df2, respectively, calculated from a tracking code. Note that the tracking code values are independent of the number of particles, since the field is calculated from one Gaussian particle ("strong beam"). Both plots show a reduction in the diffusion coefficient for the strong-strong code calculated on the longer time scale (df2). It is more apparent for the particle at $r/\sigma = 0.1$ [Fig. 45]. The reduction goes as $1/\sqrt{N}$, where N is the number of particles. This $1/\sqrt{N}$ dependence shows that finite particle fluctuation noise,[3, 36] which goes as $1/\sqrt{N}$, is contributing to the diffusion of the sample particles.

In order to reduce the fluctuation noise, we use the nonuniform particle initialization method described in Sec. 2. The simulation particles are given equal charge and are nonuniformly distributed in (x, p_x) phase space [Fig. 6]. The resulting profile in x is shown in Fig. 7 for 10000 simulation particles. SSC reference parameters are used with $\nu_0 = 0.285$ and $\Delta\nu_0 = 2.1 \times 10^{-3}$. The nonuniform initialization of the simulation particles does make a difference in the finite particle fluctuation noise level. The reduced diffusion is evident in Fig. 47, where the variable charge and uniform charge diffusion coefficients are shown

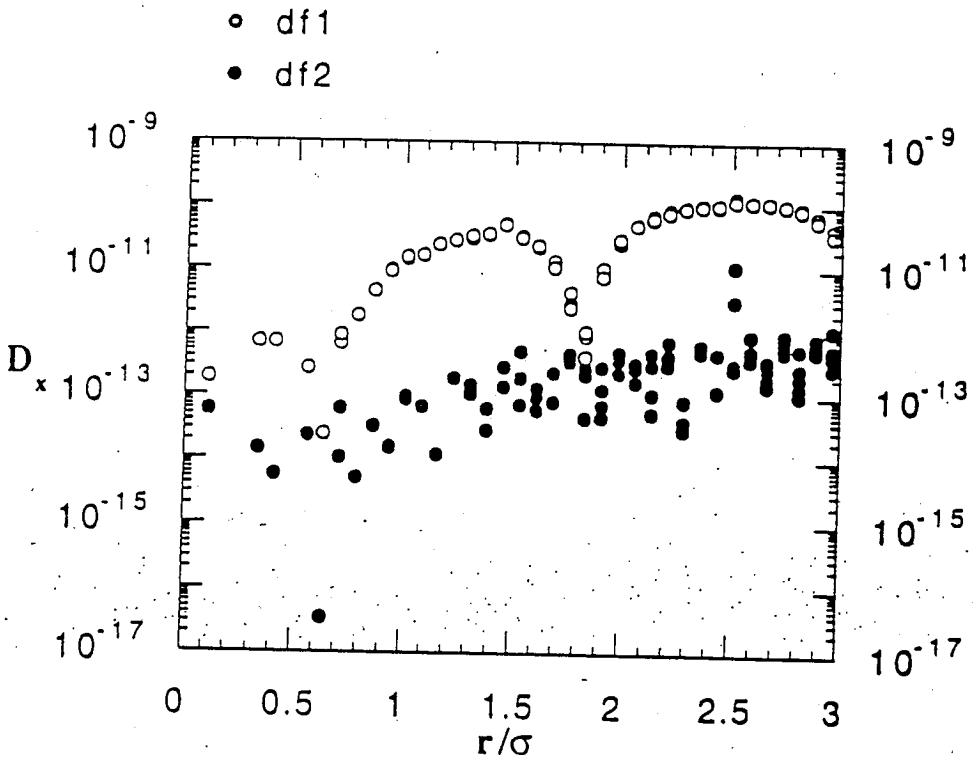

Figure 43: D_x from the tracking code of the beam with $\Delta\nu_0 = 2.1 \times 10^{-3}$ and $\nu = 0.285$ for $M = 10^5$ rotations. df1 and df2 have time scales of $\Delta N_1 = 1000$ and $\Delta N_2 = 10000$ rotations respectively.

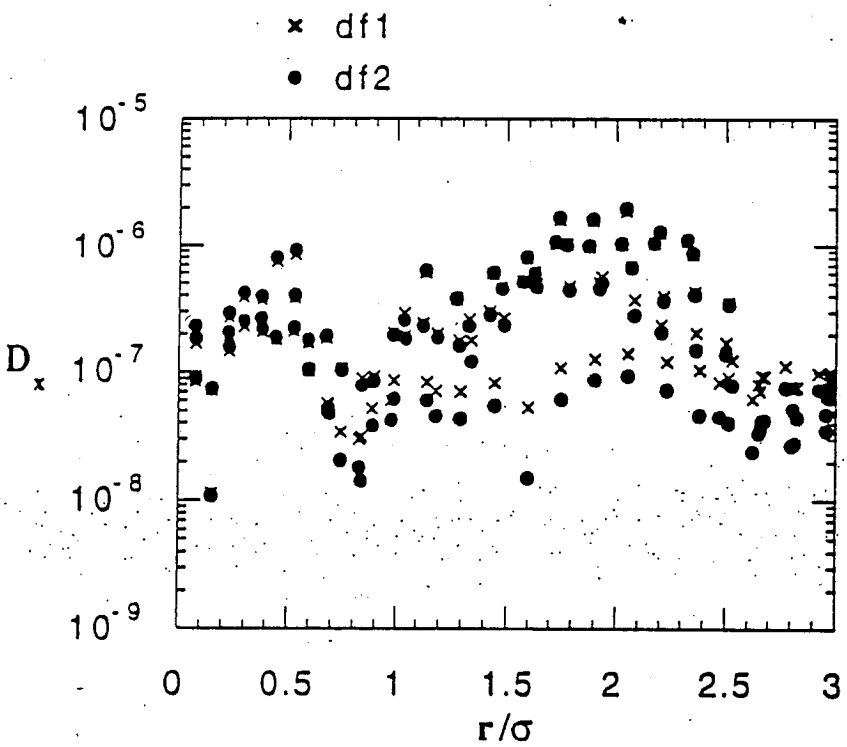

Figure 44: D_x from the strong-strong code with $\Delta\nu_0 = 2.1 \times 10^{-3}$ and $\nu = 0.285$ for $M = 10240$ rotations. df1 and df2 have time scales of $\Delta N_1 = 102$ and $\Delta N_2 = 1024$ rotations respectively.

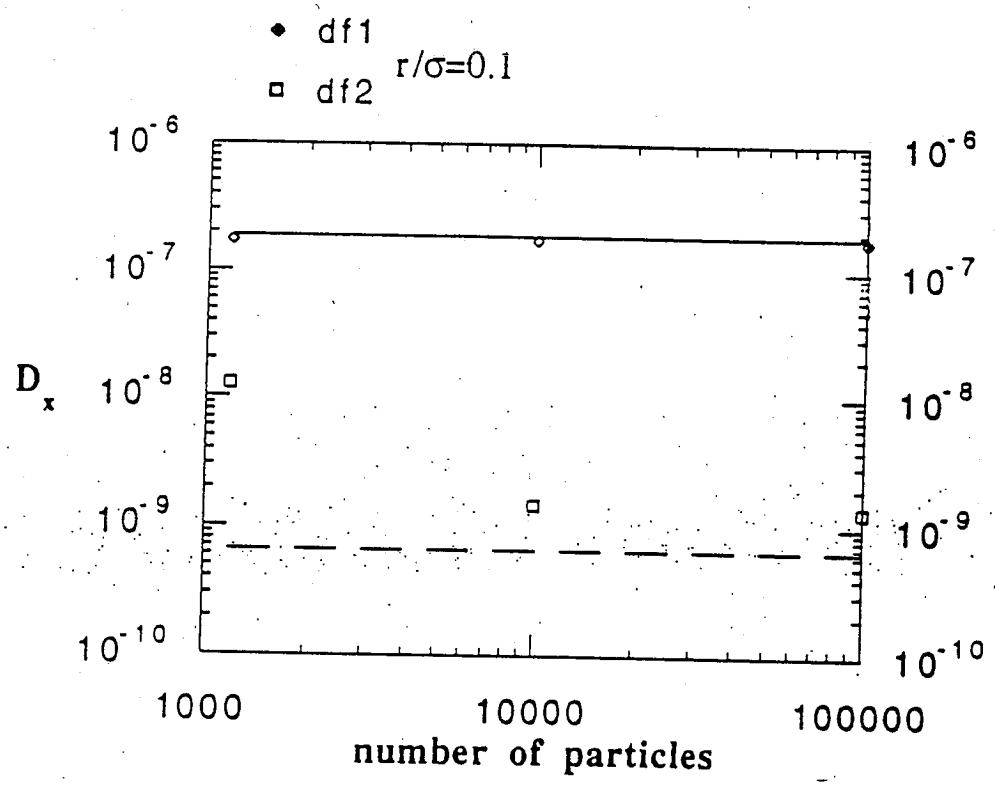

Figure 45: D_x versus particle number for a sample particle at $r/\sigma = 0.1$ for $M = 1000$ rotations. df1 and df2 have time scales of $\Delta N_1 = 10$ and $\Delta N_2 = 100$ rotations respectively.

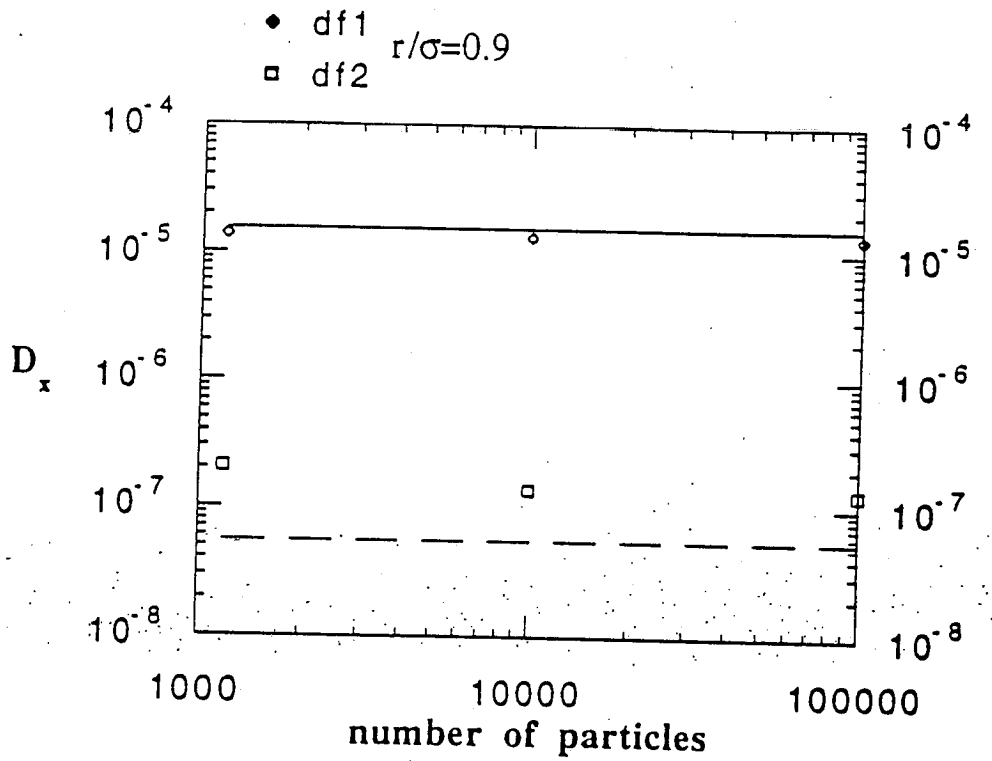

Figure 46: D_x versus particle number for a sample particle at $r/\sigma = 0.9$ for $M = 1000$ rotations. df1 and df2 have time scales of $\Delta N_1 = 10$ and $\Delta N_2 = 100$ rotations respectively.

for $M = 10240$ rotations. The uniform charge initialization is much quieter. It shows oscillatory particle motion for particles with $r/\sigma < 2$. The only particles which exhibit diffusive characteristics are those particles with $r/\sigma > 2$, that is, particles in the tails of the distribution. In comparison with the tracking code the sample particles from the uniform charge initialization show more diffusive behavior [Fig. 48]. The agreement is good between the tracking code and strong-strong code for the shorter time scale diffusion coefficient df1 for values of $r/\sigma < 2$. However, the longer time scale diffusion coefficient for the uniform particle initialization shows higher values for all values of r/σ, especially in the tail of the distribution.

It has been shown that finite particle fluctuation noise plays a role in the diffusion of particles in the strong-strong simulations. This noise can be somewhat offset by using quieter particle initialization schemes such as the smooth charge loading scheme. However, there are still significant differences from the tracking code. Although the strong-strong code should show differences from the tracking code because of the self consistent solution of the fields, it is difficult to determine whether the differences observed are due to particle fluctuation noise alone. In order to get a better grasp of the effects of this fluctuation noise, the noisy tracking code described in Sec. 2 is used. Figure 49 shows the results for 10240 rotations where noise added to the tracking code is of the form described in Sec. 2. The noise level δ is determined by:

$$\delta = \frac{1}{\sqrt{N(x)}} \tag{124}$$

where $N(x) = N \operatorname{erf}(x/\sqrt{2}\sigma_x)$ and N is the particle number. Notice that the small amplitude particles at $r/\sigma = 0.1$ are diffusive for the noisy tracking code and the PIC code. The larger amplitude particles at $r/\sigma = 0.9$ are both oscillatory. The PIC code is more diffusive than the noisy tracking code at $r/\sigma = 0.1$ and is less oscillatory than the noisy tracking code at $r/\sigma = 0.9$. These results indicate that some of the diffusion observed in the PIC code

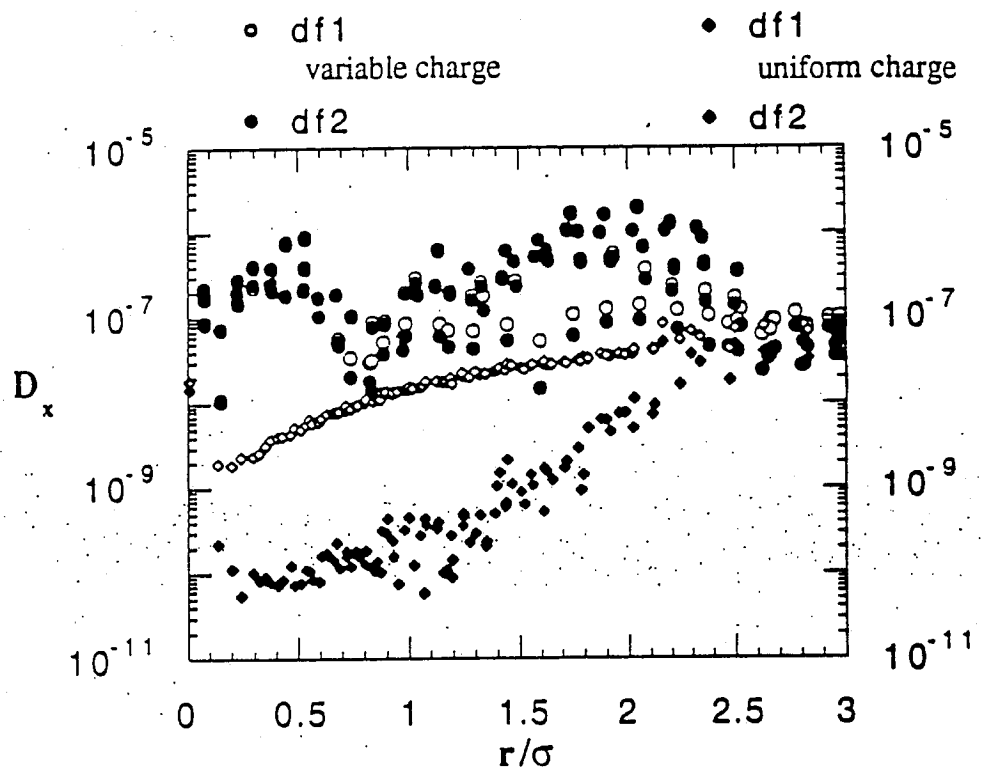

Figure 47: D_x from the strong-stong code with the variable charge and uniform charge particle initialization for $M = 10240$ rotations. df1 and df2 have time scales of $\Delta N_1 = 102$ $\Delta N_2 = 1024$ rotations respectively.

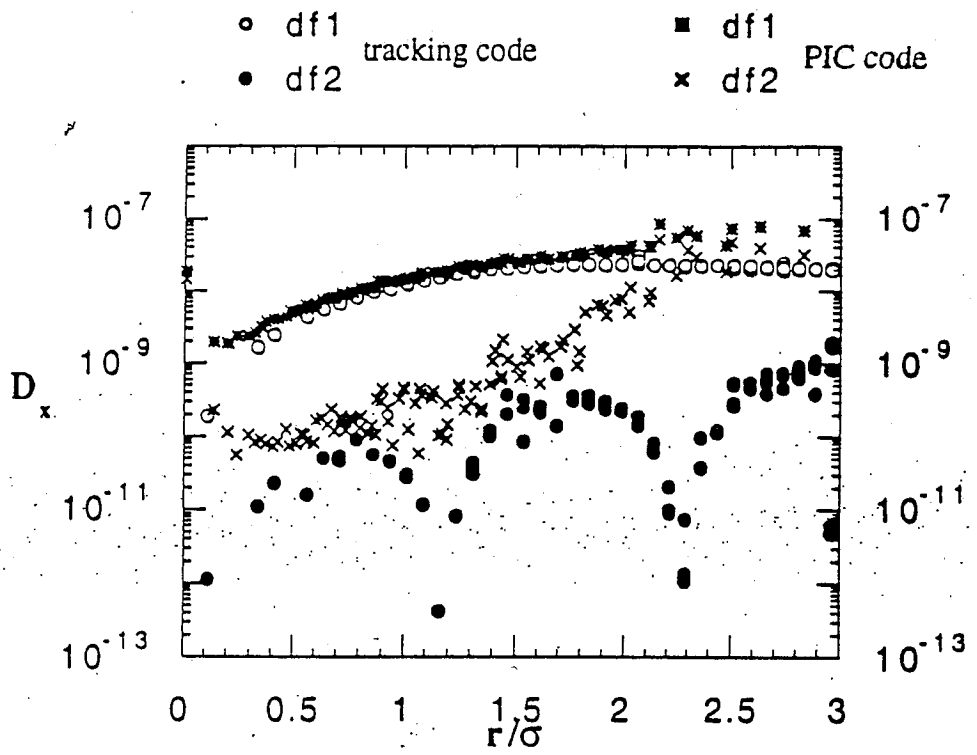

Figure 48: D_x from tracking code and the strong-stong code with uniform charge particle initialization for $M = 10240$ rotations. df1 and df2 have time scales of $\Delta N_1 = 102$ and $\Delta N_2 = 1024$ rotations respectively.

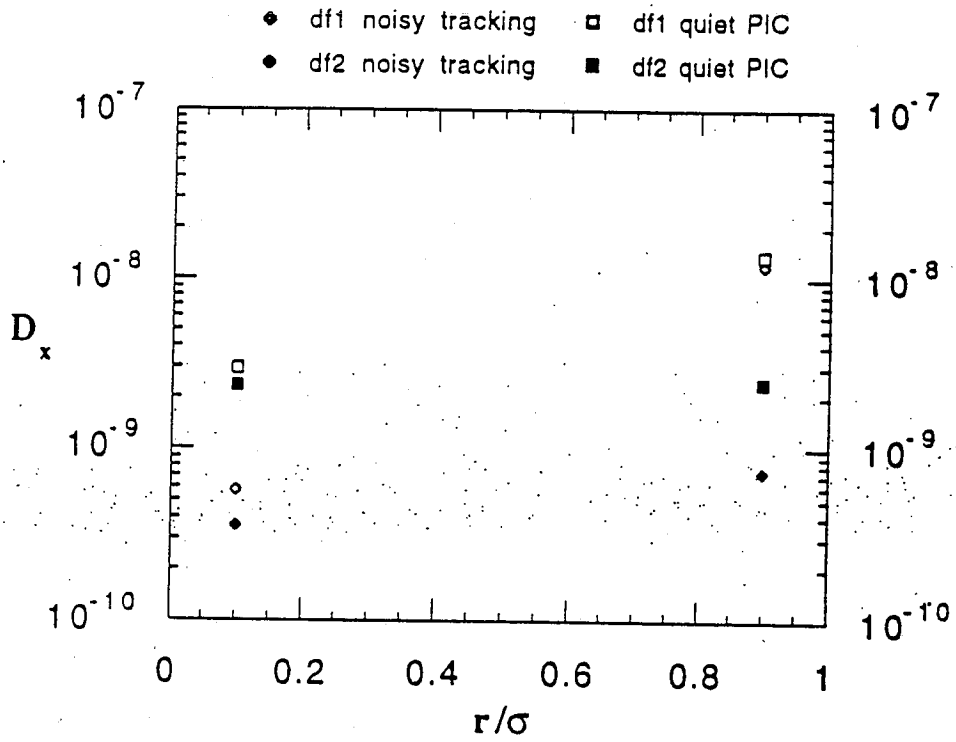

Figure 49: D_x from noisy tracking code and PIC code for $M = 10240$ rotations at $r/\sigma = 0.1$ and 0.9. df1 and df2 have time scales of $\Delta N_1 = 102$ and $\Delta N_2 = 1024$ rotations respectively.

is from finite particle noise. The discrepancy in the diffusion coefficients between the PIC code and the noisy tracking code may be due to other types of numerical noise or collective phenomena.

δf simulation results

In this section we describe particle diffusion results obtained from the δf simulation code described in Sec. 2. SSC reference parameters from Sec. 3 are used with $\nu_0 = 0.285$ and $\Delta\nu_0 = 2.1 \times 10^{-3}$. Each beam in the simulation has 10^3 simulation particles with the initial distribution in (x, p_x) phase space shown in Fig. 3.

The diffusion coefficients are calculated for 100 sample particles after 10240 rotations. As in previous sections the diffusion coefficients, df1 and df2, are calculated using $|x|$ in Eq. (115). The diffusion D_x is normalized to σ_x^2/N_r, where N_r is the number of rotations. Results from the δf code and tracking code after 10240 rotations are shown in Fig. 50. The diffusion coefficients for the δf and tracking code nearly overlay each other. Both codes show oscillatory motion for 10240 rotations. Thus, the noise level of the δf code is less than the strong-strong code with either the variable or uniform charge distribution.

Simulations with 100, 1000, and 10000 particles show little effect on the diffusion of the particles from particle number for $M = 10240$ rotations [Fig. 51]. For 100 simulation particles there is some deviation for sample particles with $r/\sigma < 1$. The noise level is not as strong a function of particle number as the strong-strong code.

The sample particles begin to show diffusive behavior, when the number of rotations is increased. Figure 52 shows the diffusion coefficients, df1 and df2, calculated for 40960 rotations. Particles with $r/\sigma > 2$ are diffusive (df1 $\approx$ df2). This same behavior is observed for 10240 rotations in the strong-strong code with the uniform charge distribution [Fig. 48]. The particles with $r/\sigma < 2$ are still somewhat oscillatory in nature. It appears that the particles in the tail of the distribution are most sensitive to either noise or collective motion

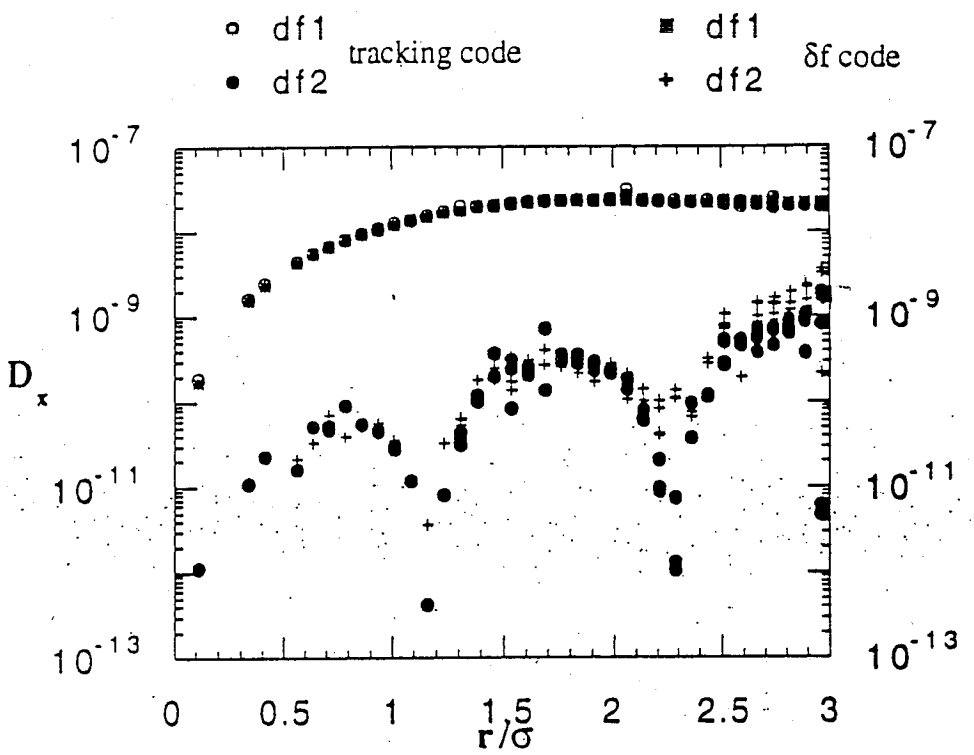

Figure 50: D_x from the δf code with 1000 simulation particles and the tracking code for $M = 10240$ rotations. df1 and df2 have time scales of $\Delta N_1 = 102$ and $\Delta N_2 = 1024$ rotations respectively.

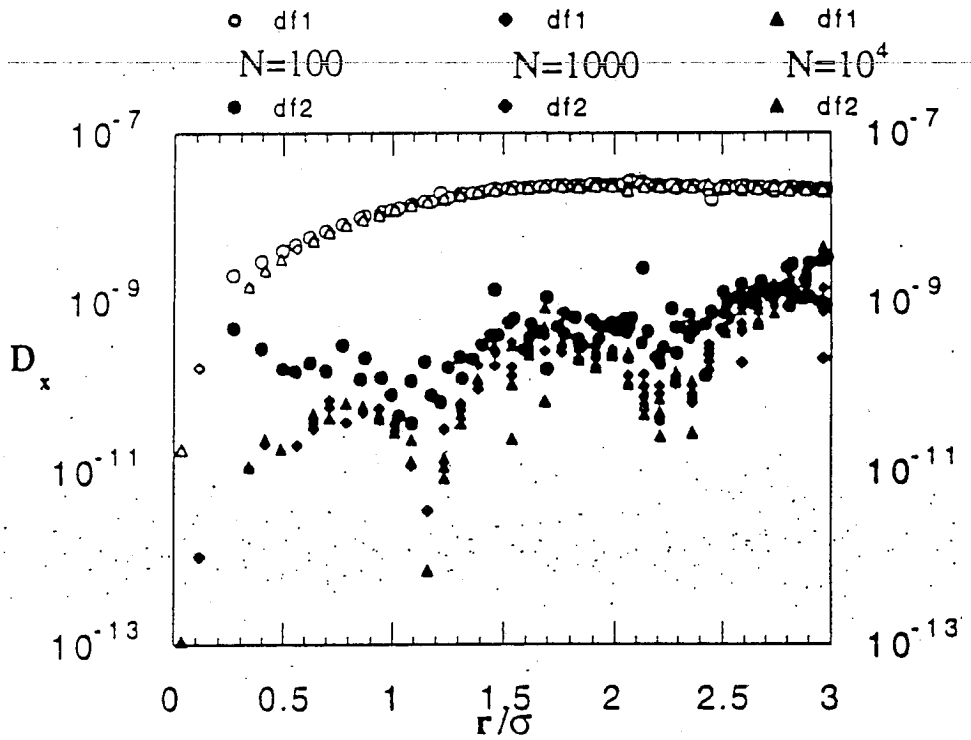

Figure 51: Variation of the diffusion coefficients with particle number N for $M = 10240$ rotations.

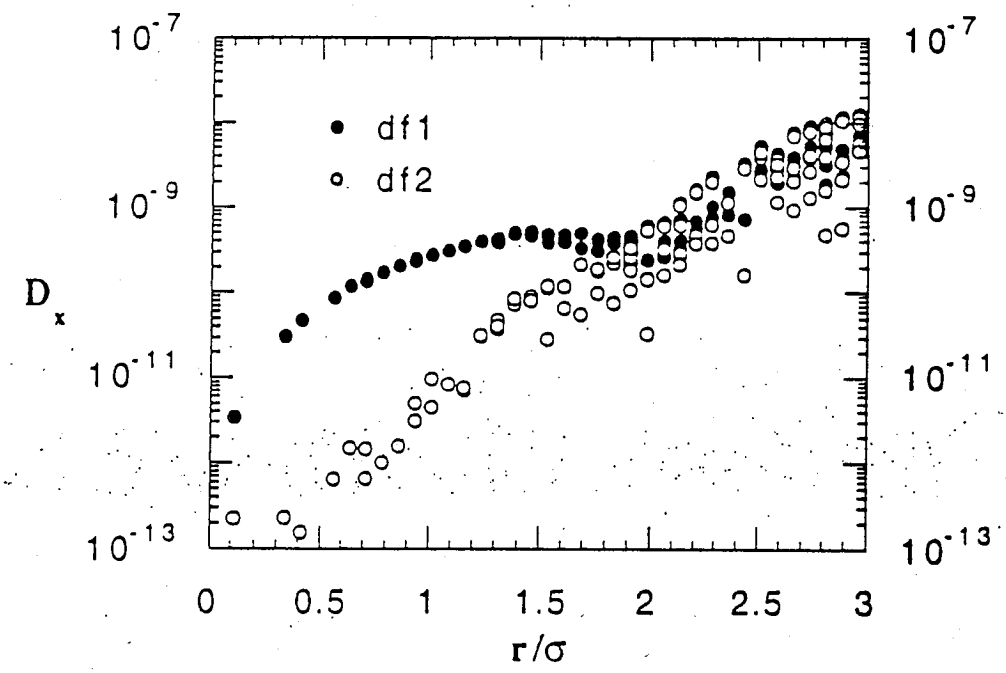

Figure 52: D_x from the δf code with 1000 simulation particles for $M = 40960$ rotations. df1 and df2 have time scales of $\Delta N_1 = 409$ and $\Delta N_2 = 4096$ rotations respectively.

in the beams. This diffusion in the tails is not due to finite particle noise, as is evident in Fig. 53. The figure shows the diffusion coefficients calculated for $N = 1000$ and $N = 10^4$ simulation particles for 40960 rotations. The results are nearly identical.

A comparison of the δf and tracking code at 40960 rotations is shown in Fig. 54. The tracking and δf code diffusion coefficients are nearly equal to the short time scale coefficient df1 with values of $r/\sigma < 1.5$. For the long time scale coefficient df2 and $r/\sigma > 1.5$ the δf code shows more diffusive behavior. This indicates that the phenomenon which causes the diffusive motions at for large r/σ is most evident on time scales of 409 rotations. Diffusive motion is not evident for for particles with $r/\sigma < 1.5$. This indicates that the diffusion occurs on longer time scales there. This is shown in longer runs. It appears that the diffusion is largest for large r/σ and smallest for small r/σ.

In order to determine the source of the diffusion observed in the δf code, noise of the form described in Sec. 2 is added to the tracking code. Figure 55 shows the results for 40960 rotations, where the noise level δ is determined by:

$$\delta = \frac{1}{\sqrt{N(x)}}\,, \tag{125}$$

where $N(x) = N\,\mathrm{erf}\,(x/\sqrt{2}\sigma_x)$ and N is the particle number. Notice that the long time scale coefficient df2 increases for small r/σ and therefore, df2 is more uniform in r/σ. The form of D_x as a function of r/σ is different from D_x calculated from the δf code. It is apparent that the enhanced diffusion observed in the tails of the distribution for the δf code is due to the self-consistent treatment of the beams. This enhanced diffusion in the tails was also observed in the strong-strong code with the uniform charge initialization and fewer rotations.

When the δf code is run for 10^5 rotations, all the sample particles show diffusive behavior [Fig. 56]. The diffusion D_x is an approximately exponential function of r/σ. The coefficients take nearly the same value as the long time scale diffusion coefficient df2 calculated for 40960 rotations [Fig. 52]. The diffusive time scale appears to be in the range of 400 to 4000

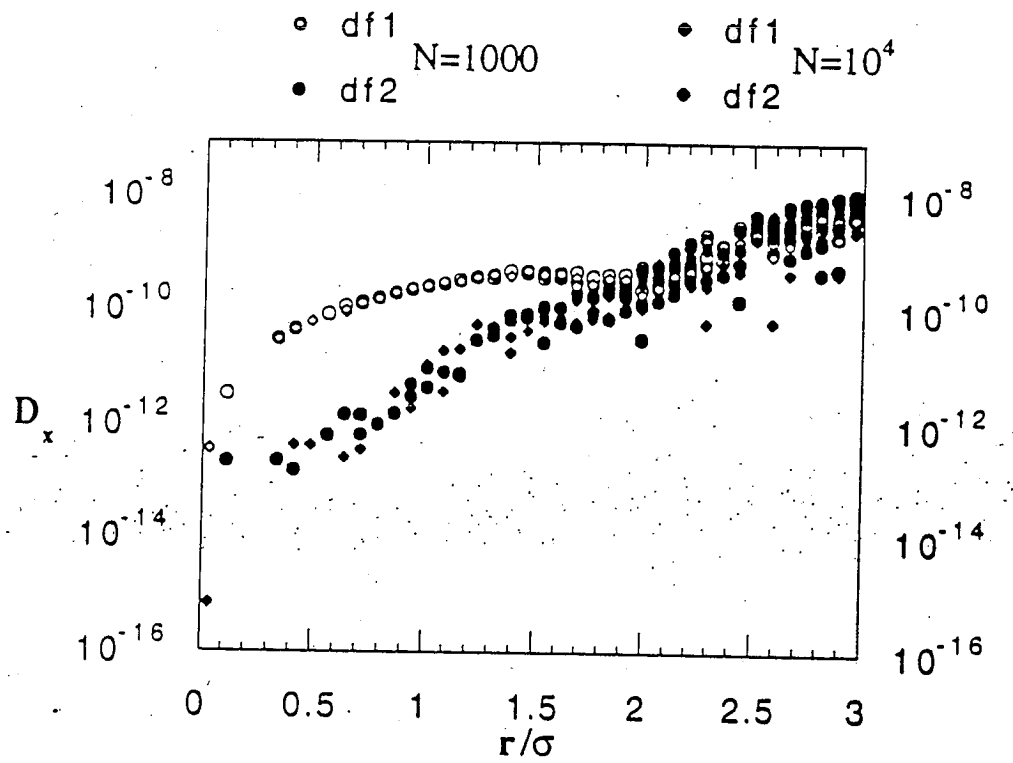

Figure 53: Variation of the diffusion coefficients with particle number N for $M = 40960$ rotations.

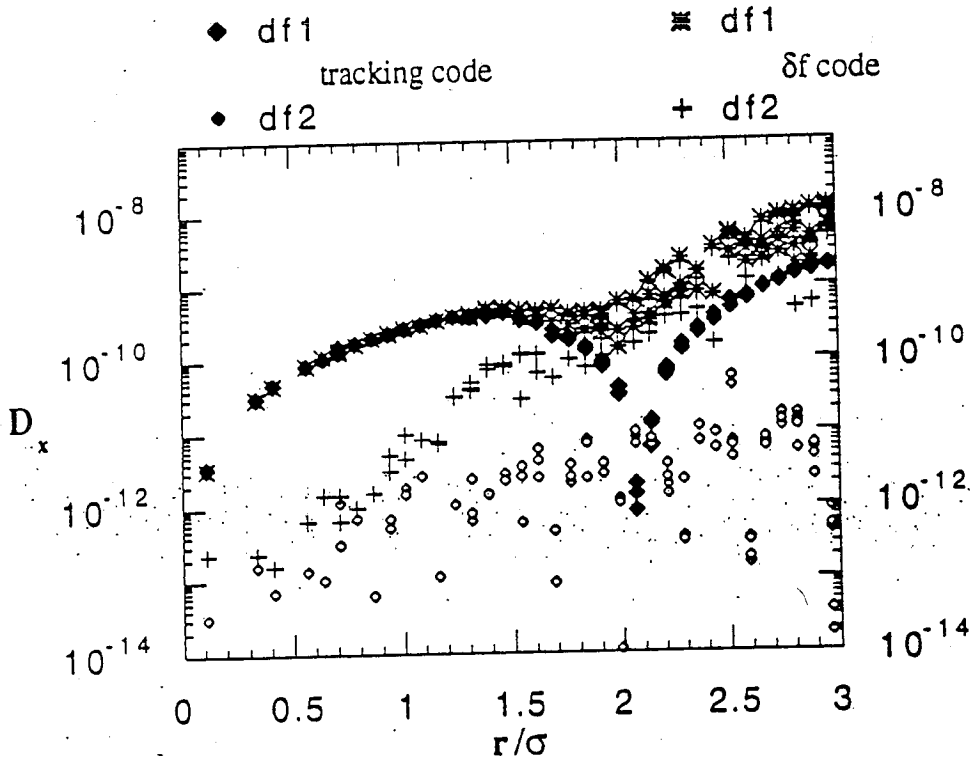

Figure 54: D_x from tracking code and the δf code for $M = 40960$ rotations. df1 and df2 have time scales of $\Delta N_1 = 409$ and $\Delta N_2 = 4096$ rotations respectively.

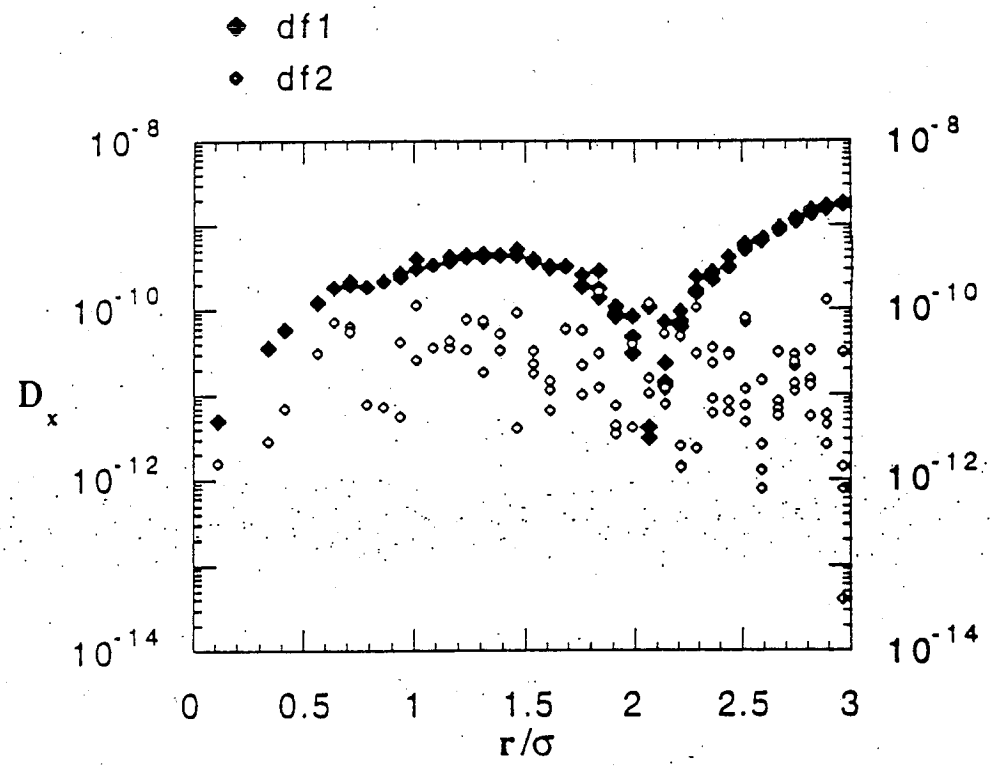

Figure 55: D_x from noisy tracking code for $M = 40960$ rotations. df1 and df2 have time scales of $\Delta N_1 = 409$ and $\Delta N_2 = 4096$ rotations respectively.

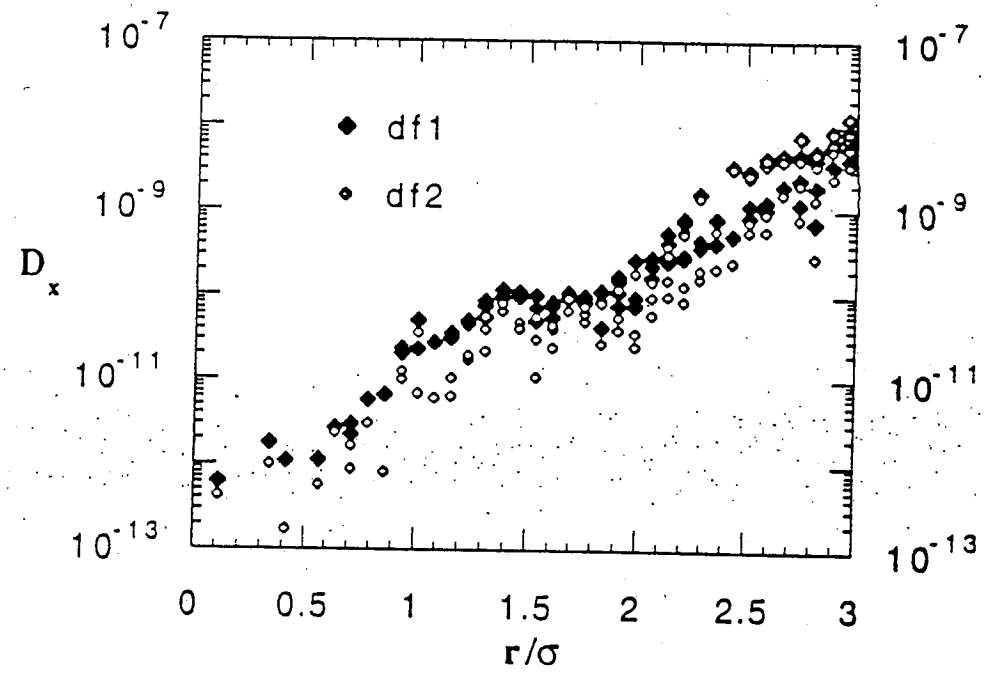

Figure 56: D_x from the δf code for $M = 10^5$ rotations. df1 and df2 have time scales of $\Delta N_1 = 1000$ and $\Delta N_2 = 10000$ rotations respectively.

rotations.

A comparison of the δf and tracking code results at 10^5 rotations is shown in Fig. 57. As in the run with 40960 rotations, the diffusion coefficients obtained from the tracking and δf runs are nearly equal for the short time scale coefficient df1 with values of $r/\sigma < 1.5$. For the long time scale coefficient df2 and $r/\sigma > 1.5$ the δf code shows diffusive behavior and is higher in value than the coefficients from the tracking code.

Figure 58 shows the diffusion coefficients calculated for $N = 1000$ and $N = 10^4$ simulation particles for 10^5 rotations. The coefficients for both particle numbers overlap indicating that the diffusion observed is not strongly dependent on the simulation particle number.

Diffusion from beam offset

In this section we examine the effects of beam offset on particle diffusion. According to analytic theory on beam offset[34] a Fokker-Planck equation can be derived for the averaged perturbation of the distribution function $\Delta F = F - F_0$:

$$\langle \Delta F \rangle = \tfrac{1}{2} \frac{\partial}{\partial J} \left\langle (\Delta J_M)^2 \right\rangle \frac{\partial F_0}{\partial J} , \tag{126}$$

where F_0 is the initial unperturbed distribution function of the beam, J is the action, and $\langle (\Delta J_M)^2 \rangle$ is the averaged change in the action due to beam offsets. $\langle (\Delta J_M)^2 \rangle / 2$ can be thought of as the diffusion coefficient. An expression for $\langle (\Delta J_M)^2 \rangle$ has been derived using the "weak-strong" approximation for the beam-beam interaction and the assumption that the strong beam is Gaussian[34]:

$$\left\langle (\Delta J_M)^2 \right\rangle = 16\pi^2 \xi^2 J_0 \exp(-J_0) M \sum_{k=0}^{\infty} \left(I_k \left(\frac{J_0}{2} \right) + I_{k+1} \left(\frac{J_0}{2} \right) \right)^2 R_k , \tag{127}$$

where ξ is the beam strength parameter, J_0 is the unperturbed action, I_k is the modified Bessel function of order k, and R_k is

$$R_k \equiv \sum_{n=-\infty}^{\infty} K(n) \cos(2\pi\nu n(2k+1)) , \tag{128}$$

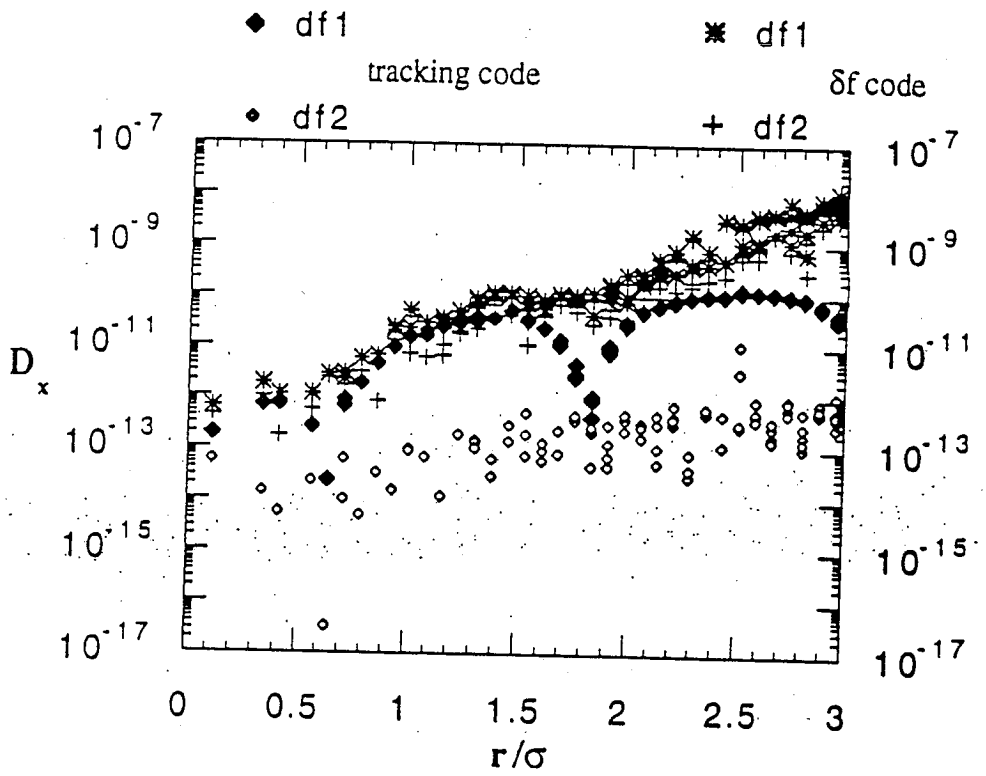

Figure 57: D_x from tracking code and the δf code for $M = 10^5$ rotations. df1 and df2 have time scales of $\Delta N_1 = 1000$ and $\Delta N_2 = 10000$ rotations respectively.

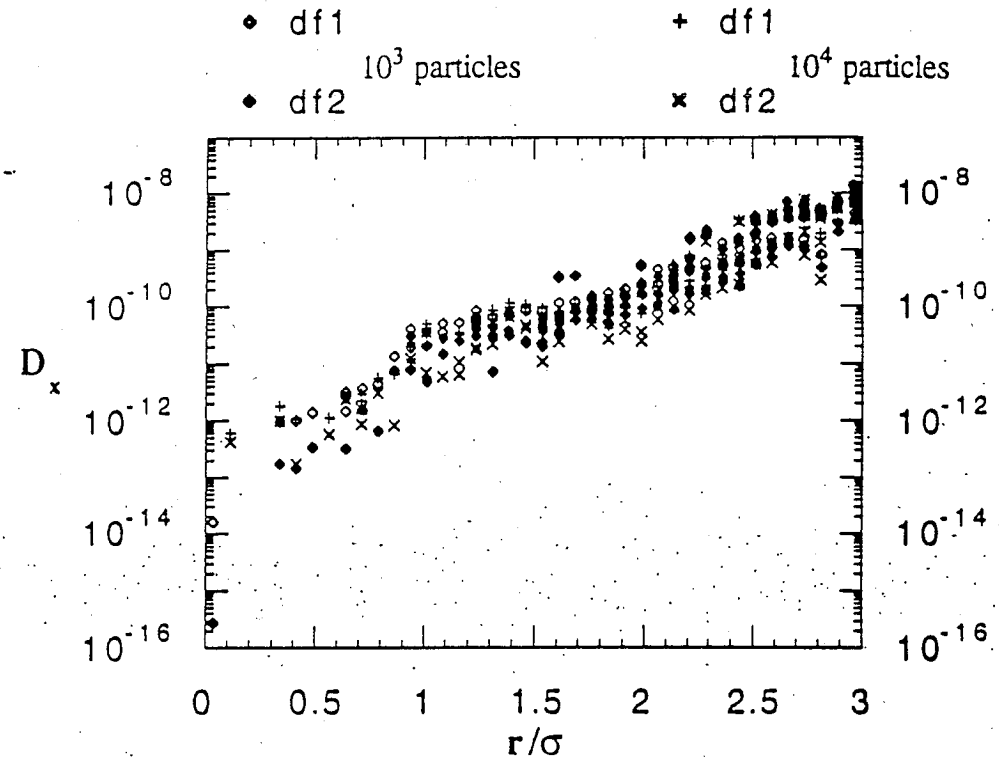

Figure 58: Variation of the diffusion coefficients with particle number N for $M = 10^5$ rotations.

where $K(n)$ is the auto-correlation function $\langle \zeta_m \zeta_{m+n} \rangle$, ζ_m is the beam offset for turn m, and ν is the tune.

Equation (127) can be simplified with the assumption that the beam offsets ζ are uncorrelated on a turn by turn basis. Then, $K(0)$ is the only nonzero term in the calculation of R_k (the Markov process assumption). Also noting that the Bessel functions fall off with k, Eq. (127) can be written in the form[34]:

$$\left\langle (\Delta J_M)^2 \right\rangle = 16\pi^2 \xi^2 J_0 \exp(-J_0) M \left(I_0\left(\frac{J_0}{2}\right) + I_1\left(\frac{J_0}{2}\right)\right)^2 R_0 \,. \tag{129}$$

After integrating over J_0, an approximate value for the diffusion coefficient can be obtained from the change in the luminosity of the beam[34]:

$$\frac{\Delta L}{L_0} = -6.25 \xi^2 M \frac{\delta x^2}{\Delta \nu} \tag{130}$$

where ΔL is the change in luminosity, L_0 is the initial luminosity, ξ is the beam strength parameter, δx is the beam displacement normalized to σ_x, M is the number of turns, and $\Delta \nu$ is the distance of the tune ν from the nearest integer. The diffusion coefficient may be defined as:

$$D = \frac{d\left(\frac{\Delta L}{L_0}\right)}{dM} \,. \tag{131}$$

Thus, D can be expressed in the form:

$$D = -6.25 \xi^2 \frac{\delta x^2}{\Delta \nu} \,. \tag{132}$$

Simulation results are compared with the theoretical predictions of Stupakov.[34] A tracking code and a δf code are used to compare with Eq. (129). Parameters from the Superconducting Super Collider (SSC) are used to compare the analytic results with the simulation results. In this case $\nu = 0.285$ and $\Delta\nu = \xi = 2.1 \times 10^{-3}$. These numbers can be used to get an approximate number for the diffusion from Eq. (132). An estimate of δx can be obtained from plots of the average x position of the beam versus the number of rotations M [Fig. 59]. The estimate of $\delta x = \frac{\Delta x}{\sigma_x}$ is 0.0005. From this an approximate value of the diffusion D is:

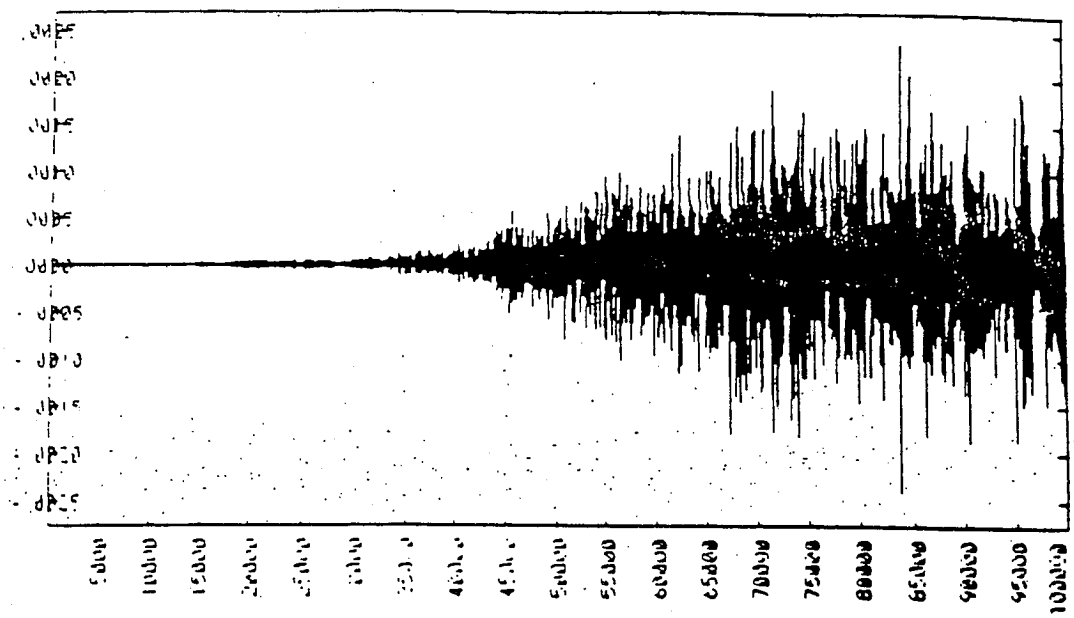

Figure 59: This figure shows $\langle x \rangle / \sigma_x$ versus M from δf simulation with $\nu_0 = 0.285$ and $\Delta\nu_0 = 0.0021$

$$D \approx 10^{-13}\sigma_x^2/\text{turn} \,. \tag{133}$$

Figure 60 shows the total change in the action $\langle(\Delta J_M)^2\rangle$ versus the action J for various values of the beam offset ζ calculated from Eq. (127). The action J is normalized to $p\sigma_x^2/\beta^*$ and the beam offset is normalized to σ_x. The plot is obtained with the assumption that the beam offsets are uncorrelated so that the $k = 0$ term in Eq. (129) is the only nonzero one. The offsets plotted are for $\zeta = 0.0001, 0.001$, and 0.01. Note that $\langle(\Delta J_M)^2\rangle$ increases with ζ as ζ^2, which is expected from Eq. (129).

Figure 61 shows tracking code and analytic results. The tracking code is run for $M = 10^5$ turns with $\nu_0 = 0.285$ and $\Delta\nu_0 = 2.1 \times 10^{-3}$. The total change in the action $\langle(\Delta J_M)^2\rangle/2$ is divided by M, the number of turns, to get the change per turn. The data points represent 100 uniformly distributed tracking particles which are run for each value of the beam offset ζ. As is evident in Fig. 61 the diffusion coefficients (df1, df2) calculated on different time scales for each particle are close to one another indicating that all the particles show diffusive behavior. There is good agreement between the tracking code results and the analytic predictions based on the random offset model of Stupakov.[34] Both show the leveling off in the diffusion with increasing values of the action J.

The δf code results over 10^5 turns are shown in Fig. 62. The δf code is started with zero offset and allowed to evolve self-consistently for $M = 10^5$ turns. Analytic results for 3 values of the beam offset, $\zeta = 0.01$ to $0.0001\sigma_x$, are shown in the background while the simulation value of ζ is in the range of 0.0005 to $0.001\sigma_x$. As is evident in the figure, the values of the diffusion in the action variable J crosses the range of the analytic prediction. However, the functional dependence on the action J is very different. The δf results show an exponential dependence on the action J for large values of J, whereas the Stupakov theory shows the diffusion leveling off.

Figure 64 shows the results of using the output $\langle x\rangle$ from the δf code shown in Fig. 59 in

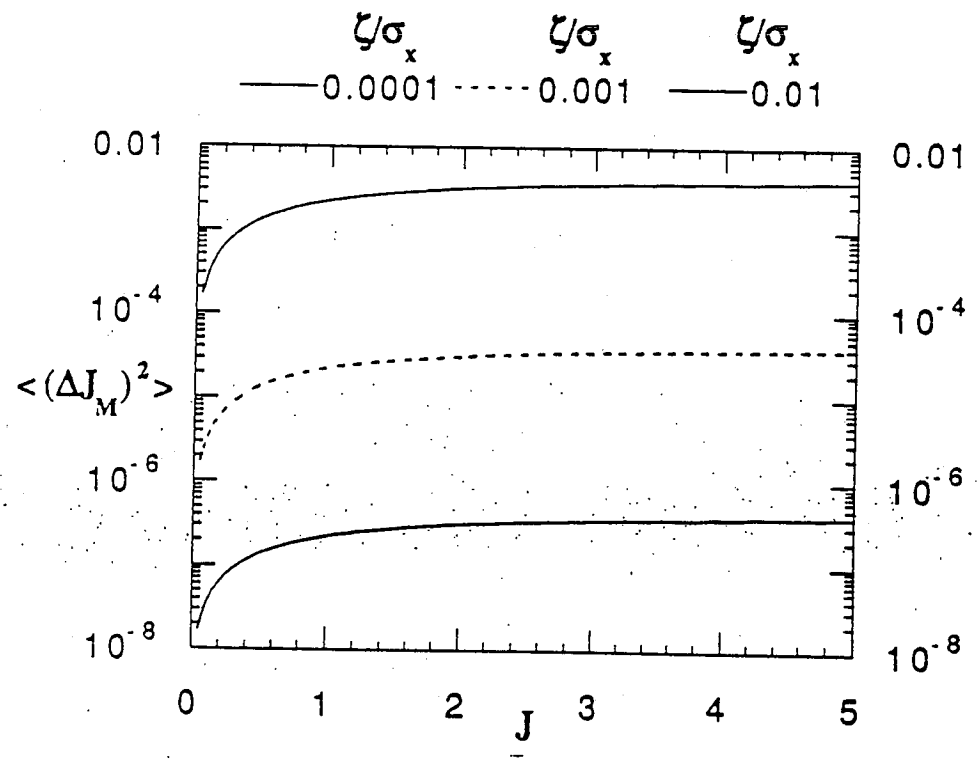

Figure 60: The total change in the action ΔJ_M versus the action J for three values of the beam offset ζ

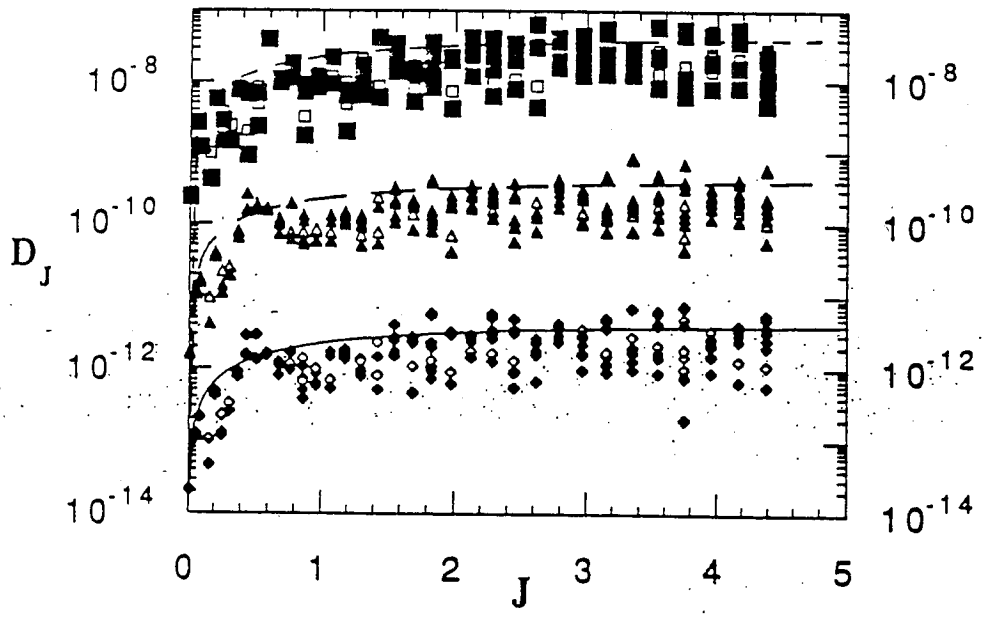

Figure 61: Tracking code results showing the change in $\langle(\Delta J_M)^2\rangle$ /2 per turn versus the action J for three values of the beam offset ζ. The time scales over which df1 and df2 are calculated are 10^3 and 10^4 rotations respectively.

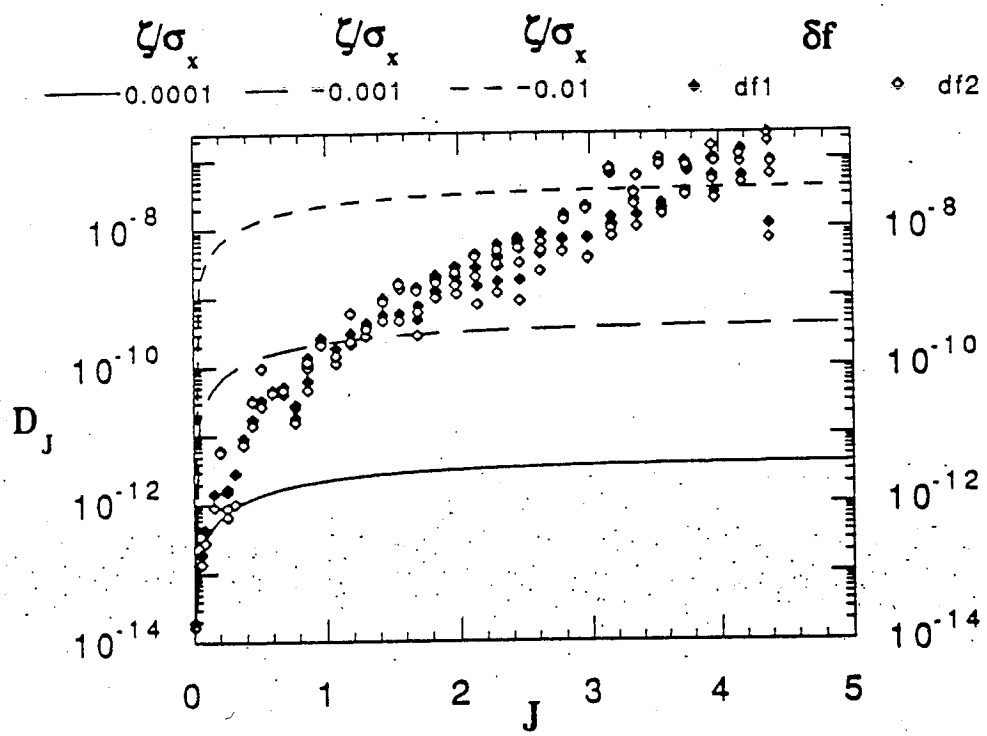

Figure 62: δf code results showing the change in the action ΔJ_M per turn versus the action J for zero initial beam offset. The time scales over which df1 and df2 are calculated are 10^3 and 10^4 rotations respectively.

the tracking code. Analytical results are also plotted for various values of the beam offset ζ. The tracking code and analytic results show the same functional behavior with respect to J. The corresponding beam offset is in the range $\zeta = 0.001$ to 0.01. Although the diffusion from the tracking code is in the same range as the δf code results, the exponential behavior for large J is not seen [Fig. 64].

The leveling off in the diffusion is produced in the δf code when the beam strength is increased. When the tune shift is increased from $\Delta\nu_0 = 2.1 \times 10^{-3}$ to $\Delta\nu_0 = 8.4 \times 10^{-3}$, the resulting motion of the beam about the original beam center increases by approximately an order of magnitude [Fig. 65]. The diffusion coefficients D_x calculated for $\Delta\nu_0 = 2.1 \times 10^{-3}$ and $\Delta\nu_0 = 8.4 \times 10^{-3}$ are shown in Fig. 66. It is evident from the figure that the diffusion increases for the small amplitude particles ($r/\sigma < 2$) when $\Delta\nu_0$ is increased to 8.4×10^{-3}. The net effect is uniform diffusion across the beam in this case. The resulting diffusion is similar to that of beam offset diffusion.[34]

This same behavior is seen in the strong-strong simulations. Figure 67 shows the diffusion coefficients calculated for the PIC and the δf codes. The leveling off in the diffusion is seen for the PIC code and not the δf code. The δf code for $M = 10240$ rotations still shows oscillatory behavior for all values of r/σ.

It appears as if the fluctuation level of the simulation determines whether the diffusion due to the presence of nonvanishing $\langle x \rangle$ suggested by Stupakov[34] dominates the particle diffusion. In the cases where the fluctuation level is high either from the strength of the kick $\Delta\nu_0$ or from simulation noise the $\langle x \rangle$ type of diffusion dominates.

Diffusion from beam breathing

We have found that the alternate breathing oscillations of the two beams appear in the self-consistent calculations, but not in the tracking calculations. The onset of the oscillations is due to the collective interaction. In this section we examine the effects of this breathing on

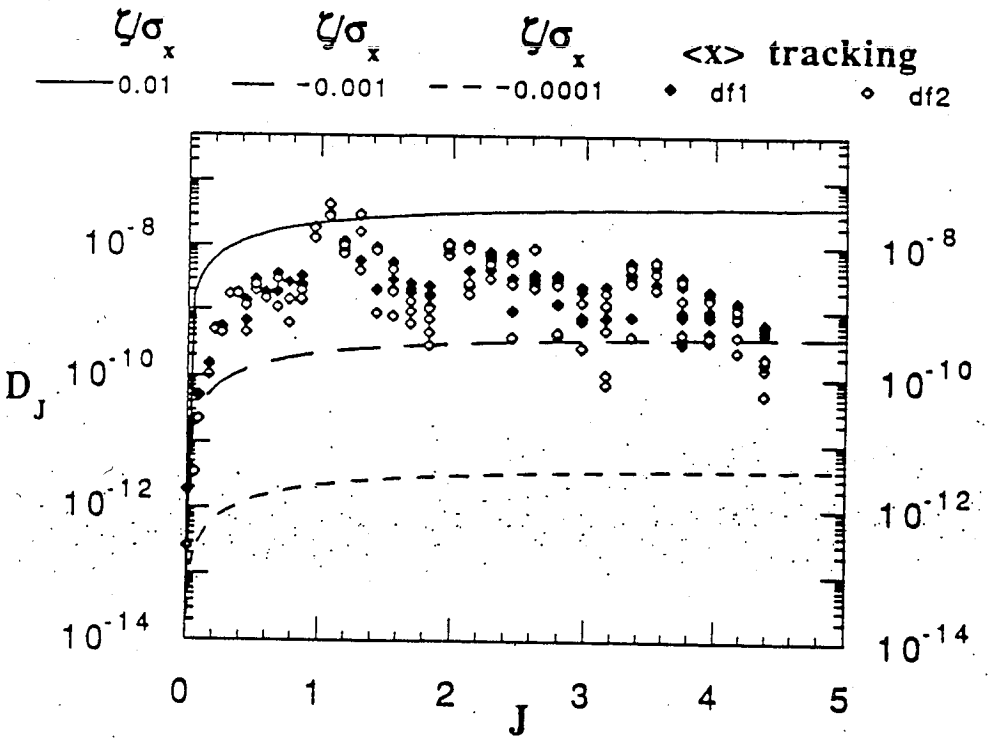

Figure 63: A comparison of tracking code with input $\langle x \rangle$ and theory

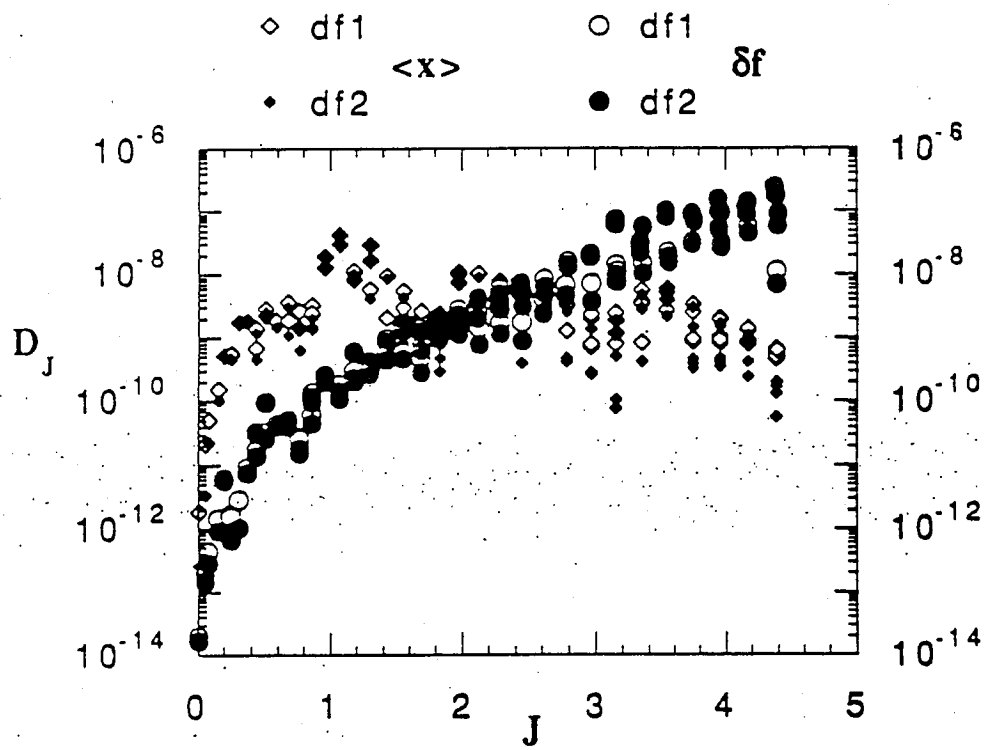

Figure 64: A comparison of tracking code with input $\langle x \rangle$ and δf results

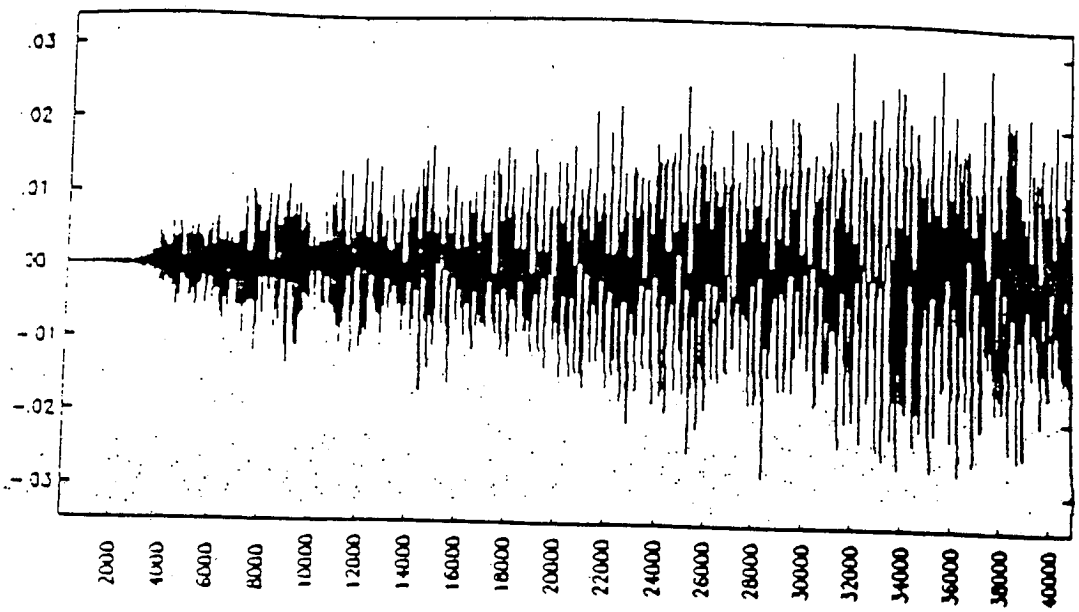

Figure 65: $\langle x \rangle$ of the beam with $\Delta\nu_0 = 8.4 \times 10^{-3}$

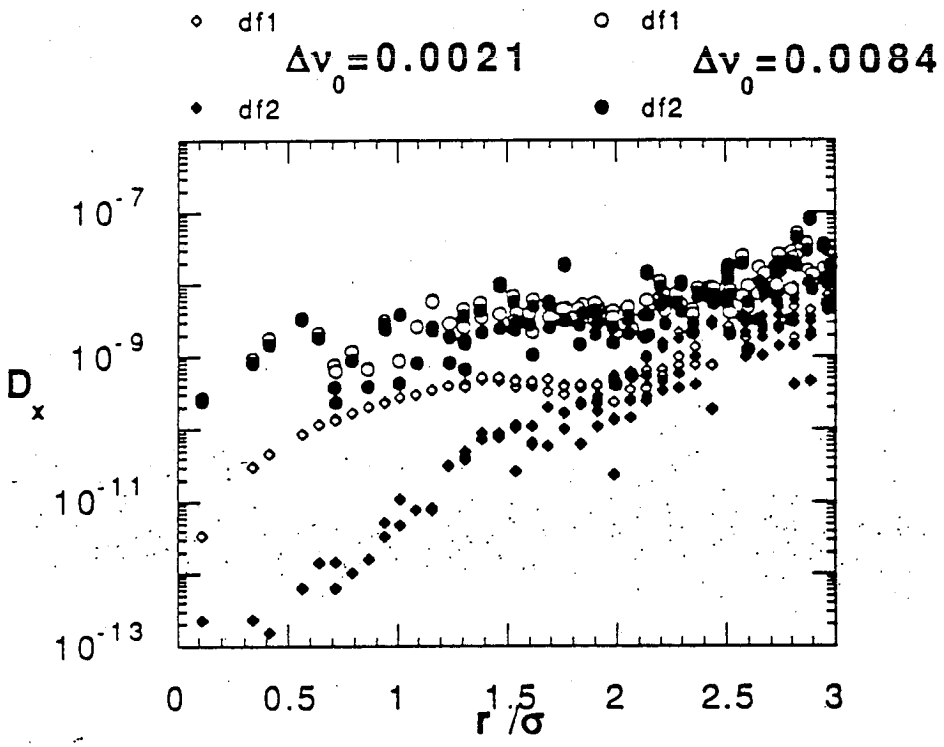

Figure 66: D_x of the beam with $\Delta\nu_0 = 2.1 \times 10^{-3}$ and $\Delta\nu_0 = 8.4 \times 10^{-3}$ for $M = 40960$ rotations and the time scales of df1 and df2 being 409 and 4096 rotations respectively.

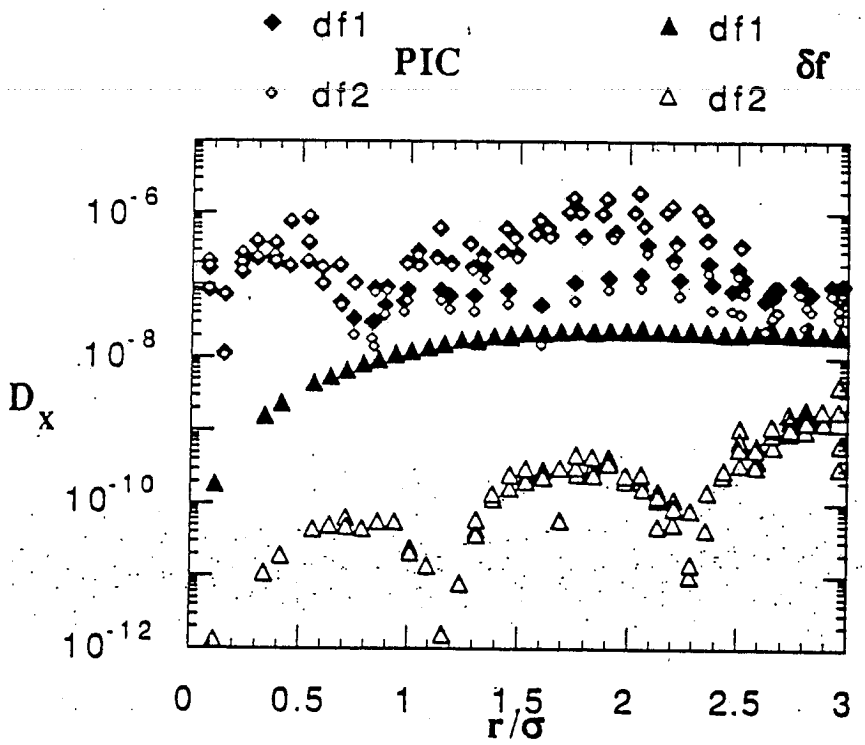

Figure 67: D_x from PIC and δf codes of the beam with $\Delta\nu_0 = 2.1 \times 10^{-3}$ for $M = 10240$ rotations. df1 and df2 have time scales of 102 and 1024 rotations respectively.

particle diffusion.

Figure 68(a) shows the diffusion coefficients of 100 randomly distributed sample particles versus their initial action calculated for the δf code and the tracking code, where the normalized action is $J = \frac{1}{2}((\frac{x}{\sigma_x})^2 + (\frac{p_x}{\sigma_p})^2)$.

The diffusion coefficients are obtained after 10^5 rotations using SSC reference parameters. The diffusion coefficient $D(J)$ in the action is normalized to σ_J^2/N_r, where $\sigma_J = {\sigma_x}^2/\beta^*$ and N_r is the number of rotations so that it takes $D(J)^{-1}$ turns to diffuse over one standard deviation of the beam emittance. For example, Fig 68(a) shows on average the diffusion time is approximately 10^{10} turns in our self-consistent calculations. In Fig. 68(a) the ratio of the coefficients calculated over intervals of 10^3 and 10^4 turns for the tracking code sample particles is on the order of $\frac{D_2}{D_1} \sim 0.01 \rightarrow 0.1$ which indicates little diffusive behavior.

In Fig. 68(a) for all sample particles in the δf code the ratio D_2/D_1 is on the order of 1, indicating that all particles are diffusive. The diffusion coefficient $D(J)$ is an approximately exponential function of J for $J > 0.5$. The diffusion is not strongly dependent on the number of simulation particles. In this δf simulation each beam has 10^3 simulation particles; however, the coefficients calculated for a simulation with 10^4 simulation particles give the same results.[21]

The source of the enhanced diffusion in the self-consistent δf simulation is identified with the observed variation of the moments of each beam which does not occur in the tracking code. The contribution of the first two beam moments $\langle x \rangle$ and $\langle x^2 \rangle$ to the beam diffusion may be estimated by varying these moments in the tracking code which assumes a Gaussian beam.

When the beam moment $\langle x \rangle$ from the δf code is input into the tracking code, the diffusion coefficients calculated for sample particles with $J < 1$ are close to that of the δf code. However, for $J > 1$ the diffusion coefficients level off and deviate substantially from the exponentially increasing diffusion coefficients of the δf code. Figure 68(b) shows diffusion

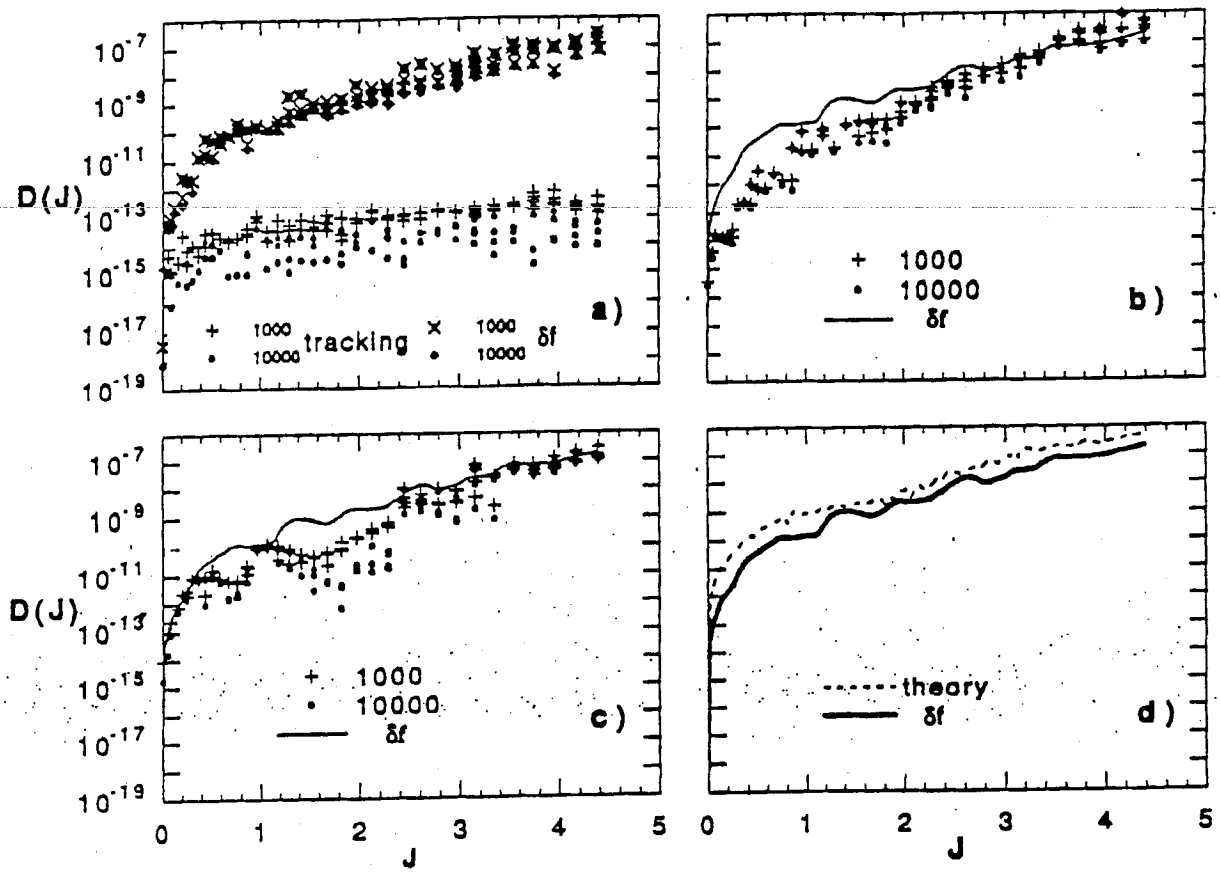

Figure 68: $D(J)$ from (a) our δf code and conventional tracking code, (b) tracking code particles with variations in $\langle x^2 \rangle$ input from the δf, and (c) tracking code particles with $\langle x^2 \rangle$ input using a band of frequencies around $2(\nu_0 - \Delta\nu)$ for $M = 10^5$ rotations. D_1 and D_2 have time scales of $\Delta N_1 = 1000$ and $\Delta N_2 = 10000$ rotations respectively. (d) The diffusion $D(J)$ from δf and our analytic theory.

coefficients from the tracking code particles when the beam σ_x of the tracking code is varied using $\langle x^2 \rangle$ from the δf code. The solid curve for the δf diffusion is obtained by smoothing the diffusion coefficients calculated for 10000 rotations. The diffusion coefficients from the tracking code with the appropriate spectrum of variations of $\langle x^2 \rangle$ and the δf code nearly overlap for most values of $J > 2$. For values of $J < 2$ the tracking code coefficients are smaller than the δf code. Thus, most of the enhanced diffusion can be accounted for by the variation of the second moment $\langle x^2 \rangle$ incurred by collective 'breathing' modes. Diffusion at the core of the beam can be accounted for by the variations in both the first $\langle x \rangle$ and second $\langle x^2 \rangle$ moments.

Figure 69(a) shows a portion of the frequency spectra $S_J(f)$ of four different sample particles initially at $J = 1, 2, 3$, and 4 over $M = 10^5$ rotations where

$$S_J(f) = \mathrm{FFT}[C(r)W(r)] \ . \tag{134}$$

$C(r)$ is the correlation function which is calculated from a discrete set of values of the action J for each particle[18]:

$$C(r) = \frac{1}{M-r} \sum_{n=1}^{M-r} J(n)J^*(n+r) \ , \tag{135}$$

where $r = 0, ..., m$, r is the rotation lag, m is the maximum rotation lag, and M is the total number of rotations. $W(r)$ is a window function and FFT is a Fast Fourier Transform with M rounded to the nearest power of 2. The frequency f of the peak in $S_J(f)$ is decreasing with increasing initial J of each sample particle and corresponds approximately to $f = 1 - 2(\nu_0 - \Delta\nu(J))$ where $\Delta\nu(J)$ is the tune shift of the particular particle. The decrease in frequency can be attributed to the decrease in $\Delta\nu(J)$ with increasing J of the particle, typical of the beam-beam tune shift. Figure 69(b) shows a portion of the frequency spectrum $S_{\sigma_x}(f)$ where the second moment of motion $\sigma_x = \sqrt{\langle x^2 \rangle}$ for $M = 10^5$ rotations is used in Eq. (135). The arrows indicate the upper and lower bounds of frequencies accessible to particles in the beam. The upper and lower bounds correspond to particles at the center

of the beam experiencing the full tune shift $\Delta\nu_0$ and particles with $J \to \infty$ experiencing no tune shift, respectively. The frequency f of the peak in Fig. 69(b) of the σ_x motion is approximately $1 - 2(\nu_0 - \Delta\nu)$ where $\Delta\nu$ is the tune shift of the large J particles. Sample particles with large J are in resonance with the σ_x variation. Sample particles with small J have a characteristic frequency f in their motion which is higher than the σ_x frequency and are not in resonance. Therefore, the main contribution to the diffusion of the large J particles is resonance overlap.[7]

Figure 68(c) shows the diffusion coefficients obtained from the input of $\langle x^2 \rangle$ variation into the tracking code including only the band of frequencies f shown in Fig. 69(b). There are some particles in the range $1 < J < 2.2$ whose diffusion coefficients are lower than that obtained from the δf simulation. However, the diffusion observed in the δf code can be mostly accounted for by the variation of $\langle x^2 \rangle$ in a narrow band of frequencies near $1 - 2(\nu_0 - \Delta\nu)$ where $\Delta\nu$ is that for large amplitude particles.

The variation in $\langle x \rangle$ does not contribute as significantly to the particle diffusion in J as $\langle x^2 \rangle$. The characteristic frequencies of the $\langle x \rangle$ motion is not as close to the characteristic frequencies of the J variation as the $\langle x^2 \rangle$ motion.

An analytic expression for the diffusion in action J can be obtained for beam σ_x variation by adapting the formalism of Stupakov[34] which contained external kicks with $\langle x \rangle$ variation, but no $\langle x^2 \rangle$ variation. The change in the action due to the beam-beam kick from a one dimensional Gaussian slab can be written in the form:

$$\Delta J = (2\pi)^{3/2} \Delta\nu_0 \sigma_x x' \mathrm{erf}\left(\frac{x}{\sqrt{2}\sigma_x}\right) , \tag{136}$$

where

$$x = \sqrt{2J\beta}\cos(\Psi) , \qquad x' = -\sqrt{\frac{2J}{\beta}}\sin(\Psi) , \tag{137}$$

and Ψ is the phase advance. Perturbing Eq. (136) with respect to σ_x and summing over M

turns one obtains an expression for the change in the action J :

$$\Delta J_M = 8\pi\Delta\nu_0 \sum_{l=0}^{M-1} J_l \exp\left(-\frac{J_l\beta}{2\sigma_{x_0}^2}\right) \sum_{k=0}^{\infty}\{I_k -$$

$$I_{k+2}\}(-1)^k \sin[2(k+1)\Psi_l] \frac{\Delta\sigma_x(l)}{\sigma_{x_0}} , \tag{138}$$

where I_k represents the k-th modified Bessel function with arguments $(\frac{J_l\beta}{2\sigma_{x_0}^2})$. The phase advance is $\Psi_l = 2\pi l(\nu_0 + \langle\Delta\nu(J)\rangle)$ where $\langle\Delta\nu(J)\rangle$ is the average tune shift that the particle encounters.

The diffusion coefficients can be calculated from:

$$D(J) = \frac{\langle\Delta J_M^2\rangle}{M} , \tag{139}$$

where

$$\Delta J_M^2 = 32\pi^2\Delta\nu_0^2 J^2 \exp\left(-\frac{J\beta}{\sigma_{x_0}^2}\right) \times$$

$$\sum_{n=-\infty}^{\infty} K(n) \sum_{k=0}^{\infty}(I_k - I_{k+2})^2 \cos[2(k+1)\Psi_n] . \tag{140}$$

Equation (140) is obtained by squaring Eq. (138) and assuming that the action, J, is not varying much over the M turns. $K(n)$ is the correlation function of the σ_x variations over turn n:

$$K(n) = \sum_{m=0}^{M-1} \frac{\Delta\sigma_x(m)}{\sigma_{x_0}} \frac{\Delta\sigma_x(m+n)}{\sigma_{x_0}} \Big/ M . \tag{141}$$

The correlation function may be defined in terms of the power spectrum, $S_{\sigma_x}(\omega)$:

$$S_{\sigma_x}(\omega) = \sum_{n=1}^{M} K(n) \exp(i\omega n) . \tag{142}$$

Using this expression in Eq. (140) and substituting into Eq. (139) we get

$$D(J) = 32\pi^3\Delta\nu_0^2 J^2 \exp(-\frac{J\beta}{\sigma_{x_0}^2}) \sum_{k=0}^{\infty}(I_k - I_{k+2})^2 S_{\sigma_x}(\omega_k) , \tag{143}$$

where $\omega_k = 2(k+1)2\pi(\nu_0 + \langle\Delta\nu(J)\rangle)$. The peak in the power spectra $S_{\sigma_x}(f)$ in Fig. 69(b) is near $4\pi\nu_0$ which corresponds to $k = 0$ in Eq. (143). Figure 68(d) shows the diffusion obtained from Eq. (143) for $k = 0$. The value of $S_{\sigma_x}(f)$ in Eq. (143) for a particular action J is obtained from measuring the frequency of the peak in the power spectra of the sample particle with that initial J [Fig. 69(a)]. Reasonable agreement between the δf computation and this analytic expression is found. If we used naive approximations for the correlation function such as the Lorentzian, we were unable to reproduce the exponential J dependence of $D(J)$ for $J > 0.5$.

In summary, through our extensive computation and theory we have discovered that the diffusion obtained from the self-consistent δf code is several orders of magnitude higher than that of the prediction from conventional tracking codes. The essence of the culprit of this enhanced diffusion is captured by the variation of the second moment of the beams $\langle x^2\rangle$ which is the result of beam-beam interaction induced collective variations of the beam distribution. However, the numerical level of the diffusion in this 1D simulation study indicates that the level of diffusion is still permissible for the design parameters of SSC. The 2D effects may, on the other hand, further degrade the diffusive behavior of beams.

III Conclusions

In this chapter we discuss the results and their relevance of our investigations of the beam-beam interaction to modern circular accelerators. Also we present future improvements which can be made to the currently developed numerical tools.

Summary of results

We have examined the effects of collective interactions between counterstreaming proton beams via various simulation techniques. Three types of code have been developed in increasing sophistication to study the beam-beam interaction: (1) a tracking code, (2) a

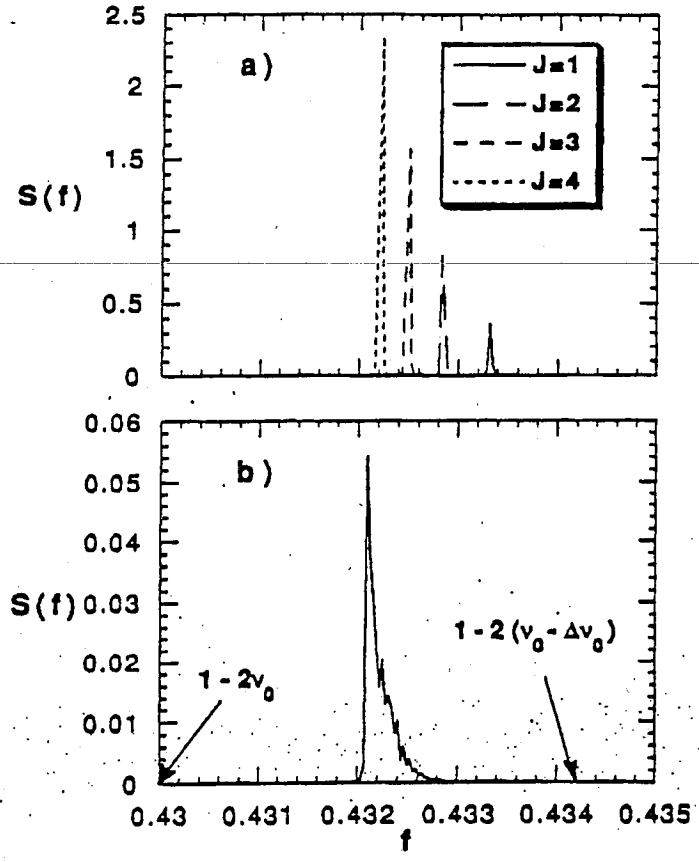

Figure 69: After $M = 10^5$ rotations (a) part of the frequency spectra of the variation of the action J of four different sample particles from the tracking code with initial values of $J = 1, 2, 3$, and 4 and (b) part of the spectra of the variation of σ_x from the δf simulation where the arrows indicate the range frequencies possible for particles in the beam. The upper and lower bound of frequencies correspond to particles with $J = 0$ ($\Delta\nu = \Delta\nu_0$) and $J \to \infty$ ($\Delta\nu = 0$), respectively.

strong-strong code, and (3) a δf code.

Collective beam-beam effects

Among the codes developed, the strong-strong and δf codes are best suited for studying beam-beam collective effects. An electromagnetic PIC code requires too many time steps to cover one interaction time and the tracking code does not show beam collective motions. The strong-strong code's main drawback is the amount of fluctuation noise produced by the finite number of particles used. This noise may be reduced by initializing the particles using the quiet start.[3] Also, although the δf code is much quieter than the strong-strong code, it is better suited for studying the beam-beam interaction away from resonances.

In the strong-strong simulations using the reference parameters of the SSC oscillations in $\Delta\nu$ are observed. The oscillations indicate expansion and contraction of the beams. The beam expansion and contraction varies with different particle positions. The small amplitude portion of the beam is increasing in oscillation amplitude while the entire beam is decreasing in oscillation amplitude. The odd moments of the beam, $\langle x \rangle$ and $< (x - \langle x \rangle)^3 >$, are increasing in oscillation amplitude with rotation number. The amplitudes of the even moments, $< (x - \langle x \rangle)^2 >$ and $< (x - \langle x \rangle)^4 >$, both decrease with the number of rotations. The phenomena of the "flip-flop" effect,[19] where one beam is decreasing in phase space area and the other beam is increasing, is observed in our simulations. It is found to be sensitive to the initial conditions.

Differences between the nonuniform charge and uniform charge initializations are found. The beam distribution from the uniform charge initialization is smoother than the distribution from the nonuniform charge distribution at the beginning and end of the simulation. The oscillations in $\Delta\nu$ indicate that the expansion and contraction of the beam with uniform charge initialization is smaller than the nonuniform charge initialization. Overall the fluctuation levels in the uniform charge initialization are smaller than in the nonuniform charge

initialization.

The simulations based on the δf algorithm show the lowest fluctuation levels of all the codes except the tracking code. However, the tracking code does not include internal dynamics of the beam. After 10^5 rotations the two main approximations of the δf code are still valid. The deviation from the initial Gaussian distribution is still small. The maximum perturbations to the Gaussian background is only 0.1% of the background distribution. Also, the constant phase space density assumption remains to be a good approximation. After 10^5 rotations in the δf code the simulation particles are no longer uniformly distributed in $(x/\sigma_x, p_x/\sigma_p)$ space. However, clumping of particles is not significant. In the simulations using the reference SSC parameters the amplitude of the variation in $\Delta\nu$ for small amplitude particles is approximately $\pm 3\%$ of $\Delta\nu_0$ throughout the run. As observed in the strong-strong simulations, the beams are expanding and contracting differently at different particle positions. The small amplitude portion of the beam is constant oscillation amplitude, while the entire beam is increasing in oscillation amplitude. The odd moments, $\langle x \rangle$ and $< (x - \langle x \rangle)^3 >$, are both increasing in oscillation amplitude with rotation number. This increase in the odd moments is also observed in the strong-strong simulations.

Stability in the tune versus tune shift space

Scans in parameters tune and tune shift, ν_0 and $\Delta\nu_0$, show regions of stability and instability against the beam blowup. These regions correspond closely to the regions predicted by the linear theory of Chao and Ruth.[5] For small values of the tune shift $\Delta\nu_0$ the beams are unstable just above a resonance. For beams with values of ν_0 just below a resonance the the beams are stable. Strong resonant beam blowup is observed just above $\nu_0 = 1/2$ and $\nu_0 = 1/4$ for values of $\Delta\nu_0 = 2.1 \times 10^{-3}$. Just below these tune values the beams are stable, as expected. However, each of the beams show dominant modes distorting the beams in in $(x/\sigma_x, p_x/\sigma_p)$ space. For $\nu_0 = 1/2 - \Delta\nu_0$ mode 2 dominates and for $\nu_0 = 1/4 - \Delta\nu_0$ mode

4 dominates. It is also found that the rate of beam blowup above the resonance drops with the order of the resonance. With $\nu_0 = 1/2 + \Delta\nu_0$ the beams blow up very quickly within a few hundred rotations. The beams blow up more slowly for $\nu_0 = 1/4 + \Delta\nu_0$. The slowest beam blowup is observed for $\nu = \nu_0 + \Delta\nu_0$, where in the case of two beams $\nu_0 = 2/6$ and $\Delta\nu_0 = 4 \times 10^{-3}$. In this case mode 6 dominates the distribution.

Particle diffusion

In studying particle diffusion away from resonances it is found that the tracking code shows no diffusion of particles from the beam-beam interaction over 10^5 rotations. The strong-strong codes are too noisy to study process of diffusion of beam particles due to the beam-beam interaction. With variable charge initialization all particles show diffusive behavior, after 10240 rotations. The diffusion differs substantially from the tracking code. The diffusion coefficient D_x is uniform across the beam radius and is nearly an order of magnitude higher. With uniform charge initialization where the fluctuation noise is lower, only particles with large r/σ, where $r/\sigma = \sqrt{(x/\sigma_x)^2 + (p_x/\sigma_p)^2}$ are diffusive after 10240 rotations. Results from noisy tracking codes modelling the finite particle fluctuation noise indicate that some of the diffusion can be attributed to this noise. This noise can be somewhat offset by using quieter particle initialization schemes such as the uniform charge scheme. However, there are still significant differences from the tracking code. Although the strong-strong code should show differences from the tracking code because of the self-consistent solution of the fields, it is difficult to determine whether the differences observed are due to particle fluctuation noise alone. However, it is apparent that the enhanced diffusion observed in the tails of the distribution for the strong-strong code is due to the self consistent treatment of the beam dynamics.

The δf code which has the lowest fluctuation level shows no particle diffusion up to 10240 rotations agreeing with the tracking code. The noise level of the δf code is less than

the strong-strong code with either the variable or uniform charge distribution. However, particle diffusion is observed after 40960 rotations for particles with large values of $r/\sigma > 2$. It appears that the particles in the tail of the distribution are most sensitive to either noise or collective motion in the beams. Variation of the δf particle number indicates that this diffusion in the tails is not due to particle noise. All particles are diffusive after 10^5 rotations. The magnitude of the diffusion is found to increase exponentially with the action J where $J = (x/\sigma_x)^2 + (p_x/\sigma_p)^2$. This exponential dependence is found to be independent of the number of particles used in the δf simulations. It appears, therefore, that collective beam effects are responsible.

Beam offset effects

In examining the effects of beam offset on diffusion, good agreement is found between analytic theory[34] and the tracking code. This is expected, since the tracking code is based on the "weak-strong" assumption as is the theory. Results from the δf simulations show general agreement with the range of values for the diffusion. The δf code is started with 0 offset and allowed to evolve self-consistently for $M = 10^5$ turns. The values of the diffusion in action are within the range of the analytic prediction. However, the δf results show an exponential dependence on the action J for large values of J whereas the theory shows the diffusion leveling off. The approximate value for the diffusion from the change in luminosity is lower than the diffusion for most of the sample particles in the δf code. Tracking code results with $\langle x \rangle$ input from the δf also do not show the same functional dependence on J as the δf code. The values for the diffusion, however, are within the same range. The leveling-off in the diffusion is observed in the δf simulation when the beam strength $\Delta\nu_0$ is increased. The increase in $\Delta\nu_0$ leads to the increased beam offset $\langle x \rangle$. It appears that when this beam offset is large enough, the resulting diffusion is dominated by beam offset diffusion.[34] This leveling-off in the diffusion is also seen for the strong-strong code. It appears as if the fluctuation

level of the simulation determines whether the diffusion due to the presence of $\langle x \rangle$ offset suggested by Stupakov[34] dominates the process of particle diffusion.

We find (i) that the $D(J)$ is far greater in the δf code than in the tracking code, indicating that conventional tracking code prediction is unrealistically low; (ii) that even the highest value of $D(J)$ from the self-consistent result remains within typical machine design lifetimes of 10^8 turns; and (iii) there appears a strong action, J, dependence.

Future improvements

In this section we discuss possible future improvements which can be made to the codes and future areas of study.

One obvious improvement to the code is extension to x-y and x-y-z dimensions. This extension is straightforward.

Improvements can be made to the simple storage ring model we employed. Some of the effects which can be included in the lattice traversal are[25]:

- betatron damping
- synchrotron motion
- non-zero chromaticity
- longitudinal displacement
- β^* variation along the length of the interaction point
- energy loss and phase change between interaction points
- quantum excitation.

As shown in earlier chapters, the perturbation equation for the δf advance was linear in δf [Eq. (64)]. The term which is neglected is Eq. (65):

$$\delta F(x,s)\,\frac{\partial \delta f}{\partial x'}\ , \tag{144}$$

which was assumed to be small. This term, however, can be incorporated in the δf advance by placing it in the stationary Eq. (56):

$$\frac{\partial f_0}{\partial s} + x'\,\frac{\partial f_0}{\partial x} - (K(s) - F_0(s))x\,\frac{\partial f_0}{\partial x'} = 0 \tag{145}$$

in the following manner:

$$\frac{\partial f_0}{\partial s} + x'\,\frac{\partial f_0}{\partial x} - (K(s) - F_0(s))x\,\frac{\partial f_0}{\partial x'} = \left\langle \delta F(x,s)\,\frac{\partial \delta f}{\partial x'} \right\rangle\ , \tag{146}$$

where $\langle\ \ \rangle$ refers to time average. The incorporation of this term in the stationary Eq. (56) forces the numerical advance now of $f_0(x,x',s)$. However, $f_0(x,x',s)$ is slowly varying as long as it is away from resonances, so that the equation would need to be advanced only every few thousand rotations. The term in Eq. (144) is similar to the quasilinear term used in plasma physics.[12]

Another improvement which can be made includes a higher order method of integration of the particle positions. Higher order integration may be accomplished using the method of symplectic integration algorithms[31] or Lie algrebraic techniques.[11]

Also a possibility exists of applying the technique of differential algebra[2] to the δf algorithm. In this technique the δf method could be treated as a mapping function which could be applied to any points in phase space.

Another approach to the δf method would involve using the Vlasov approach (Eulerian method). The main problem with the Vlasov technique has been that the distribution functions go negative due to truncation errors. However, in the δf technique the main part of the distribution is already determined and the perturbation can go negative without causing problems.

Other areas of investigation would include investigation of betatron resonance, applications to other machines such as HERA or LHC, and the effects of collision angle on beam dynamics.

Acknowledgments

The authors would like to acknowledge constant discussion, stimulation, and collaboration of Dr. A. Chao and his colleagues at SSC Lab. One of the authors (TT) would also like to thank Prof. M. Tigner, who headed the Central Design Group of SSC at Berkeley and encouraged him to look into the beam-beam interaction. He has been on sabbatical at CDG at the invitation of Prof. Tigner and he has also been a consultant to the Director of CDG. Since the site of SSC was chosen, he has been a member of the Accelerator Physics Group of SSCL and a consultant to the management of SSC Lab. TT would also like to thank Prof. R. Schwitters, the former Director of SSCL, for his encouragements. The other author (JKK) has finished his dissertation on this topic at The University of Texas at Austin, and continued on as a SSC Lab Fellow. He too has looked into the accelerator physics issues of SSC in considerable depth.

The work was supported by the U.S. Department of Energy under grants DE-FG05-80ET-53088 and DE-FG05-92ER-40739, and SSC Lab subcontract.

References

[1]Amman, F. and Ritson, D., Intern. Conf. on High Energy Accel., Brookhaven, 471 (1961).

[2]Berz, M., Part. Accel. **24**, 109 (1989).

[3]Birdsall, C.K. and Langdon, A.B. *Plasma Physics via Computer Simulation* (McGraw-Hill, 1985).

[4]Bountis, T., and Tompaidis, S., Institute for Fusion Studies Report #434, 1990.

[5]Chao, A.W., and Ruth, R.D., Particle Accelerators **16**, 201 (1985).

[6]Chao, A.W., SSCL-346, (1991).

[7]Chirikov, B.V., Ford, J., and Vivaldi, F., in *Nonlinear Dynamics and the Beam-Beam Interaction,* A.I.P. Conf. Proc., Vol. 57, Eds. M. Month and J.C. Herrera, p. 323, (A.I.P., New York, 1979).

[8]E.D. Courant and H.S. Synder, Annals of Physics **3**, 1-48 (1958).

[9]Decyk, V.K. and Dawson, J.M., J. Comput. Phys. **30**, 407 (1979).

[10]DiPeso, G., Morse, E.C., and Ziolkowski, R.W., J. Comput. Phys. **96**, 325 (1991).

[11]Dragt, A.J., Neri, F., Rangarajan, G., Douglas, D.R., Healy, L.M., and Ryne, R.D., Ann. Rev. Nucl. Part. Sci. **38**, 455-496 (1988).

[12]W.E. Drummond and D. Pines, Nucl. Fusion Suppl. **3**, 1049 (1962).

[13]Edwards, D.A. and Syphers, M.J., in *Physics of Particle Accelerators* (Fermilab Summer School 1987), Eds. M. Month and M. Dienes, A.I.P. Conference Proceedings 184, (A.I.P., New York, 1989).

[14]Fisher, D., private communication.

[15]Herrera, J.C., Month, M., and Peirels, R.F., in A.I.P. Conference Proceedings 57 *Nonlinear Dynamics and the Beam-Beam interaction*, Eds. M. Month and J.C. Herrera, 1979, NY, p. 203.

[16]Jackson, J.D., *Classical Electrodynamics* (John Wiley and Sons, Inc., 1975).

[17]Jackson, G. and Siemann, R.H., Nucl. Inst. & Methods **286**, 17 (1990).

[18]Kamimura, T., Wagner, T. and Dawson, J.M., Phys. Fluids **21**, 1151 (1978).

[19]Kheifets, S., in *Long-Time Prediction in Dynamics*, Eds. W. Horton, L.E. Reichl, and V.G. Szebehely (John Wiley and Sons, New York, 1983) p. 397.

[20]Klimontovich, Y.L., *The Statistical Theory of Non-Equilibrium Processes in a Plasma* (MIT Press, Cambridge, MA, 1967).

[21]J.K. Koga and T. Tajima, submitted to *J. Comput. Phys.* (1993).

[22]Kotschenreuther, M., Bull. Am. Phys. Soc. **33**, 2109 (1988).

[23]Krishnagopal, S., and Siemann, R., Phys. Rev. Lett. **67**, 2461 (1991).

[24]Kubo, R., J. Phys. Soc. Jpn. **17**, 1100 (1962).

[25]Myers, S., Nucl. Inst. & Methods **211**, 263 (1983).

[26]Neuffer, D., A. Riddiford, and A. Ruggiero, IEEE trans. on Nuclear Sci. **NS-30**, 2430 (1983).

[27]Okuda, H., and Cheng, C.Z., Comp. Phys. Comm. **14**, 169 (1978).

[28]Parzen, E., Technometrics **3**, 167 (1961).

[29]Priestly, M.B., *Spectral Analysis and Time Series*, Vol. 1 (Academic Press, London, 1981).

[30]Richter, B., Proc. Int. Symp. Electron and Positron Storage Rings, Saclay, 1966, p. I-1-1.

[31]Ruth, R., IEEE Trans. Nucl. Sci. **NS-30**, 2669-2671 (1983).

[32]Sands, M., SLAC-121 UC-28 (ACC) (1970).

[33]Siemann, R.H., CESR note **CBN 89-4** (1989).

[34]Stupakov, G., "Luminosity Dilution Due to Random Offset Beam-Beam Interaction," SSCL-560 (1991).

[35]Tajima, T., and Perkins, F.W., Proc. 1983 Sherwood Theory Meeting (University of Maryland, Arlington, VA, 1983) 2P9.

[36]Tajima, T., *Computational Plasma Physics* (Addison-Wesley, Redwood City, 1989).

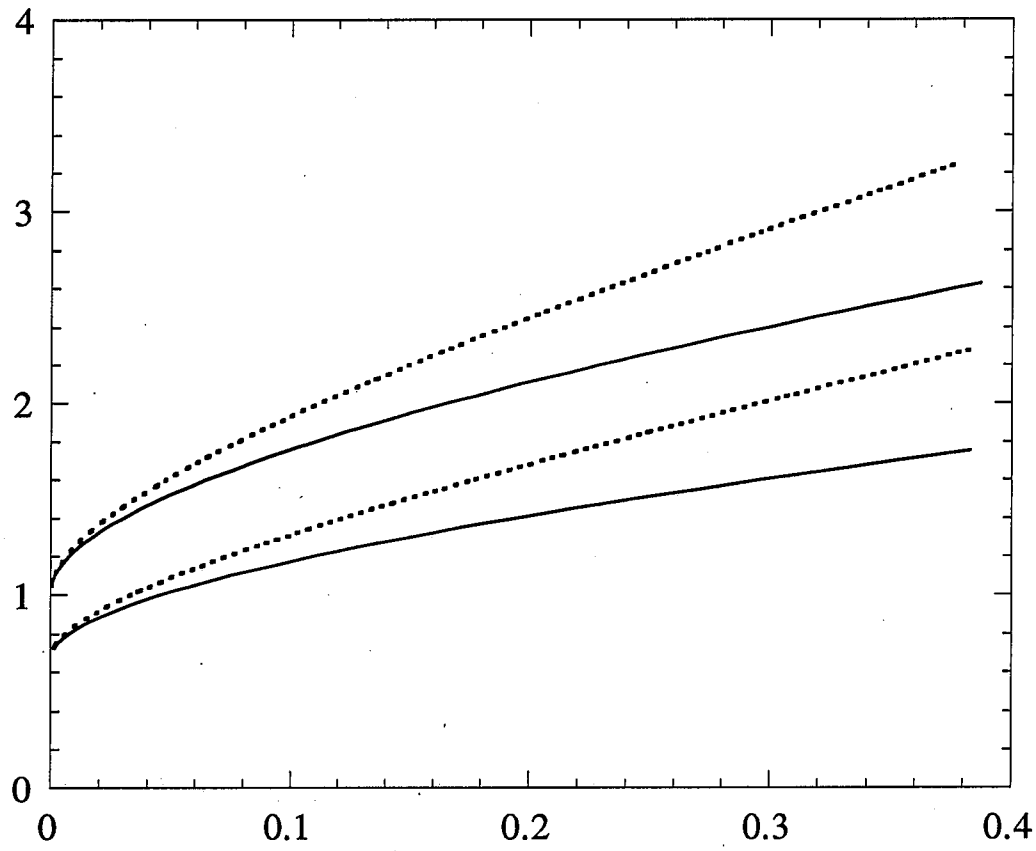
4
3
2
1
0
0
0.1
0.2
0.3
0.4